Excitation of Atoms by Twisted Light

Von der Fakultät für Elektrotechnik, Informationstechnik, Physik
der Technischen Universität Carolo-Wilhelmina zu Braunschweig

zur Erlangung des Grades einer Doktorin
der Naturwissenschaften (Dr. rer. nat.)

genehmigte Dissertation

von
Sabrina Anna-Lena Schulz
aus Tübingen

eingereicht am: 6. Februar 2020

Disputation am: 27. Mai 2020

1. Referent: Prof. Dr. Andrey Surzhykov

2. Referent: Prof. Dr. Peter Lemmens

Druckjahr 2020

To my family

"IN ORDER FOR THE LIGHT TO SHINE SO BRIGHTLY,
THE DARKNESS MUST BE PRESENT. "

– Sir Francis Bacon

Abstract

Twisted light has received a lot of attention in recent years. And there are justified reasons for this. The properties of twisted light are unusual and differ fundamentally from the plane-wave properties. The phase fronts of these light beams have a helical structure, giving them the name *twisted*. This helical phase structure originates from the well-defined orbital angular momentum (OAM) that they carry along their propagation direction and in addition to the spin angular momentum (SAM). Moreover, they have a characteristic intensity profile, which consists of concentric rings with a central minimum, and a phase singularity in the beam center. The latter is why this type of light is sometimes called *vortex light*.

The present thesis is based on two main parts, each dealing with a different aspect of twisted light. These investigations are carried out using Bessel beams, one type of twisted light. Twisted light beams are cylindrically symmetrical. Therefore, they are defined on the basis of circularly polarized light. This fact leads to the first question: Is it possible to generate twisted light in other polarization states? In this work, we derive how this can be achieved by using the superposition principle and how this can be used to construct linearly, radially, or azimuthally polarized Bessel beams, for example.

The focus in the second part of this thesis is on the excitations of atoms by twisted Bessel beams. In particular, we analyze how the use of twisted light can modify individual atomic multipole transitions. The obtained results show that for an efficient modification a precise localization of the target atom is required.

In the last chapter, both aspects are combined. We analyze transitions between magnetic hyperfine states in a single trapped atom (or ion), which is exposed to an additional external magnetic field. The presented calculations for these multipole excitations are based on a formalism that accounts for the alignment of the applied external magnetic field with respect to the propagation direction of the light, and additionally different polarization states of the radiation field are considered. Our results demonstrate that for the excitation a correct alignment of the magnetic field in relation to the propagation direction is essential, but this orientation also strongly depends on the used polarization.

The obtained results indicate that twisted light could be of particular interest for precision experiments. One possible application is the use in single-ion clocks. The work shows that high multipole orders of the vortex beams allow excitations in the intensity minimum in the center of these beams without causing large disturbances, and thus may enable a significant reduction of the light shift in atomic transitions.

Zusammenfassung

Getwisteten Lichtstrahlen wurde in den letzten Jahren viel Aufmerksamkeit gewidmet. Dafür gibt es berechtigte Gründe. Die Eigenschaften von *getwisteten* Lichtstrahlen sind ungewöhnlich und unterscheiden sich grundlegend von den Eigenschaften ebener Wellen: Ihre Phasenfronten weisen eine helikale Struktur auf, woraus der Name *getwisted* hervorgeht. Diese helikale Phasenstruktur resultiert aus dem wohldefinierten Orbitalen-Drehimpuls (OAM), den sie entlang ihrer Ausbreitungsrichtung und zusätzlich zum Spin-Drehimpuls (SAM) haben. Charakterisch ist das ringförmige Intensitätsprofil mit dem zentralen Minimum, ebenso wie die Phasensingularität im Strahlzentrum, weswegen sie auch als *Vortexlicht* bezeichnet werden.

Die vorliegende Arbeit ist im Wesentlichen in zwei Hauptteile gegliedert, die sich jeweils mit einem anderen Aspekt des *getwisteten* Lichts befassen. Diese Untersuchungen werden mit Besselstrahlen, einer Art des *getwisteten* Lichts, durchgeführt. *Getwistete* Lichtstrahlen sind zylindersymmetrisch, aus diesem Grund werden sie in der Basis von zirkular polarisiertem Licht definiert. Diese Tatsache führt zu der ersten hier behandelten Fragestellung: Ist es möglich *getwistetes* Licht in anderen Polarisationszuständen zu generieren? Wir zeigen, wie dies unter Verwendung des Superpositionsprinzip realisiert werden kann und wie damit verschiedene Polarisationszustände von Besselstrahlen, wie zum Beispiel lineare, radiale oder azimuthale Polarisation, konstruiert werden können.

Der Fokus im zweiten Teil dieser Arbeit liegt auf der Anregung von Atomen durch *getwistete* Besselstrahlen. Insbesondere analysieren wir, wie der Einsatz von *getwistetem* Licht einzelne atomare Multipolübergänge modifizieren kann. Die erzielten Ergebnisse zeigen, dass eine genaue Positionierung des anzuregenden Atoms notwendig ist, um eine effiziente Modifikation zu erreichen.

Im letzten Kapitel werden diese beiden Aspekte kombiniert. Dort untersuchen wir Übergänge zwischen magnetischen Hyperfeinstrukturzuständen in einem einzelnen gefangenen Atom (bzw. Ion), das einem zusätzlichen Magnetfeld ausgesetzt ist. Die präsentierten Berechnungen für diese Multipolanregungen beruhen auf einem Formalismus, der die Ausrichtung des angelegten externen Magnetfelds in Bezug auf die Ausbreitungsrichtung des Lichts berücksichtigt und zusätzlich verschiedene Polarisationszustände einschließt. Unsere Ergebnisse zeigen, dass für die Anregung eine korrekte Ausrichtung des Magnetfeldes bezüglich der Ausbreitungsrichtung wichtig ist, die Ausrichtung aber auch von der Polarisation abhängt.

Die erzielten Ergebnisse machen kenntlich, dass *getwistetes* Licht für Präzisionsexperimente von Interesse sein könnte. Eine denkbare Anwendung wäre die Verwendung in Einzelionen-Uhren. Die Arbeit zeigt, dass hohe Multipolordnungen der Vortex-Lichtstrahlen Anregungen im Intensitätsminimum im Zentrum dieser Strahlen ermöglichen, ohne große Störungen zu bewirken und somit eine deutliche Reduktion der Lichtverschiebung in atomaren Übergängen möglich machen.

Contents

List of Figures

List of Symbols

α	fine-structure constant; additional quantum numbers; (dynamic) polarizability
$\boldsymbol{\alpha}$	vector of Dirac matrices
$\boldsymbol{a}_{LM}^{(p)}$	multipole component
$\boldsymbol{\mathcal{A}}$	vector potential
$\boldsymbol{b}$	impact parameter
$\boldsymbol{B}$	magnetic field
D_{LM}^{p}	Wigner-D rotation matrix
d_{LM}^{p}	small Wigner-D rotation matrix
ΔM	$M_f - M_i$
$\Delta\nu_{AC}$	Light shift (quadratic AC-Stark shift)
$\boldsymbol{E}$	electric field
$\boldsymbol{e}_{\boldsymbol{k}}$	polarization vector
F	total angular momentum (quantum number)
ϕ	tilt of the polarization vector (for linearly polarized light) with respect to the x-axis
φ_k	azimuthal angle of the photon momentum $\boldsymbol{k}$
$\widehat{h}$	helicity operator
H_I	interaction operator
I	nuclear spin
$I_\perp$	transverse intensity
J	total electric angular momentum (quantum number)
J_L	spherical Bessel function of the first kind
$\varkappa$	transverse linear momentum
$\boldsymbol{k}$	wave vector; photon momentum
$\boldsymbol{k}_\perp$	transverse linear momentum
$\boldsymbol{k}_z$	longitudinal linear momentum
λ	helicity

L	orbital angular momentum (quantum number)
$[L]$	$2L+1$
M	magnetic quantum number
W_{fi}	matrix element
m_γ	projection of the TAM onto the light propagation direction
m_l	projection of the OAM onto the light propagation direction
p	type of the transition: (p=0) magnetic; (p=1) electric
$\boldsymbol{k}$	wave vector
ω	transition frequency
OAM	orbital angular momentum
$\mathcal{R}$	geometrical factor
$\widetilde{\mathcal{R}}$	averaged geometrical factor
σ	width of the atomic distribution
$\boldsymbol{S}$	Pointing vector; Stokes vector
$S_{0;1;2;3}$	0^{th} to 3^{rd} Stokes parameter
$\widehat{S}$	spin operator; S operator
SAM	spin angular momentum
θ	angle between the applied magnetic field and the direction of light propagation
θ_k	momentum cone opening angle of the twisted photons
$\boldsymbol{T}^M_{L,\Lambda}$	vector spherical harmonics
TAM	total angular momentum
$\widehat{U}$	propagation operator
W_{fi}	transition rate
Y_{LM}	spherical harmonics
z_{atom}	atomic quantization axis and direction of the applied magnetic field
$z(z_{\text{light}})$	propagation direction and quantization axis of the light beam

Chapter 1

Introduction

"This is going to be big [and] it will be easy for the next 10 years but then it will get more technical" [1], said Allen 1992 to his wife after the submission of the paper on what is nowadays known as *orbital angular momentum* (OAM) or *twisted light* [2]. Allen was right with his first statement. This publication can, in some sense, be seen as the "birth of twisted light". Moreover, Allen *et al.* original papers from that time [2, 3] are highly-cited and collect hundreds of new citations each year [4]. His second prediction was wrong – after less than 10 years the topic was already quite technical [1]. However, before moving to a discussion of the theoretical details and experimental applications, we first have to answer the question: "What is twisted light?"

More than a century, in 1909, John H. Poynting proposed that circularly polarized light should have an instinct angular momentum of $\lambda\hbar$ per photon, where $\hbar$ is the Planck constant and $\lambda = \pm 1$ denotes left- or right-handed circular polarization, respectively [5]. Nowadays, this angular momentum is called *spin angular momentum* (SAM), and λ is known as the *helicity* of light – the projection of the spin onto the direction of the momentum. Although Poynting claimed that the effects of λ will be very small, Richard A. Beth was able to observe the physical effects of the SAM by measuring the torque exerted by a circularly polarized beam on a doubly refracting plate [6].

However, the orbital angular momentum (OAM), the other type of angular momentum, is independent of the light polarization. It arises from the spatial profiles of the light intensity and the phase [7]: Allen and co-workers [2] have shown that these *twisted* (or *vortex*) light beams carry a non-zero orbital angular momentum projection of $m\hbar$ onto their propagation direction, which results from the additional phase factor $e^{-im\varphi}$. Consequently, these light beams have properties that differ substantially from those of plane waves: They have a helical phase front and their characteristic intensity profile has an annular pattern with a minimum in the beam center [8]. Unlike the helicity operator, which is (in the Coulomb gauge) restricted to two eigenstates, namely $\lambda = \pm 1$, the values of m are just restricted to integer numbers $m \in \{0, \pm 1, \pm 2, \dots\}$. Thus, the Hilbert space of the orbital angular momentum states is

infinite-dimensional and makes twisted light very attractive for encoding information in quantum communication. m is also known as *topological charge*, and determines the number of intertwined helical phase fronts, while its sign sets the direction of the spiraling. Light beams with a positive topological charge have wavefronts that twist clockwise around the direction of light propagation, and with a negative charge they go anti-clockwise around [7].

Already just after the publication of [2], there was significant interest in laser beams that carry well-defined OAM, both in experiment and theory. In one of the first experimental studies, it was shown that microscopic particles can be held in optical tweezers and that the orbital angular momentum can induce a rotation of these particles. It was possible to distinguish the torque, which is caused by the OAM, from that one which originates from the spin angular momentum. While the SAM induces trapped particles to spin on the beam axis, the OAM let them orbit the vortex in the center [9, 10]. Moreover, it was possible by calibrating the rotations to demonstrate that the OAM per photon is, indeed, $m\hbar$ [11]. Theoretical investigation in these early times [12–14] moved the development further and could already show the complexity of these beams.

Today, the methods to produce twisted light are diverse: spiral phase plates [15, 16], computer generated holograms [8, 17–19], spatial light modulators (SLM), synchrotron radiation in a helical undulator [20], or vortex retarders [21] can be used. Although we have just mentioned some examples, this list is already quite long – but still not complete – we can not discuss all of them in detail. Therefore, we present here the idea of two.

Firstly, we explain the working principle of a spiral phase plate. This method is well established and can nowadays simply be purchased from optics manufacturers. These phase plates are fabricated in such a way that their thickness increases in proportion to the azimuthal angle around the center, see Fig. 1.1. The change in thickness causes an angle-dependent phase-delay to the irradiated plane-wave light beam. Consequently, the plane wave is converted to a twisted light beam. However, the spiral phase plate is a device to create optical vortices only with low topological charges [23].

Beams with high topological charges can be produced with computer generated holograms [18]. Holograms act, like phase plates, on the phase of the incident light. Spatial light modulators (SLM) are nowadays of high precision and are used to display the mask. The computer designed form determines the resulting beams. The holograms that are used to generate OAM beams are fork-like. The resulting topological charge depends on the number of branches. From Fig. 1.2 can be seen, that each extra slit in the upper half of the grating increases the topological charge by one. The advantages of this method with holograms are, on the one hand, that beams with a topological charge of > 100 can easily be produced [18], and, on the other hand, it can also be used for the generation of beams with OAM in a large frequency

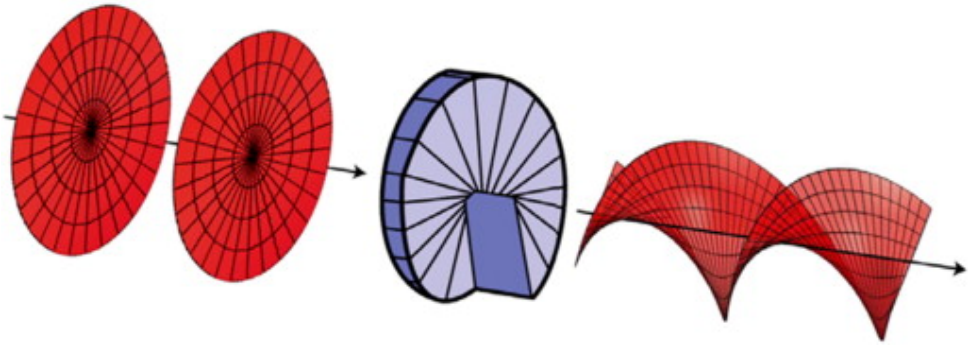

FIGURE 1.1: Principal of a spiral phase plate. The thickness of the spiral phase plate increases to the azimuthal angle. After passing trough the plate, the plane wave-front of the irradiated beam is converted to a OAM beam with a helical phase front due to the azimuthally dependent phase delay. The figure is taken from [22].

range from terahertz to extreme ultraviolet [19].

As mentioned above, twisted light beams have special properties that are very different from those of plane waves. Besides, we have shown that there are numerous possibilities for the creation of beams carrying OAM. The combination of these things make twisted light interesting for various applications, which cover many different research areas, such as quantum information [24], observational astronomy [25], and solid states physics [26]. In recent years, many studies have been made to investigate the interaction with twisted light and matter. For example, the generation of a coherent superposition of vortex states in Bose-Einstein condensates [27], the radiation of twisted photons by ultra-relativistic electrons [28, 29], and intense vortex harmonics in plasma [30]. Furthermore, it was examined that twisted light affects transitions in semiconductors and their nanostructures [31–33], atomic photoionization [34, 35], and Rayleigh, Raman and Compton scattering [36]. The review [37] provides a good overview of recent developments and applications when atoms interact with twisted light.

In this thesis, we will develop a theoretical formalism to analyze the excitations of single atoms (or ions) by using twisted light. We investigate how certain polarization states of the light and the orientation of an applied magnetic field affects the excitation process. Special attention is paid to the analysis of the modification of multipole transitions by twisted light. In order to do so, we need to introduce the underlying theory that is necessary to describe the photoabsorption. This can be divided into three parts: the atomic states, the light (types and properties), and the interaction between both of them.

In Chapter 2, we start with the discussion of the theory of light based on Maxwell's

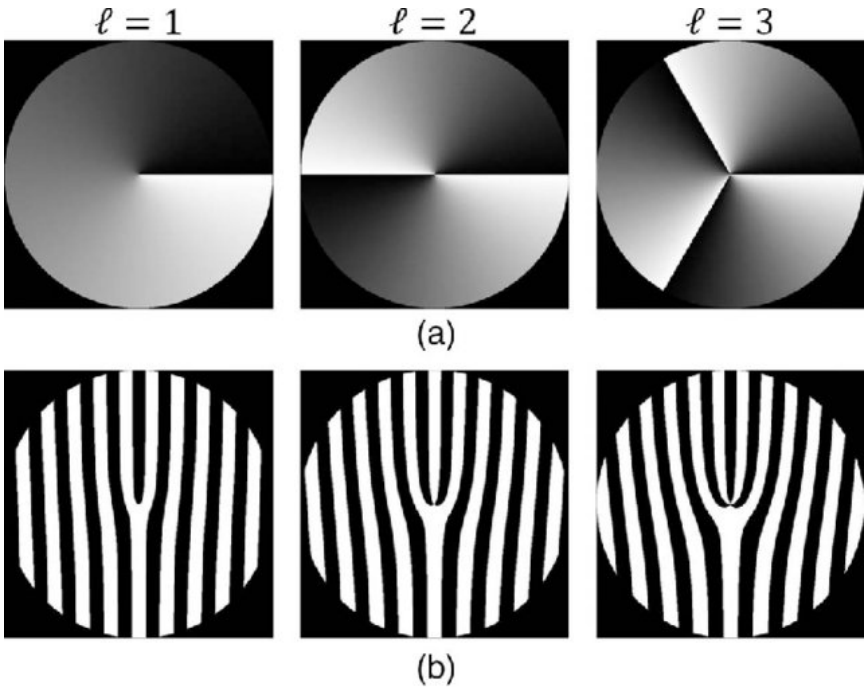

FIGURE 1.2: Principal of a hologram to generate a vortex beam. In the experiment a spatial light modulator (SLM) is used to display the mask. The spiral phases (a) correspond to the OAM beams with topological charges $l = 1, 2, 3$ and are generated with the corresponding fork hologram (b). The figure is taken from [19].

equations. Three different solutions of the wave equation are considered: Plane waves, spherical waves, and twisted Bessel waves. We introduce the vector potentials of all three types of theses waves and discuss their basic properties. Moreover, we introduce the expansion of the optical field in terms of its multipole fields.

Then, in Chapter 3, we focus on the polarization of light. We begin with a short introduction about polarization in general. To characterize the polarization states of the radiation field with observables, we introduce the Stokes parameters. While polarization for plane-wave radiation is homogenous and position independent, it is not for twisted light. Beams with non-zero OAM have complex phase and intensity profiles. We discuss how to construct linearly, radially and azimuthally polarized Bessel beams and show that for these beams also the polarization is non-trivial and spatially inhomogeneous.

In Chapter 4, we study the atom-light interaction. First, we present the basic formulas of the well-established *density matrix formalism*. In order to accord the dynamical behaviour of the atomic quantum states we use the *first-order perturbation theory*. Based on these principles, the transition matrix element for the photoabsorption is derived. Afterwards we study the transition between fine-structure levels in a single atom induced by either plane-wave or twisted Bessel radiation. In each case, explicit expressions are derived for the matrix elements and the transition rates. We

show, in particular, that the excitation of the atom – in the case of twisted light – strongly depends on the atomic position. Therefore, the realistic experimental situation, when the atom is not well-localized is also considered. Afterwards we discuss the selection rules for atomic excitations. We find that the selection rules for interactions with twisted light are modified compared to the well-known plane-waves selection rules.

In Chapter 5, the theoretical formalism is applied to study high order multipole excitations by twisted light. We demonstrate that the relative strength of the multipoles can be strongly modified with respect to the plane-wave case. To quantify this modification by twisted light, we introduce the *geometrical factor*, and to account the delocalization of the atom, the *averaged* geometrical factor. It is found that this factor is sensitive to the atomic positioning. That means for an efficient modification a precise localization of the target atom is required.

Chapter 6 considers the transitions between magnetic hyperfine levels, again induced by twisted Bessel beams. But, in addition to what is analyzed in the previous chapter, here the generalized excitation process is studied when the light propagation direction and the applied magnetic field, which defines the quantization axis of the atom, do not coincide. In particular, we study the electric octupole (E3) hyperfine transition ${}^2S_{1/2}(F=0) \rightarrow {}^2F_{7/2}(F=3)$ in the ${}^{171}\mathrm{Yb}^+$ ion, when the transitions driven by linearly, radially, and azimuthally polarized Bessel beams. This E3 transition, which is commonly used in a single ${}^{171}\mathrm{Yb}^+$ ion clock [38, 39], has an extremely narrow linewidth in the order of 10^{-9} Hz. Therefore, high laser power is needed to drive the transition. We show, that the laser-induced Stark shift can be significantly reduced by using twisted light instead of plane-wave radiation. Finally, in Chapter 7, we summarize the main results and give a outlook.

Hartree atomic units ($\hbar = e = m_e = 4\pi\epsilon_0 = 1,\ c = 1/\alpha$) are used throughout this work, unless stated otherwise explicitly. Here $\hbar$ is the Planck's constant, e is the electron charge, m_e is the electron rest mass, $4\pi\epsilon_0$ is the vacuum permittivity with ϵ_0 being the electric permittivity in vacuum, c is the speed of light in vacuum and $\alpha \approx 1/137$ is the fine-structure constant.

Moreover, vectors are denoted in bold letters, e.g. $\boldsymbol{b}$, and operators are marked with a "hat", for example $\widehat{S}$. An asterisk $*$ denotes the conjugate complex of a quantity.

Chapter 2

Theory of Light

The theory of light has a long history. The earliest studies on the nature of light are dating back to antiquity. At that time the Greeks studied the aspects of vision [40]. It was the Dutch Christiaan Huygens, who proposed the wave theory of light in 1679 [41]. And then in 1865 James Clerk Maxwell completed the classical theory of light by publishing "*A Dynamical Theory of the Electromagnetic Field*" [42]. That is not all about the history of light: Later the quantum nature of light was proposed by Einstein in 1905 [43], but we will not go further in history, for more details see [40, 44].

In this chapter, we first introduce Maxwell's equations. Based on of the electromagnetic wave equation that is derived from Maxwell's equations, we consider three different solutions of the wave equation: We start with the discussion of the familiar plane-wave solutions and continue those for spherical waves. Moreover, we demonstrate the expansion of the radiation field in multipole terms. In the last section of this chapter, we introduce the *twisted Bessel beams*.

2.1 Maxwell's Theory of Light

Maxwell's equations describe all (classical) electromagnetic dynamics. In vacuum they are given by [42, 45]

$$\nabla \cdot \boldsymbol{E}(\boldsymbol{r},t) = 0, \tag{2.1a}$$

$$\nabla \cdot \boldsymbol{B}(\boldsymbol{r},t) = 0, \tag{2.1b}$$

$$\nabla \times \boldsymbol{E}(\boldsymbol{r},t) = -\frac{\partial \boldsymbol{B}}{\partial t}, \tag{2.1c}$$

$$\nabla \times \boldsymbol{B}(\boldsymbol{r},t) = \alpha^2 \frac{\partial \boldsymbol{E}}{\partial t}, \tag{2.1d}$$

where α is the fine-structure constant, $\boldsymbol{E}$ is the electric, and $\boldsymbol{B}$ is the magnetic field. It is convenient to introduce a scalar $\varphi(\boldsymbol{r},t)$ and a vector potential $\boldsymbol{\mathcal{A}}(\boldsymbol{r},t)$. Then, according to the Helmholtz's theorem [46], the electric and magnetic field can be

expressed in terms of these potentials

$$\boldsymbol{E}(\boldsymbol{r},t) = -\nabla\varphi(\boldsymbol{r},t) - \frac{\partial\boldsymbol{\mathcal{A}}(\boldsymbol{r},t)}{\partial t}, \tag{2.2a}$$

$$\boldsymbol{B}(\boldsymbol{r},t) = \nabla\times\boldsymbol{\mathcal{A}}(\boldsymbol{r},t). \tag{2.2b}$$

With (2.2a) and (2.2b) the four equations (2.1a)-(2.1d) reduce to the following two [45]

$$\nabla^2\varphi(\boldsymbol{r},t) + \frac{\partial}{\partial t}(\nabla\cdot\boldsymbol{\mathcal{A}}(\boldsymbol{r},t)) = 0\,, \tag{2.3a}$$

$$\nabla^2\boldsymbol{\mathcal{A}}(\boldsymbol{r},t) - \alpha^2\frac{\partial^2\boldsymbol{\mathcal{A}}(\boldsymbol{r},t)}{\partial t^2} - \nabla\left(\nabla\cdot\boldsymbol{\mathcal{A}}(\boldsymbol{r},t) + \alpha^2\frac{\partial\varphi(\boldsymbol{r},t)}{\partial t}\right) = 0\,. \tag{2.3b}$$

But, as well known, the potentials $\varphi(\boldsymbol{r},t)$ and $\boldsymbol{\mathcal{A}}(\boldsymbol{r},t)$ are not well-defined. Gauge transformations of these potentials leave the electric and magnetic field invariant [45, 47]

$$\boldsymbol{\mathcal{A}}(\boldsymbol{r},t) \to \boldsymbol{\mathcal{A}}'(\boldsymbol{r},t) = \boldsymbol{\mathcal{A}}(\boldsymbol{r},t) + \nabla\chi(\boldsymbol{r},t)\,, \tag{2.4a}$$

$$\varphi(\boldsymbol{r},t) \to \varphi'(\boldsymbol{r},t) = \varphi(\boldsymbol{r},t) - \frac{\partial\chi(\boldsymbol{r},t)}{\partial t}\,, \tag{2.4b}$$

since $\chi(\boldsymbol{r},t)$ is an arbitrary scalar function, which does not change the electric (2.2a) and magnetic fields (2.2b). Within this thesis, we will use the Coulomb gauge, which reads as

$$\nabla\cdot\boldsymbol{\mathcal{A}}(\boldsymbol{r},t) = 0\,, \qquad \varphi(\boldsymbol{r},t) = 0\,. \tag{2.5}$$

$\varphi(\boldsymbol{r},t) = 0$ is a result of our assumption that there is zero source charge density ($\rho = 0$). Then the above equations, (2.3a) and (2.3b), reduce further and we are left with the wave equation, given by

$$\nabla^2\boldsymbol{\mathcal{A}}(\boldsymbol{r},t) - \alpha^2\,\frac{\partial^2\boldsymbol{\mathcal{A}}(\boldsymbol{r},t)}{\partial t^2} = 0\,. \tag{2.6}$$

As seen from this expression, the wave equation is a linear, second-order, partial differential equation and describes the movement of all energy waves (in vacuum) [41]. In this work, we restrict ourselves to monochromatic light with photon energy ω. Thus, we can separate the time dependence from the spatial dependence

$$\boldsymbol{\mathcal{A}}(\boldsymbol{r},t) = \boldsymbol{\mathcal{A}}(\boldsymbol{r})e^{-i\omega t}\,, \tag{2.7}$$

and obtain the Helmholtz equation, the time-independent form of the wave equation, which reads as

$$\nabla^2\boldsymbol{\mathcal{A}}(\boldsymbol{r}) + k^2\boldsymbol{\mathcal{A}}(\boldsymbol{r}) = 0\,, \tag{2.8}$$

where $k = \omega\alpha$ is the wave number. Once the vector potential is known, the electric and magnetic field can be calculated from it (see Eqs. (2.2a) and (2.2b)). Therefore, when no sources are present, $\varphi(\boldsymbol{r}, t) = 0$, we get for the electric and magnetic field the following expressions

$$\boldsymbol{E}(\boldsymbol{r}, t) = -\frac{\partial \boldsymbol{\mathcal{A}}(\boldsymbol{r}, t)}{\partial t}, \tag{2.9a}$$

$$\boldsymbol{B}(\boldsymbol{r}, t) = \nabla \times \boldsymbol{\mathcal{A}}(\boldsymbol{r}, t). \tag{2.9b}$$

2.2 Plane Waves

In the previous section, we derived the wave equation (2.8), which describes the propagation of electromagnetic waves in vacuum. The simplest solutions to this equation are plane waves. The vector potential of a circularly polarized plane wave vector potential reads as

$$\boldsymbol{\mathcal{A}}^{(\mathrm{pl})}_{\boldsymbol{k}\lambda}(\boldsymbol{r}) = \boldsymbol{e}_{\boldsymbol{k}\lambda}\, \mathrm{e}^{i\boldsymbol{k}\cdot\boldsymbol{r}}, \tag{2.10}$$

where $\boldsymbol{k}$ and $\boldsymbol{e}_{\boldsymbol{k}\lambda}$ denote the wave and the polarization vectors, and $\lambda = \pm 1$ is the helicity of light. In this work, we write the polarization vector as

$$\boldsymbol{e}_{\boldsymbol{k}\lambda} = \frac{1}{\sqrt{2}} \begin{pmatrix} 1 \\ i\lambda \\ 0 \end{pmatrix}, \tag{2.11}$$

following the convention of Rose [48]. Then, the vector potential (2.10) describes a plane wave with right circular polarization, if $\lambda = 1$, and for $\lambda = -1$ it is left circularly polarized.

Next, we will discuss some basis characteristics of plane-waves. We assume a harmonic time dependence, so that $\boldsymbol{\mathcal{A}}^{(\mathrm{pl})}_{\boldsymbol{k}\lambda}(\boldsymbol{r}, t) = \boldsymbol{\mathcal{A}}^{(\mathrm{pl})}_{\boldsymbol{k}\lambda}(\boldsymbol{r}) e^{-i\omega t}$. Therefore, by making use of Eq. (2.9a) as well as the Maxwell equation (2.1c), we obtain the expressions for the electric and magnetic field

$$\boldsymbol{E}^{(\mathrm{pl})}_{\boldsymbol{k}\lambda}(\boldsymbol{r}, t) = i\omega \boldsymbol{\mathcal{A}}^{(\mathrm{pl})}_{\boldsymbol{k}\lambda}(\boldsymbol{r}, t), \tag{2.12a}$$

$$\boldsymbol{B}^{(\mathrm{pl})}_{\boldsymbol{k}\lambda}(\boldsymbol{r}, t) = \frac{1}{\omega}\left(\boldsymbol{k} \times \boldsymbol{E}^{(\mathrm{pl})}_{\boldsymbol{k}\lambda}(\boldsymbol{r}, t)\right). \tag{2.12b}$$

From these two equations, together with Eq. (2.1a), follows directly that $\boldsymbol{E}$, $\boldsymbol{B}$, and $\boldsymbol{k}$ are orthogonal to each other

With these expressions, Eqs. (2.12a) and (2.12b), we are able to calculate the Poynting vector $\boldsymbol{S}$, which is defined as the cross-product of the electric and magnetic field [45]. However, since the instantaneous values of the fields are not measurable,

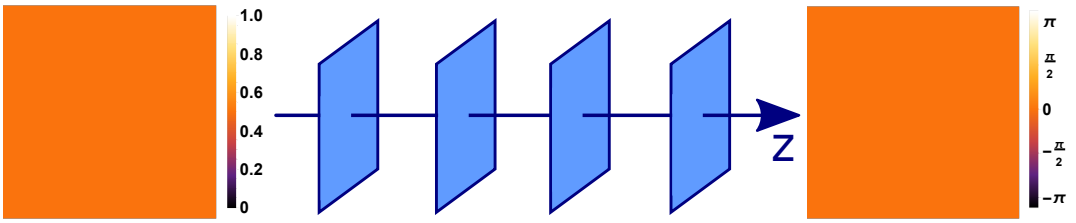

FIGURE 2.1: The basic characteristics of plane waves. Plane waves exhibit a homogeneous intensity profile transverse to their propagation direction (left panel). Their wavefronts are planes, orthogonal to the beam axis (middle panel). The phase profile of a plane wave is smooth (right panel).

we are interested in the time-averaged Poynting vector. This vector represents the energy flux density and the intensity profile of an electromagnetic wave [41, 45], and, in vacuum, it is given as [49]

$$\boldsymbol{S}(\boldsymbol{r}) = \frac{1}{4\pi\,\alpha}\,\mathrm{Re}\Big(\boldsymbol{E}(\boldsymbol{r}) \times \boldsymbol{B}^{*}(\boldsymbol{r})\Big)\,. \tag{2.13}$$

The transverse intensity of the light beam is proportional to the absolute value of its z-component

$$I_{\perp}(\boldsymbol{r}) \propto |S_z(\boldsymbol{r})|. \tag{2.14}$$

In the case of plane waves, as follows from Eq. (2.12b), the Poynting vector points in the propagation direction, i.e. $\boldsymbol{S} \parallel \boldsymbol{k}$, and is constant for all positions in space. Therefore, their transverse intensity profile is homogenous, as seen from the left picture in Fig. 2.1.

Plane waves carry a well-defined linear momentum $\boldsymbol{k}$, i.e. their vector potential $\boldsymbol{\mathcal{A}}^{(\mathrm{pl})}_{\boldsymbol{k}\lambda}$ is an eigenfunction of each component of the linear momentum operator $\widehat{p}_j = -i\frac{\partial}{\partial x_j}$ (where $j = 1, 2, 3$) to $\boldsymbol{\mathcal{A}}^{(\mathrm{pl})}_{\boldsymbol{k}\lambda}$. Thus, we get the following eigenequations

$$\widehat{p}_j \boldsymbol{\mathcal{A}}^{(\mathrm{pl})}_{\boldsymbol{k}\lambda} = k_j \boldsymbol{\mathcal{A}}^{(\mathrm{pl})}_{\boldsymbol{k}\lambda} \qquad j = 1, 2, 3\,. \tag{2.15}$$

The linear momentum of plane waves is parallel to the propagation direction. This can also be obtained from Eq. (2.12b). Next, we want to analyze how the wavefronts of these waves look like. In order to do so, we need to set the phase $\boldsymbol{k}\cdot\boldsymbol{r} - \omega t$ to constant. For the wave propagating along $\boldsymbol{r}$ follows, $\boldsymbol{k}\cdot\boldsymbol{r} = \text{const}$: The wavefronts of plane waves are planes with constant phase perpendicular to the propagation direction, see Fig. 2.1 (middle panel).

Apart from the linear momentum, light can also carry angular momentum (AM). There are two types of angular momentum: the spin angular momentum (SAM) and the orbital angular momentum (OAM). The latter, the OAM, we will discuss in Sec. 2.4 because the OAM is related to a spatially variant phase and since the phase is

constant for plane waves, c.f. Fig 2.1 (right panel), the OAM is zero for plane waves. It is well-known that the SAM is associated with the circular polarization of light [50]. The projection of the SAM onto the propagation direction is called *helicity* λ. The spin angular momentum operator is a vector operator $\widehat{\boldsymbol{S}}$. If we assume that the light propagates along the z-direction, we only need its z-component, which reads as [48]

$$\widehat{S}_z = \begin{pmatrix} 0 & -i & 0 \\ i & 0 & 0 \\ 0 & 0 & 0 \end{pmatrix}. \tag{2.16}$$

Hence, with this restriction on $\boldsymbol{\mathcal{A}}^{(\mathrm{pl})}_{\boldsymbol{k}\lambda}(z,t) = \boldsymbol{e}_{\boldsymbol{k}\lambda} e^{ik_z z}$, one can easily prove, that $\boldsymbol{\mathcal{A}}^{(\mathrm{pl})}_{\boldsymbol{k}\lambda}(z,t)$ is an eigenfunction of $\widehat{S}_z$

$$\widehat{S}_z \boldsymbol{\mathcal{A}}^{(\mathrm{pl})}_{\boldsymbol{k}\lambda} = \lambda \boldsymbol{\mathcal{A}}^{(\mathrm{pl})}_{\boldsymbol{k}\lambda}, \tag{2.17}$$

where the eigenstate $\lambda = \pm 1$ is the helicity of the photon, associated with left and light circular polarization, respectively. In general, if the light propagates not along the z-direction, all three components of $\widehat{\boldsymbol{S}}$ have to be taken into account. The x- and y-component can also be found in [48] and are given by

$$\widehat{S}_x = \begin{pmatrix} 0 & 0 & 0 \\ 0 & 0 & -i \\ 0 & i & 0 \end{pmatrix}, \qquad \widehat{S}_y = \begin{pmatrix} 0 & 0 & i \\ 0 & 0 & 0 \\ -i & 0 & 0 \end{pmatrix}. \tag{2.18}$$

As mentioned above, helicity is the projection of SAM onto the propagation direction. Therefore, for the general case (when the propagation is not along the z-axis), we have to introduce the helicity operator, which is defined as [51]

$$\widehat{h} = \widehat{\boldsymbol{S}} \cdot \widehat{\boldsymbol{p}}, \tag{2.19}$$

where $\widehat{\boldsymbol{p}} = \frac{\boldsymbol{p}}{p}$.

Since the fundamental equations are based on circularly polarized light, it is reasonable to use cylindrical coordinates $(r_\perp, \varphi_r, z)$. Then, the momentum $\boldsymbol{k}$ for a plane wave propagating in (θ_k, φ_k) direction reads as [34]

$$\boldsymbol{k} = \begin{pmatrix} k_\perp \cos\varphi_k \\ k_\perp \sin\varphi_k \\ k_z \end{pmatrix}, \tag{2.20}$$

where $k_\perp$ and k_z are the transversal and longitudinal momentum, respectively, and the absolute photon momentum of $\boldsymbol{k}$ is $k = \sqrt{k_\perp^2 + k_z^2}$. $\theta_k = \arctan(k_\perp / k_z)$ and φ_k denote the polar and azimuthal angle of $\boldsymbol{k}$. For the plane wave, we need also to

rewrite the polarization vector

$$\boldsymbol{e}_{\boldsymbol{k}\lambda} = \frac{1}{\sqrt{2}} \begin{pmatrix} \cos\theta_k \cos\varphi_k - i\lambda \sin\varphi_k \\ \cos\theta_k \sin\varphi_k + i\lambda \cos\varphi_k \\ -\sin\theta_k \end{pmatrix} . \tag{2.21}$$

The vectors $\boldsymbol{e}_{\boldsymbol{k}\lambda}$ are solutions of the corresponding eigenvalue problem for the helicity operator [34]. Consequently, $\boldsymbol{e}_{\boldsymbol{k}\lambda} e^{i\boldsymbol{k}\cdot\boldsymbol{r}}$ describes a circularly polarized plane wave with well-defined helicilty λ along the direction of propagation. Moreover, from the Coulomb gauge condition (2.5) follows $\boldsymbol{e}_{\boldsymbol{k}\lambda} \cdot \boldsymbol{k} = 0$, i.e. the polarization vector is orthogonal to the momentum $\boldsymbol{k}$.

These plane waves can be used to construct a twisted Bessel light beam, but before we do this, we will introduce the spherical waves and expand the plane waves into multipoles in the next section.

2.3 Multipole Expansion and Spherical Waves

Since electromagnetic radiation fields are produced by oscillating electric charges and oscillating currents or magnetic moments for electric or magnetic radiation, respectively [52], it is natural to express these *multipole fields* with spherical waves [41, 45, 53]. To solve this problem, we need to find solutions to the Helmholtz equation (2.8) in spherical coordinates. As a starting point we consider the scalar Helmholtz equation $\nabla^2\psi = -k^2\psi$ and use the *separation of variables* method to solve this differential equation. That means, we consider solutions of the form

$$\psi(\boldsymbol{r}) = R(r)\Theta(\theta)\Phi(\phi)\,, \tag{2.22}$$

and the Helmholtz equation separates in the following three ordinary differential equations [54]

$$\frac{d^2\Phi(\phi)}{d\phi^2} + M^2\Phi(\phi) = 0\,, \tag{2.23a}$$

$$\frac{1}{\sin\theta}\frac{d^2}{d\theta^2}\left(\sin\theta\frac{d^2\Theta(\theta)}{d\theta^2}\right) + \left(L^2 - \frac{M^2}{\sin^2\theta}\right)\Theta(\theta) = 0\,, \tag{2.23b}$$

$$r^2\frac{d^2R(r)}{dr^2} + 2r\frac{dR(r)}{dr} + \left(k^2r^2 - L^2\right)R(r) = 0\,. \tag{2.23c}$$

The *spherical harmonics* $Y_{LM}(\theta,\phi) = \Theta(\theta)\Phi(\phi)$ are solutions for the angular variables, and the *spherical Bessel functions* $J_L(kr)$ for the radial coordinate [54]. Therefore, the solutions for this problem in spherical coordinates is given by solutions of the form

$$\psi_{LM}(\boldsymbol{r}) = J_L(kr)\,Y_{LM}(\theta,\phi)\,. \tag{2.24}$$

They fulfill the angular momentum and parity properties that are required in order to get physically solutions [48, 55]: Since the parity operation, i.e. the replacing $\theta \to \pi - \theta$ and $\phi \to \pi + \phi$, affects only the angular part, we have [48]

$$Y_{LM}(\pi - \theta, \pi + \phi) = (-1)^L \, Y_{LM}(\theta, \phi) \, . \tag{2.25}$$

And, moreover, the spherical harmonics $Y_{LM}(\theta, \phi)$ are simultaneous eigenfunctions of the *orbital angular momentum operator* $\widehat{\boldsymbol{L}}^2$ and its z-component $\widehat{L}_z$

$$\widehat{\boldsymbol{L}}^2 Y_{LM}(\theta, \phi) = L(L+1) \, Y_{LM}(\theta, \phi) \, , \tag{2.26a}$$

$$\widehat{L}_z Y_{LM}(\theta, \phi) = M \, Y_{LM}(\theta, \phi) \, , \tag{2.26b}$$

where L is the *orbital angular momentum quantum number* with $L = 0, 1, 2, \ldots$ and M the *magnetic quantum number* with $M = -L, \ldots, +L$. It can be shown that the solutions (2.22) form a complete set. Therefore, we can use them to express the plane wave solutions (2.10) in terms of them.

In this work, we are especially interested in the contributions from different multipole channels to atomic excitations. Therefore, we expand the vector potential $\boldsymbol{\mathcal{A}}^{(\mathrm{pl})}_{\boldsymbol{k}\lambda}$ (2.10) in terms of its multipole components. In the first part of this section, we derived solutions (2.24) for the scalar Helmholtz equation. Since the electric and magnetic field are vector fields, we need vectorial solutions. The scalar functions (2.24) can be transformed into vector fields [54], which solve the vector Helmholtz equation (2.8). However, we will not derive these formulas here, but simply use the solutions below, for details we refer to [48].

The explicit form of the expansion depends on the choice of the quantization axis of light, z_{light} (or z). If the light propagation direction $\hat{\boldsymbol{k}} = \boldsymbol{k}/k = (\theta_k, \varphi_k)$ does not coincide with the quantization (z) axis, the multipole expansion has the following form [48, 56]

$$\boldsymbol{\mathcal{A}}^{(\mathrm{pl})}_{\boldsymbol{k}\lambda}(\boldsymbol{r}) = \sqrt{2\pi} \sum_{LM} \sum_{p=0,1} i^L [L]^{\frac{1}{2}} \, (i\lambda)^p \, D^p_{LM}(\varphi_k, \theta_k, 0) \, \boldsymbol{a}^{(p)}_{LM} \, , \tag{2.27}$$

where $[L] = 2L + 1$ and $D^p_{LM}(\varphi_k, \theta_k, 0) = e^{-iM\varphi_k} \, d^p_{LM}(\theta_k)$ is the Wigner-D rotation matrix. Here $\boldsymbol{a}^{(p)}_{LM}$ refers to magnetic ($p = 0$) and electric ($p = 1$) multipole components, that are constructed as irreducible tensors of rank L and each of them is given by [48, 56]

$$\boldsymbol{a}^{(0)}_{LM}(\boldsymbol{r}) = j_L(kr) \boldsymbol{T}^M_{L,L}, \tag{2.28a}$$

$$\boldsymbol{a}^{(1)}_{LM}(\boldsymbol{r}) = j_{L-1}(kr) \sqrt{\frac{L+1}{2L+1}} \boldsymbol{T}^M_{L,L-1} - j_{L+1}(kr) \sqrt{\frac{L}{2L+1}} \boldsymbol{T}^M_{L,L+1}, \tag{2.28b}$$

where $\boldsymbol{T}^M_{L,\Lambda}$ are the vector spherical harmonics of rank L. They represent an extension of the scalar spherical harmonics Y_{LM} to the vectorial case that results form coupling

Y_{LM} to the spherical unit vectors $\boldsymbol{\xi}_\pm = \frac{\mp 1}{\sqrt{2}}(1, \pm i, 0)$ and $\boldsymbol{\xi}_0 = (0, 0, 1)$ [56]

$$\boldsymbol{T}^M_{L,\Lambda} = \sum_m \langle \Lambda M{-}m \;\; 1m \mid LM \rangle \, Y_{\Lambda,M-m} \, \boldsymbol{\xi}_m, \tag{2.29}$$

where $\langle \ldots \ldots \mid \ldots \rangle$ is a Clebsch-Gordan coefficient. It is worth to mention here, that the multipole potentials $\boldsymbol{a}^{(p)}_{LM}(\boldsymbol{r})$ are constructed in such a way, that they are eigenfunctions of $\hat{\boldsymbol{J}}^2$, J_z and the parity operator. Moreover, since they are constructed as linear combinations of the vector spherical harmonics, they satisfy the Helmholtz equation [48].

Now, that we have discussed the plane and spherical waves, we can proceed to construct twisted light, which can in some sense be understood as solutions of the wave equation between plane waves and spherical waves.

2.4 Twisted Light

So far, we have discussed circularity polarized plane waves. In Sec. 2.2, we have shown that they carry a well-defined spin angular momentum along their propagation direction. In this section, we will introduce so-called twisted (or vortex) light beams. These beams have an orbital angular momentum (OAM) in addition to the spin angular momentum. In this study, we consider one of the most common types of twisted light beams, known as Bessel beams, whose vector potential $\boldsymbol{\mathcal{A}}^{(\mathrm{tw})}_{m_\gamma \lambda}$ is a solution of the Helmholtz equation (2.8) in Coulomb gauge (2.5) and reads as [34, 57]

$$\boldsymbol{\mathcal{A}}^{(\mathrm{tw})}_{m_\gamma \lambda}(\boldsymbol{r}) = \int \frac{d^2\boldsymbol{k}_\perp}{(2\pi)^2} \boldsymbol{e}_{\boldsymbol{k}\lambda} e^{i\boldsymbol{k}\cdot\boldsymbol{r}} a_{\varkappa m_\gamma}(\boldsymbol{k}_\perp) \tag{2.30}$$

with the amplitude

$$a_{\varkappa m_\gamma}(\boldsymbol{k}_\perp) = \frac{2\pi}{\varkappa}(-i)^{m_\gamma} e^{i m_\gamma \varphi_k} \delta(k_\perp - \varkappa). \tag{2.31}$$

We have chosen the normalization factor in such a way that the normalization condition for plane waves $\int d^3\boldsymbol{r} \boldsymbol{\mathcal{A}}^{(\mathrm{pl})}_{\boldsymbol{k}\lambda} \boldsymbol{\mathcal{A}}^{*(\mathrm{pl})}_{\boldsymbol{k'}\lambda'} = \delta^{(3)}(\boldsymbol{k} - \boldsymbol{k'})\delta_{\lambda,\lambda'}$ is also satisfied for twisted light. The vector potential (2.30) describes a photon beam with energy ω, that carries the projection m_γ of total angular momentum (TAM) on the propagation axis. Again, this axis is taken along the quantization axis z_{light}. Moreover, as follows from Eqs. (2.30) and (2.31) the Bessel beam can be seen as a superposition of plane waves whose wave vectors form a cone with height k_z and radius $|\boldsymbol{k}_\perp| = \varkappa$. $\theta_k = \arctan(\varkappa/k_z)$ is the opening angle of this momentum cone, see Fig. 2.2.

In Eq. (2.30) the vector potential $\boldsymbol{\mathcal{A}}^{(\mathrm{tw})}_{m_\gamma \lambda}$ is written in the integral representation, but for further calculations it is convenient to perform the integrations: The differential in cylindrical coordinates is $d^2\boldsymbol{k}_\perp = k_\perp dk_\perp d\varphi_k$. First, we integrate over the transverse momentum $k_\perp$. And to continue with the integration over φ_r, we expand

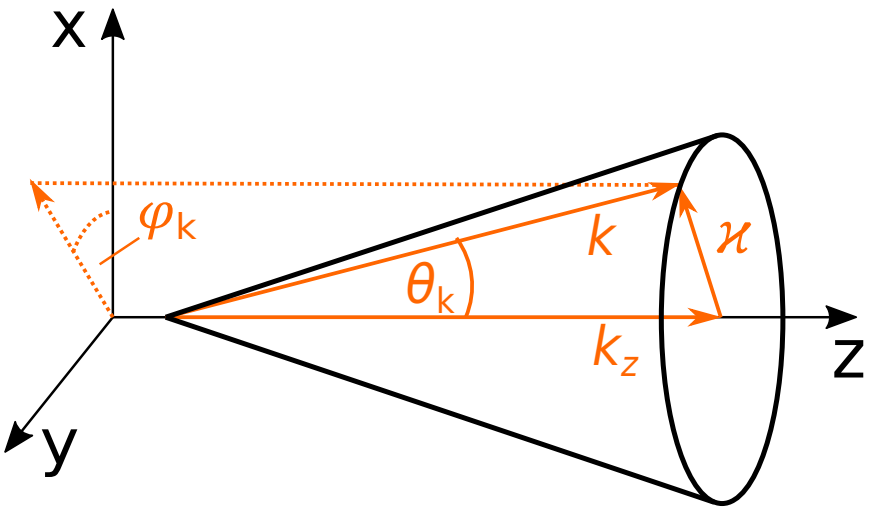

FIGURE 2.2: Momentum cone for a twisted Bessel light beam. A Bessel beam can be seen as a superposition of circularly polarized plane waves. All states that contribute to the vector potential $\boldsymbol{\mathcal{A}}^{(\mathrm{tw})}_{m_\gamma \lambda}$ lie on a momentum cone with an opening angle of $\theta_k = \arctan(\varkappa/k_z)$, radius $\varkappa$ and height k_z. $k_\perp$ and k_z are the transversal and longitudinal momentum, respectively. The opening angle θ_k is the polar and φ_k is the azimuthal angle of the momentum $\boldsymbol{k}$.

the polarization vector $\boldsymbol{e}_{\boldsymbol{k}\lambda}$ in terms of $\boldsymbol{e}_{\pm 1} = \frac{1}{\sqrt{2}}(1, \pm i, 0)$ and $\boldsymbol{e}_0 = (0, 0, 1)$, and the coefficients $c_{m_s=\pm 1} = \frac{\pm\lambda}{2}(1 \pm \lambda \cos\theta_k)$ and $c_{m_s=0} = \frac{-1}{\sqrt{2}} \sin\theta_k$. This expansion is given by

$$\boldsymbol{e}_{\boldsymbol{k}\lambda} = \sum_{m_s=0,\pm 1} c_{m_s}\, e^{-i m_s \varphi_k} \boldsymbol{e}_{m_s}. \tag{2.32}$$

Then, to perform the integration over φ_k, we make use of this expansion (2.32) and the relation $\boldsymbol{k}_\perp \cdot \boldsymbol{r}_\perp = k_\perp r_\perp \cos(\varphi_k - \varphi_r)$. After the integrations we get the vector potential $\boldsymbol{\mathcal{A}}^{(\mathrm{tw})}_{m_\gamma \lambda}(\boldsymbol{r})$ in cylindrical coordinates $(r_\perp, \varphi_r, z)$ [34], which reads as

$$\boldsymbol{\mathcal{A}}^{(\mathrm{tw})}_{m_\gamma \lambda}(\boldsymbol{r}) = \sum_{m_s=0,\pm 1} (-i)^{m_s}\, c_{m_s}\, J_{m_\gamma - m_s}(\varkappa r_\perp)\, e^{i(m_\gamma - m_s)\varphi_r} e^{i k_z z} \boldsymbol{e}_{m_s}\,, \tag{2.33}$$

where we used the integral representation for the Bessel function of the first kind [58, 59]

$$\int_0^{2\pi} e^{il\alpha}\, e^{ix\cos(\beta-\alpha)}\, d\alpha = 2\pi\, i^l\, e^{il\beta}\, J_l(x)\,. \tag{2.34}$$

For further calculations, it is more convenient to express $\boldsymbol{\mathcal{A}}^{(\mathrm{tw})}_{m_\gamma \lambda}(\boldsymbol{r})$ in terms of the scalar functions of the vector potential

$$\mathcal{A}^{(\mathrm{tw})}_{m_\gamma m_s}(\boldsymbol{r}) = (-i)^{m_s}\, c_{m_s}\, J_{m_\gamma - m_s}(\varkappa r_\perp)\, e^{i(m_\gamma - m_s)\varphi_r} e^{ik_z z}\,. \tag{2.35}$$

Then, Eq. (2.33) is given as a sum of them

$$\boldsymbol{\mathcal{A}}^{(\mathrm{tw})}_{m_\gamma \lambda}(\boldsymbol{r}) = \sum_{m_s = 0, \pm 1} \mathcal{A}^{(\mathrm{tw})}_{m_\gamma m_s}(\boldsymbol{r})\, \boldsymbol{e}_{m_s}\,. \tag{2.36}$$

2.4.1 Bessel Beams in the Paraxial Regime

For small opening angles $\theta_k \ll 1$, i.e. when the transverse momentum $\varkappa$ of the Bessel beam is much smaller than the longitudinal one k_z, the vector potential $\boldsymbol{\mathcal{A}}^{(\mathrm{tw})}_{m_\gamma \lambda}$ (2.33) can be simplified. This is called *paraxial regime*. In this regime, the opening angle is very small, so that the momentum vectors are almost parallel to the propagation axis and the beam behaves nearly like a plane wave. Then, the sum in (2.36) is limited to a single term $m_s = \lambda$ and the coefficients $c_{m_s = \lambda}$ reduce to

$$c_{\pm 1} \approx \frac{1}{2}(1 \pm \lambda)\,; \quad c_0 \approx 0\,, \tag{2.37}$$

where $\cos\theta_k \approx 1$ is a good approximation in this paraxial regime. Thus, for this case, the vector potential is given by

$$\boldsymbol{\mathcal{A}}^{(\mathrm{tw})}_{m_l \lambda}(\boldsymbol{r}) = (-i)^{\lambda}\, \boldsymbol{e}_{\boldsymbol{k}\lambda}\, J_{m_l}(\varkappa r_\perp)\, e^{i m_l \varphi_r} e^{ik_z z}\,. \tag{2.38}$$

Next, we analyze the angular momentum properties of the twisted Bessel beams in the paraxial regime. In Sec. 2.2 we introduced the SAM operator (2.16) and (2.18). Twisted light beams, however, carry not only a spin angular momentum but also an orbital angular momentum (OAM). The z-component of the OAM operator is defined as

$$\widehat{L}_z = -i\frac{\partial}{\partial \varphi_r}\,. \tag{2.39}$$

And the sum of both, the spin and the orbital angular momentum, is given by the total angular momentum (TAM) operator, which reads as

$$\widehat{J}_z = \widehat{S}_z + \widehat{L}_z\,. \tag{2.40}$$

Only in the paraxial approximation SAM and OAM are decoupled. This can be observed with Eq. (2.38) by applying the SAM, OAM operator, and the TAM operator.

Then, the vector potential $\boldsymbol{\mathcal{A}}^{(\mathrm{tw})}_{m_l\lambda}$ is a simultaneous eigenfunction of $\widehat{S}_z$, $\widehat{L}_z$, and $\widehat{J}_z$

$$\widehat{S}_z\, \boldsymbol{\mathcal{A}}^{(\mathrm{tw})}_{m_l\lambda} = \lambda\, \boldsymbol{\mathcal{A}}^{(\mathrm{tw})}_{m_l\lambda}\,, \tag{2.41a}$$

$$\widehat{L}_z\, \boldsymbol{\mathcal{A}}^{(\mathrm{tw})}_{m_l\lambda} = m_l\, \boldsymbol{\mathcal{A}}^{(\mathrm{tw})}_{m_l\lambda}\,, \tag{2.41b}$$

$$\widehat{J}_z\, \boldsymbol{\mathcal{A}}^{(\mathrm{tw})}_{m_l\lambda} = (\lambda + m_l)\, \boldsymbol{\mathcal{A}}^{(\mathrm{tw})}_{m_l\lambda}\,. \tag{2.41c}$$

Therefore, in the paraxial regime, a twisted Bessel photon carries the OAM projection m_l along the z-axis, the helicity λ, and the TAM projection $\lambda + m_l$. Otherwise, in the non-paraxial regime, just their sum, the total angular momentum, is well-defined, and we obtain

$$\widehat{J}_z\, \boldsymbol{\mathcal{A}}^{(\mathrm{tw})}_{m_\gamma\lambda} = m_\gamma\, \boldsymbol{\mathcal{A}}^{(\mathrm{tw})}_{m_\gamma\lambda}\,. \tag{2.42}$$

Next, we are going to analyze the wavefronts of a twisted Bessel beam in the paraxial approximation. These surfaces of constant phase are determined by the relation

$$m_l\varphi_r + k_z z - \omega t = \mathrm{const}\,, \tag{2.43}$$

and have a helical structure. This structure is caused by the phase factor of $m_l\varphi_r$, which they have in addition compared to the plane waves. The projection of the OAM m_l in Eq. (2.43), which is also known as *topological charge*, determines the number of intertwined helices. The sign of the topological charge indicates, whether the wavefronts twist clockwise for positive m_l, or anti-clockwise, if m_l is negative [7]. This phase property gives twisted light its name: The wavefronts "twist" around the light propagation axis. The helical wavefront for a Bessel beam with an OAM of $m_l = 1$ is depicted in the middle picture of Fig. 2.3. And the right panel shows the transverse phase profile this beam. Due to the helical phase variation along their propagation direction, these beams have an undefined phase in the beam center resulting in a phase singularity.

2.4.2 The Electric and Magnetic Field of Bessel Beams

Twisted light beams are cylindrical symmetric. Therefore, for the further analysis, it is convenient to rewrite the vector potential $\boldsymbol{\mathcal{A}}^{(\mathrm{tw})}_{m_\gamma\lambda}(\boldsymbol{r})$ (2.33) in cylindrical coordinates ($r_\perp$, φ_r, z). The cylindrical unit vectors are related to the Cartesian unit vectors as follows

$$\begin{pmatrix} \boldsymbol{e}_x \\ \boldsymbol{e}_y \\ \boldsymbol{e}_z \end{pmatrix} = \begin{pmatrix} \cos\varphi_r & -\sin\varphi_r & 0 \\ \sin\varphi_r & \cos\varphi_r & 0 \\ 0 & 0 & 1 \end{pmatrix} \begin{pmatrix} \boldsymbol{e}_{r_\perp} \\ \boldsymbol{e}_{\varphi_r} \\ \boldsymbol{e}_z \end{pmatrix}\,. \tag{2.44}$$

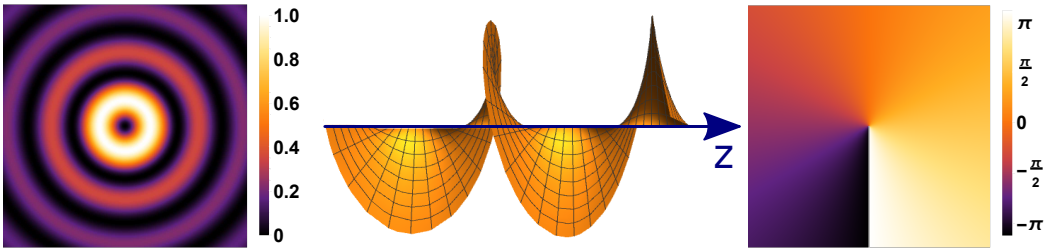

FIGURE 2.3: The basic properties for a twisted Bessel beam. The results show the transverse intensity profile of a twisted Bessel beam (left panel), which has an annular character with an intensity minimum in the beam center, the helical wavefronts (middle panel) that depend on the orbital angular momentum, and the phase profile (right panel), which variates with the azimuthal angle φ_r. The calculations were performed for a Bessel beam with an OAM projection of $m_l = 1$, $\lambda = 1$, $\omega = 2.65$ eV and an opening angle of $\theta_k = 7.53°$.

And then, after some simple algebra, we can rewrite the unit vectors $\boldsymbol{\xi}_{0,\pm1}$ with the cylindrical unit vectors as

$$\boldsymbol{\xi}_{+1} = -\frac{1}{\sqrt{2}}\left(\boldsymbol{e}_x + i\boldsymbol{e}_y\right) = -\frac{1}{\sqrt{2}}\, e^{+i\varphi_r}\left(\boldsymbol{e}_{r_\perp} + i\boldsymbol{e}_{\varphi_r}\right), \tag{2.45a}$$

$$\boldsymbol{\xi}_{-1} = +\frac{1}{\sqrt{2}}\left(\boldsymbol{e}_x - i\boldsymbol{e}_y\right) = +\frac{1}{\sqrt{2}}\, e^{-i\varphi_r}\left(\boldsymbol{e}_{r_\perp} - i\boldsymbol{e}_{\varphi_r}\right), \tag{2.45b}$$

$$\boldsymbol{\xi}_0 = \boldsymbol{e}_z\,. \tag{2.45c}$$

By making use of these expressions we can express the vector potential $\boldsymbol{\mathcal{A}}^{(\mathrm{tw})}_{m_\gamma\lambda}(\boldsymbol{r},t)$ in cylindrical coordinates

$$\boldsymbol{\mathcal{A}}^{(\mathrm{tw})}_{m_\gamma\lambda}(\boldsymbol{r}) = \boldsymbol{e}_{r_\perp}\mathcal{A}^{(\mathrm{tw})}_{r_\perp}(\boldsymbol{r},t) + \boldsymbol{e}_{\varphi_r}\mathcal{A}^{(\mathrm{tw})}_{\varphi_r}(\boldsymbol{r},t) + \boldsymbol{e}_z\mathcal{A}^{(\mathrm{tw})}_{z}(\boldsymbol{r},t)\,, \tag{2.46}$$

where the components $\mathcal{A}^{(\mathrm{tw})}_{r_\perp}(\boldsymbol{r},t)$, $\mathcal{A}^{(\mathrm{tw})}_{\varphi_r}(\boldsymbol{r},t)$, and $\mathcal{A}^{(\mathrm{tw})}_{z}(\boldsymbol{r},t)$ are given by

$$\mathcal{A}^{(\mathrm{tw})}_{r_\perp}(\boldsymbol{r},t) = i\, e^{i(k_z z-\omega t)}\, e^{im_\gamma\varphi_r}\Big(J_{m_\gamma+1}(k_\perp r_\perp)\, c_{-1} + J_{m_\gamma-1}(k_\perp r_\perp)\, c_{+1}\Big), \tag{2.47a}$$

$$\mathcal{A}^{(\mathrm{tw})}_{\varphi_r}(\boldsymbol{r},t) = e^{i(k_z z-\omega t)}\, e^{im_\gamma\varphi_r}\Big(J_{m_\gamma+1}(k_\perp r_\perp)\, c_{-1} - J_{m_\gamma-1}(k_\perp r_\perp)\, c_{+1}\Big), \tag{2.47b}$$

$$\mathcal{A}^{(\mathrm{tw})}_{z}(\boldsymbol{r},t) = e^{i(k_z z-\omega t)}\, e^{im_\gamma\varphi_r}\, J_{m_\gamma}(k_\perp r_\perp)\, c_0\,. \tag{2.47c}$$

The electric field components can be calculated by using the relation $\boldsymbol{E}^{(\mathrm{tw})}(\boldsymbol{r},t) = -\frac{\partial}{\partial t}\,\boldsymbol{\mathcal{A}}^{(\mathrm{tw})}(\boldsymbol{r},t)$ and the above Eqs. (2.47)

$$E_{r_\perp}^{(\mathrm{tw})}(\boldsymbol{r},t) = -\omega\, e^{i(k_z z-\omega t)}\, e^{im_\gamma\varphi_r}\Big(J_{m_\gamma+1}(k_\perp r_\perp)\, c_{-1} + J_{m_\gamma-1}(k_\perp r_\perp)\, c_{+1}\Big)\,, \tag{2.48a}$$

$$E_{\varphi_r}^{(\mathrm{tw})}(\boldsymbol{r},t) = i\omega e^{i(k_z z-\omega t)}\, e^{im_\gamma\varphi_r}\Big(J_{m_\gamma+1}(k_\perp r_\perp)\, c_{-1} - J_{m_\gamma-1}(k_\perp r_\perp)\, c_{+1}\Big)\,, \tag{2.48b}$$

$$E_z^{(\mathrm{tw})}(\boldsymbol{r},t) = i\omega e^{i(k_z z-\omega t)}\, e^{im_\gamma\varphi_r}\, J_{m_\gamma}(k_\perp r_\perp)\, c_0\,. \tag{2.48c}$$

Next, by means of the relation $\boldsymbol{B}^{(\mathrm{tw})}(\boldsymbol{r},t) = \nabla\times\boldsymbol{\mathcal{A}}^{(\mathrm{tw})}(\boldsymbol{r},t)$, we can determine the components of the magnetic field as

$$B_{r_\perp}^{(\mathrm{tw})}(\boldsymbol{r},t) = i\lambda\omega\, e^{i(k_z z-\omega t)}\, e^{im_\gamma\varphi_r}\Big(J_{m_\gamma+1}(k_\perp r_\perp)\, c_{-1} + J_{m_\gamma-1}(k_\perp r_\perp)\, c_{+1}\Big)\,, \tag{2.49a}$$

$$B_{\varphi_r}^{(\mathrm{tw})}(\boldsymbol{r},t) = \lambda\omega\, e^{i(k_z z-\omega t)}\, e^{im_\gamma\varphi_r}\Big(J_{m_\gamma+1}(k_\perp r_\perp)\, c_{-1} - J_{m_\gamma-1}(k_\perp r_\perp)\, c_{+1}\Big)\,, \tag{2.49b}$$

$$B_z^{(\mathrm{tw})}(\boldsymbol{r},t) = \lambda\omega\, e^{i(k_z z-\omega t)}\, e^{im_\gamma\varphi_r}\, J_{m_\gamma}(k_\perp r_\perp)\, c_0\,. \tag{2.49c}$$

If we compare Eqs. (2.47), (3.1a), and (2.49), we find the following connections between the vector potential, the electric, and the magnetic field

$$\boldsymbol{E}^{(\mathrm{tw})}(\boldsymbol{r},t) = -\frac{\partial}{\partial t}\,\boldsymbol{\mathcal{A}}^{(\mathrm{tw})}(\boldsymbol{r},t) = i\omega\,\boldsymbol{\mathcal{A}}^{(\mathrm{tw})}(\boldsymbol{r},t)\,, \tag{2.50a}$$

$$\boldsymbol{B}^{(\mathrm{tw})}(\boldsymbol{r},t) = \nabla\times\boldsymbol{\mathcal{A}}^{(\mathrm{tw})}(\boldsymbol{r},t) = -i\lambda\,\boldsymbol{E}^{(\mathrm{tw})}(\boldsymbol{r},t)\,. \tag{2.50b}$$

In the following subsection, we will use these results and investigate the intensity profile of twisted Bessel beams.

2.4.3 Intensity Profile of Bessel Beams

In Sec. 2.4.1, we have seen that the wavefronts of a twisted Bessel beam are helical shaped, the phase profile depends on the azimuthal angle φ_r, and results in a phase singularity. As we are about to observe, these phase properties affect the intensity, too. In order to analyze the transverse intensity distribution of twisted Bessel beams within the paraxial approximation, we make use of relation (2.13). Therefore, to calculate the Poynting vector, we need the expressions for the electric and magnetic field components, which we derived in the previous section. Thus, we are ready now, to calculate the Poynting vector $\boldsymbol{S}(\boldsymbol{r})$, which, in the cylindrical coordinates, $(r_\perp,\varphi_r,z)$, reads as

$$\boldsymbol{S}(\boldsymbol{r}) = \boldsymbol{e}_{r_\perp}S_{r_\perp}(\boldsymbol{r}) + \boldsymbol{e}_{\varphi_r}S_{\varphi_r}(\boldsymbol{r}) + \boldsymbol{e}_z S_z(\boldsymbol{r})\,. \tag{2.51}$$

With the help of Eqs. (3.1a) and (2.49) we can compute the components of the (time-averaged) Poynting vector, $\boldsymbol{S}(\boldsymbol{r}) = \frac{1}{4\pi\alpha}\,\mathrm{Re}\Big(\boldsymbol{E}(\boldsymbol{r})\times\boldsymbol{B}^*(\boldsymbol{r})\Big)$[c.f. Eq. (2.13)], which

are then given by (see also [35, 60])

$$\boldsymbol{S}_{r_\perp}(\boldsymbol{r}) = 0\,, \tag{2.52a}$$

$$\boldsymbol{S}_{\varphi_r}(\boldsymbol{r}) = \frac{\omega^2}{4\pi\,\alpha}\sin\theta_k\, J_{m_\gamma}(k_\perp r_\perp)\,, \tag{2.52b}$$

$$\boldsymbol{S}_z(\boldsymbol{r}) = \frac{\omega^2}{4\pi\,\alpha}\left(\cos^4\left(\frac{\theta_k}{2}\right) J^2_{m_\gamma-\lambda}(\varkappa r_\perp) - \sin^4\left(\frac{\theta_k}{2}\right) J^2_{m_\gamma+\lambda}(\varkappa r_\perp)\right)\,, \tag{2.52c}$$

where $c^2_{+1} = \cos^4\left(\frac{\theta_k}{2}\right)$ and $c^2_{+1} = \sin^4\left(\frac{\theta_k}{2}\right)$.
As already mentioned in Sect.2.2, the Poynting vector represents the energy flow of the light beam. We can obtain from Eq. (2.52a), that the radial component of the Poynting vector vanishes for the case of a twisted Bessel beam. This is the reason, why Bessel beams are non-diffractive [35]. Moreover, the energy flow trough the plane, which is transverse to the propagation direction, can be described by $S_z(\boldsymbol{r})$. The absolute value of this energy flux distribution is proportional to the transverse intensity profile $I_z(\boldsymbol{r})$ of the Bessel beam (2.14). In the left panel of Fig. 2.3 we present the transverse intensity profile obtained for a Bessel beam with an OAM of $m_l = 1$, $\lambda = 1$, $\omega = 2.65$ eV and an opening angle of $\theta_k = 7.53^\circ$. The figure depicts the typical ring structure with an intensity minimum in the beam center, which is in strong contrast to the homogenous intensity profile of plane waves, c.f. Fig. 2.1. Due to these characteristics, these beams are also called *doughnut* or *vortex beams*.

In the next chapter, we will explain how to characterize the polarization state of a light beam and how linear polarized light can be constructed from circular ones. We will perform the analysis for both cases, plane-wave and twisted light radiation. For the latter case, we will also investigate spatially inhomogeneous states of polarization, namely radially and azimuthally polarized Bessel beams.

Chapter 3

Polarization

In the previous chapter, we introduced twisted Bessel beams. As explained, they are constructed in the *circular polarization basis*. In this chapter, we will discuss how various types of polarization can be constructed on this basis. In order to do so, firstly, we give a brief introduction to the theory of polarization. This will lead us to the Stokes parameters, which are one possibility to measure the polarization and which completely characterize the polarization state of a light wave. Using these parameters we apply the concept on plane waves and explain the characterization of different polarization states by the Poincaré sphere. Afterwards, we will proceed with the analysis of polarization for twisted light beams. We will see that these states are more complicated. In contrast to the plane-wave case, this evaluation is more complicated because polarization of OAM beams is a local quantity and depends on the particular point within the beam front. Such beams with a space-variant polarization are called *vector beams* [61–63]. At the end of this section, we will explain how to characterize them by a so-called *higher-order Poincaré sphere* [61].

3.1 Introduction

Polarization is one of the basic properties of light. It refers to the fact that light is a transverse electromagnetic wave: only transverse waves can be polarized – longitudinal waves, such as sound waves, do not exhibit polarization.

In the previous chapter, we have shown that the electric and magnetic field of an electromagnetic wave are oscillating mutually perpendicular and also perpendicular to the propagation direction. Thus, polarization is a property of transverse waves, specifying the geometrical direction of the oscillations of the electric field. If light is said to be in a state of linear polarization, the oscillations are restricted to a single direction, whereas for light, which is circularly or elliptically polarized, the vector of the electric field rotates. Oscillations of the electric and the magnetic field, which are mutually perpendicular, lie in a plane orthogonal to the propagation direction.

3.2 Stokes Parameters

As mentioned in Chapter 2, the optical field in free space can be described by the wave equation (2.6). If we assume the light is propagating along the z direction, the electric field is confined in the xy-plane. In general, the electric field is complex, however, only the real part of $\boldsymbol{E}$ is physically accessible. Therefore, these transverse components of the optical field for a plane wave are given by [64]

$$E_x(z,t) = \mathrm{Re}[E_{0x}\, e^{i\delta_x}\; e^{i(kz-\omega t+\delta_x)}]\,, \tag{3.1a}$$

$$E_y(z,t) = \mathrm{Re}[E_{0y}\, e^{i\delta_y}\; e^{i(kz-\omega t+\delta_y)}]\,, \tag{3.1b}$$

where E_{0x} and E_{0y} are the maximum amplitudes of the electric field components and δ_x and δ_y are arbitrary phases. By combing these two equations, one can eliminate the propagator $kz - \omega t$ and obtain the expression for the *polarization ellipse* [65]

$$\frac{E_x(z,t)^2}{E_{0x}^2} + \frac{E_y(z,t)^2}{E_{0y}^2} - 2\frac{E_x(z,t)E_y(z,t)}{E_{0x}E_{0y}}\cos\delta = \sin^2\delta, \tag{3.2}$$

where $\delta = \delta_y - \delta_x$ is the phase difference between the x- and y-component of the electric field. This polarization ellipse is shown in Fig. 3.1. It describes a generally (elliptically) polarized beam and is characterized by two angles, the orientation angle ψ and the ellipticity angle χ, which are defined as follows [64]

$$\tan 2\psi = \frac{2E_{0x}E_{0y}}{E_{0x}^2 - E_{0y}^2}\cos\delta\,, \qquad 0 \le \psi \le \pi\,, \tag{3.3a}$$

$$\sin 2\chi = \frac{2E_{0x}E_{0y}\sin\delta}{E_{0x}^2 + E_{0y}^2}\,, \qquad -\frac{\pi}{4} \le \chi \le \frac{\pi}{4}\,. \tag{3.3b}$$

The polarization ellipse is one method to visualize the polarization of light. However, for its derivation the propagator was eliminated. Therefore, the ellipse remains fixed with respect to its orientation and shape [64], and there are two main limitations of the polarization ellipse: Firstly, light beams oscillate with high frequencies. Thus, a single period is in a time interval of the order of a few seconds and its actual polarization ellipse cannot be observed. The second limitation is that the polarization ellipse can only characterize completely polarized light, but not partially polarized nor unpolarized light.

There is, however, another possibility to overcome these limitations and characterize the polarization of light with the observables of the polarized field. As seen from the two field components, (3.1a) and (3.1b), three independent quantities are needed to characterize the polarization states, namely two amplitudes, E_{0x} and E_{0y}, and the phase difference δ. For practical reasons, it is convenient to use the so-called *Stokes parameters*. They were introduced by George G. Stokes in 1852 [66] and can

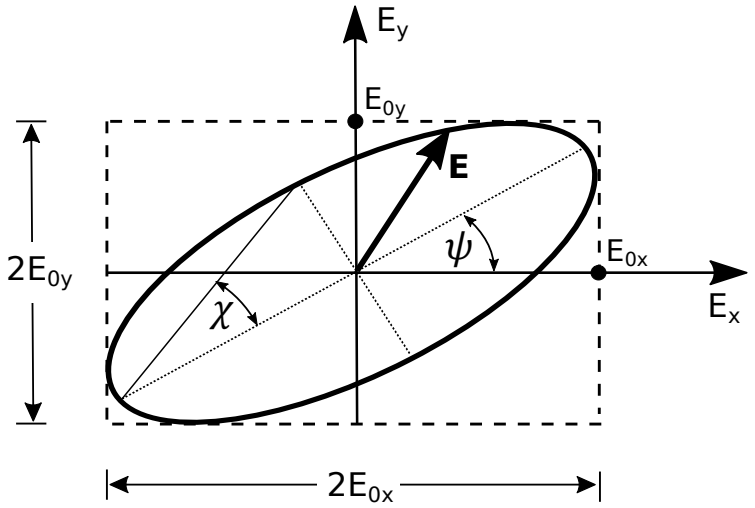

FIGURE 3.1: Polarization ellipse. The end point of the propagating electric field vector $\boldsymbol{E}$ follows, in general, an elliptical trajectory in the xy-plane. This ellipse is parametrized by two angles, namely, the orientation angle ψ and the ellipticity angle χ, which are defined in the text. E_{0x} and E_{0y} are the maximum amplitudes of the x and the y electric field component, respectively.

be derived from the polarization ellipse (3.2): The experimentally accessible quantities are not the amplitudes of the field but the time-averaged squares of the field amplitudes, i.e. the field intensities [64], which are defined as

$$\left\langle E_i(z,t)E_j(z,t)\right\rangle = \lim_{T\to\infty}\frac{1}{T}\int_0^T E_i(z,t)\,E_j(z,t)\,dt\,, \quad i,j=x,y\,, \tag{3.4}$$

where T is the averaging time, i.e. the time needed for the measurement. One can easily obtain that

$$\begin{aligned}\left\langle E_i(z,t)^2\right\rangle &= \frac{1}{2}\,E_{0i}^2\,,\\ \left\langle E_i(z,t)\,E_j(z,t)\right\rangle &= \frac{1}{2}\,E_{0i}\,E_{0j}\,\cos\delta\,.\end{aligned} \tag{3.5}$$

By inserting these results in the time-averaged equation of the polarization ellipse (3.2), we get after some simple algebra

$$2\,E_{0x}^2\,E_{0y}^2 + 2\,E_{0x}^2\,E_{0y}^2 - (2\,E_{0x}\,E_{0y}\cos\delta)^2 = (2\,E_{0x}\,E_{0y}\sin\delta)^2\,. \tag{3.6}$$

And, since we want to describe intensity and polarization, a term like $E_{0x}^2\,E_{0y}^2$ should be in the formula so that we rewrite this expression as

$$(E_{0x}^2+E_{0y}^2)^2 - (E_{0x}^2-E_{0y}^2)^2 - (2\,E_{0x}\,E_{0y}\cos\delta)^2 = (2\,E_{0x}\,E_{0y}\sin\delta)^2\,, \tag{3.7}$$

where each of the terms in parentheses is given through one of the Stokes parameters for a plane wave, namely

$$S_0 = E_{0x}^2 + E_{0y}^2 , \tag{3.8a}$$

$$S_1 = E_{0x}^2 - E_{0y}^2 , \tag{3.8b}$$

$$S_2 = 2\, E_{0x}\, E_{0y} \cos\delta , \tag{3.8c}$$

$$S_3 = 2\, E_{0x}\, E_{0y} \sin\delta . \tag{3.8d}$$

The four Stokes parameters completely characterize the polarization properties of an optical field [67]. Above, we have stressed that only three parameters are needed. Indeed, the first parameter, S_0, is simply the incident intensity, and the others S_1, S_2, and S_3 specify the state of polarization: The second one, S_1, indicates the amount the intensity of parallel polarization ($S_1 > 0$) exceeds the intensity of perpendicular polarization ($S_1 < 0$). S_2 determines the excess of $+45^\circ$ polarization intensity ($S_2 > 0$) versus of the -45° polarization intensity ($S_2 < 0$). And the last parameter S_3 estimates the excess of intensity in the ratio of right ($S_3 > 0$) to left circularly polarized light ($S_3 > 0$). It is convenient to normalize the Stokes parameters by dividing each one of them by S_0, and arrange the three (normalized) parameters in the so-called *Stokes* vector

$$\boldsymbol{S} = \frac{1}{S_0} \begin{pmatrix} S_1 \\ S_2 \\ S_3 \end{pmatrix} , \tag{3.9}$$

where "0"-th parameter is obliviously identity and dropped. In Fig. 3.2 the common polarization states of light are shown: The electric field vectors in the first column are depicted for parallel (top) and perpendicular (bottom) linearly polarized states. Parallel and perpendicular refer to the xz-plane, i.e. parallelly polarized light oscillates along the x-axis. If the light is linearly polarized, but the $\boldsymbol{E}$-vector is rotated by $\pm 45^\circ$ with respect to the x-axis (2nd column), the corresponding Stokes vectors are $\boldsymbol{S} = (0, \pm 1, 0)$. The third column accounts left (top) and right (bottom) polarization, which are related with $\boldsymbol{S} = (0, 0, \pm 1)$. And, the last two figures, depict examples for elliptically polarized plane waves.

In order to overcome the time integration (3.4) the Stokes Parameters can be expressed in the *complex representation* [68]. They can be defined either in terms of the linear polarization basis or in the circular polarization basis. Since, as mentioned above, dealing with twisted light, it is more appropriate to use the circular one. In

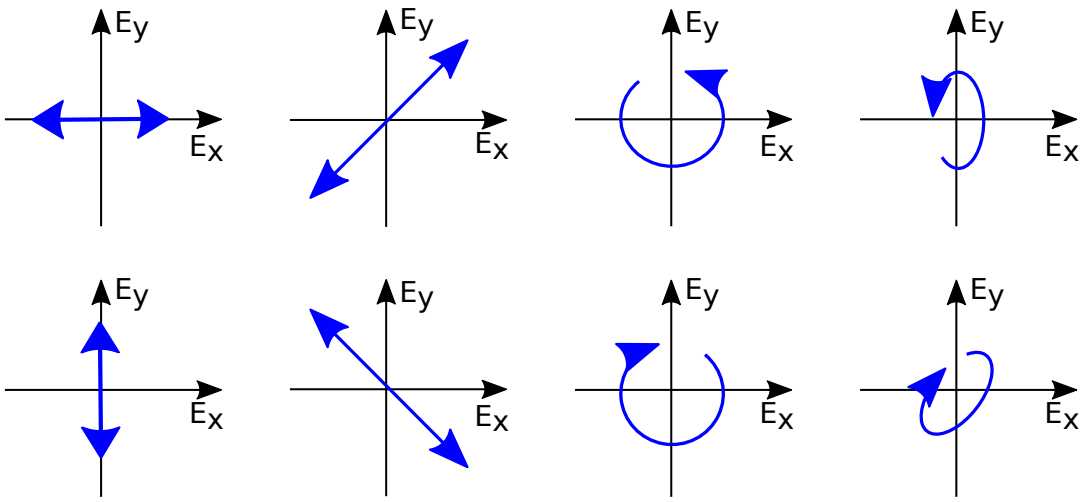

FIGURE 3.2: Illustration of polarization states. The considered states are: parallel (top) and perpendicular (bottom) linearly (1st column), +45° (top) and -45° linearly (2nd column), left (top) and right (bottom) circularly (3rd column) polarized plane waves. In the last column are two examples for elliptically polarized light shown.

the circular polarization basis, the Stokes Parameters read [45]

$$S_0 = \left|\boldsymbol{e}^*_{\boldsymbol{k}+} \cdot \boldsymbol{E}(\boldsymbol{r},t)\right|^2 + \left|\boldsymbol{e}^*_{\boldsymbol{k}-} \cdot \boldsymbol{E}(\boldsymbol{r},t)\right|^2, \tag{3.10a}$$

$$S_1 = 2\,\mathrm{Re}\left[\left(\boldsymbol{e}^*_{\boldsymbol{k}+} \cdot \boldsymbol{E}(\boldsymbol{r},t)\right)^* \left(\boldsymbol{e}^*_{\boldsymbol{k}-} \cdot \boldsymbol{E}(\boldsymbol{r},t)\right)\right], \tag{3.10b}$$

$$S_2 = 2\,\mathrm{Im}\left[\left(\boldsymbol{e}^*_{\boldsymbol{k}+} \cdot \boldsymbol{E}(\boldsymbol{r},t)\right)^* \left(\boldsymbol{e}^*_{\boldsymbol{k}-} \cdot \boldsymbol{E}(\boldsymbol{r},t)\right)\right], \tag{3.10c}$$

$$S_3 = \left|\boldsymbol{e}^*_{\boldsymbol{k}+} \cdot \boldsymbol{E}(\boldsymbol{r},t)\right|^2 - \left|\boldsymbol{e}^*_{\boldsymbol{k}-} \cdot \boldsymbol{E}(\boldsymbol{r},t)\right|^2, \tag{3.10d}$$

where the scalar products $\boldsymbol{e}^*_{\boldsymbol{k}+} \cdot \boldsymbol{E}$ and $\boldsymbol{e}^*_{\boldsymbol{k}-} \cdot \boldsymbol{E}$ are the amplitudes of radiation with positive and negative helicity. Note that in the circularly polarized basis the complex conjugate of the polarization vectors $\boldsymbol{e}^*_{\boldsymbol{k}+}$ must be used.

In the next section, we will introduce the *Poincaré sphere*, which is a useful method to visualize the states of polarization.

3.3 Poincaré Sphere

In the previous section, the Stokes parameters were introduced. We have explained this is a possibility to express the polarization state in terms of observables. However, there is another useful tool to classify the various polarization states visually: the *Poincaré sphere*. This method was suggested by Henri Poincaré (1892) [69] in order to overcome the difficulties of the polarization ellipse – as we have noted above, it is only possible to describe fully polarized light with the ellipse. The Poincaré

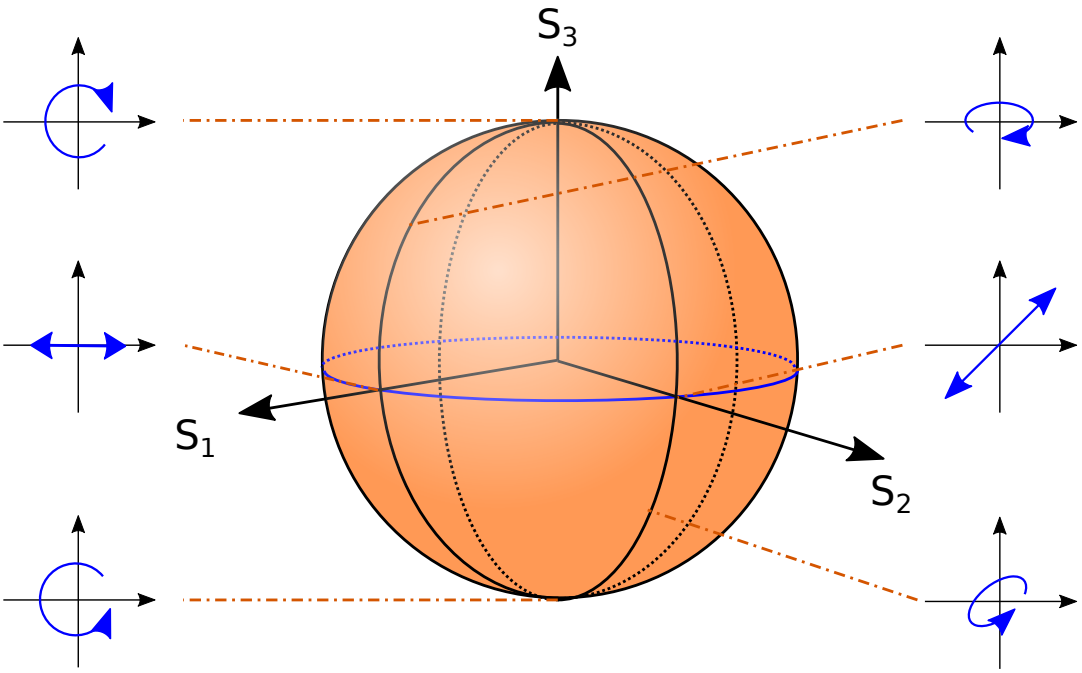

FIGURE 3.3: Poincaré sphere. The axes of the sphere are the Stokes parameters S_1, S_2, and S_3, where the radius is given by $S_0 = 1$. Fully polarized states lie on the surface of the sphere. The poles correspond to right and left circular polarization states, all states with linear polarization lie on the equator and intermediate elliptical states.

sphere is shown in Fig. 3.3. It is a unit sphere, spanned by the three (normalized) Stokes parameters S_1, S_2, and S_3, i.e. the radius is defined by S_0 and the three axes of the Cartesian coordinate system are given by S_1, S_2, and S_3. Each point on the surface of the sphere represents one fully-polarized state. While partially-polarized states are located inside of the sphere. Linearly polarized states lie on the equator, circularly polarized states can be found on the poles of the sphere, and all intermediate points are associates with elliptical polarization.

Having explained the various polarization states and how to describe them, we will discuss in the next section, how to construct them from a circular polarization basis.

3.4 Vector Potential for Linearly Polarized Beams

3.4.1 Linearly Polarized Plane Waves

The vector potential $\boldsymbol{\mathcal{A}}_{\boldsymbol{k}\lambda}^{(\mathrm{pl})}$ (2.10) was derived for a particular helicity λ of light, which corresponds to left or right circular polarization [48]. However, we want also study atomic excitations induced by linearly polarized light, which is used in many experiments and important for a large class of applications. In order to do so, we remind,

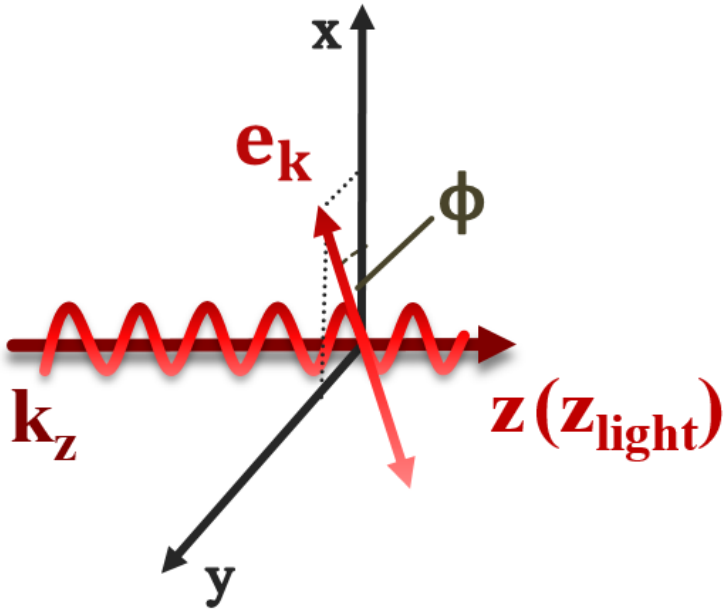

FIGURE 3.4: Orientation of the electric field vector for linearly polarized light. The linearly polarized light beam propagates along the $z(z_{\text{light}})$-axis. ϕ denotes the tilt of the polarization vector $\boldsymbol{e}_{\boldsymbol{k}}$ with respect to the xz-plane.

that any polarization vector $\boldsymbol{e}_{\boldsymbol{k}}$ can be expanded in terms of unit vectors in the circular polarization basis $\boldsymbol{e}_{\boldsymbol{k}\lambda}$ [41]. At this point, it is worth to make a small comment on the used notations: Since we are going to analyze various polarization states, we will use $\boldsymbol{e}_{\boldsymbol{k}}$ for a polarization vector describing arbitrary polarization, and $\boldsymbol{e}_{\boldsymbol{k}\lambda}$, as in the previous chapter, for the case when the helicity is fixed, i.e. for circularly polarization. However, the explicit form of this expansion depends on the definition of the basis used to describe $\boldsymbol{e}_{\boldsymbol{k}}$. By using the convention of Rose (2.11), the vector potential for linearly polarized plane waves can be written as a superposition of two circularly polarized beams (2.10) with opposite helicity and has the following form

$$\boldsymbol{\mathcal{A}}^{(\text{pl})}_{\text{lin}}(\boldsymbol{r}) = \frac{1}{\sqrt{2}} \sum_{\lambda=\pm 1} e^{-i\lambda\phi} \boldsymbol{\mathcal{A}}^{(\text{pl})}_{\boldsymbol{k}\lambda}(\boldsymbol{r})\,, \tag{3.11}$$

where ϕ denotes the tilt of the polarization vector $\boldsymbol{e}_{\boldsymbol{k}}$ with respect to the plane, which is spanned by the x- and z-axis, see Fig. 3.4. Later in Sec. 6.4 we will see that this plane can also be defined by means of the quantization axis for the light (z_{light}) and the quantization axis for the atom (z_{atom}), which is determined by the orientation of an external $\boldsymbol{B}$-field.

For $\phi = 0$ the linearly polarized light (3.11) is parallel to the xz-plane (see Fig. 3.4). The vector potential for this *parallel* polarized plane wave is then given as

$$\boldsymbol{\mathcal{A}}^{(\text{pl})}_{\parallel}(\boldsymbol{r}) = \frac{1}{\sqrt{2}} \left(\boldsymbol{\mathcal{A}}^{(\text{pl})}_{\boldsymbol{k}\lambda=+1}(\boldsymbol{r}) + \boldsymbol{\mathcal{A}}^{(\text{pl})}_{\boldsymbol{k}\lambda=-1}(\boldsymbol{r}) \right) = \boldsymbol{e}_x\, e^{ikz}\,. \tag{3.12}$$

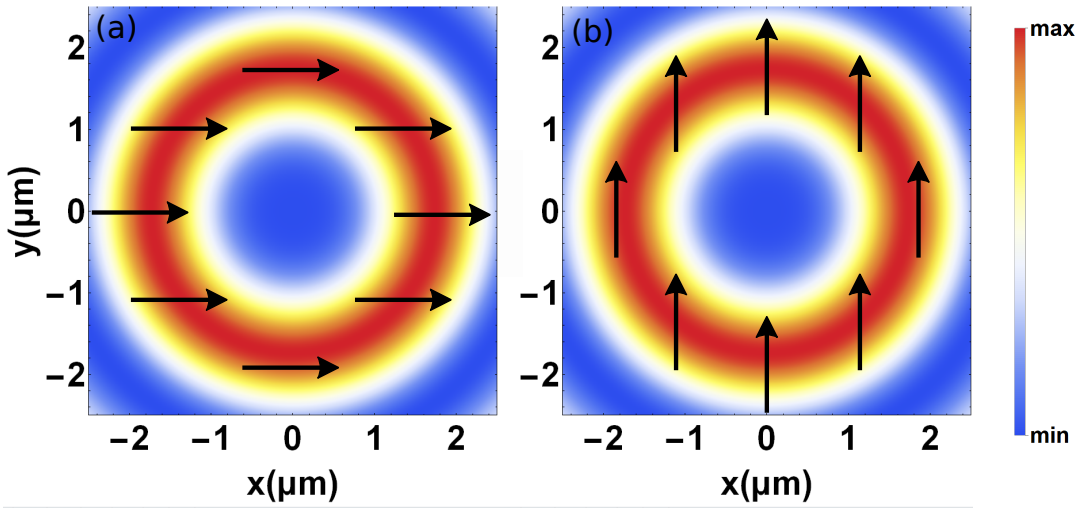

FIGURE 3.5: Intensity profiles of twisted Bessel beams of light of photon energy $\hbar\omega = 2.65$ eV with an opening angle $\theta_k = 7.53°$. The directions of the electric field are indicated by black arrows. The parallel (a) and perpendicular (b) linearly polarized twisted beams have an OAM of $m_l = 2$. The figures are taken from our publication, Ref. [70].

The plane wave linearly polarized perpendicular to the xz-plane can be obtained in a similar way, by taking $\phi = \frac{\pi}{2}$, so that

$$\boldsymbol{\mathcal{A}}^{(\mathrm{pl})}_{\perp}(\boldsymbol{r}) = \frac{i}{\sqrt{2}}\left(-\boldsymbol{\mathcal{A}}^{(\mathrm{pl})}_{\boldsymbol{k}\lambda=+1}(\boldsymbol{r}) + \boldsymbol{\mathcal{A}}^{(\mathrm{pl})}_{\boldsymbol{k}\lambda=-1}(\boldsymbol{r})\right) = \boldsymbol{e}_y\, e^{ikz}\,. \tag{3.13}$$

3.4.2 Linearly Polarized Twisted Light

In analogy with plane waves, the twisted light in the paraxial approximation can be linearly polarized [2]. In Sec. 2.4.1 we have seen that in the paraxial regime, where the transverse momentum $\varkappa$ of the photons is much smaller than the longitudinal one, $\varkappa \ll k_z$, the OAM and SAM decouple and the Bessel waves have a well-defined OAM of $m_l = m_\gamma - m_s$ and SAM of $m_s = \lambda$.

Then, it is possible to construct the vector potential for linear polarized twisted photons as a superposition of two beams with the same OAM projection m_l but opposite helicity, so that

$$\boldsymbol{\mathcal{A}}^{(\mathrm{tw})}_{\mathrm{lin}}(\boldsymbol{r}) = \frac{1}{\sqrt{2}}\sum_{\lambda=\pm1}(-i)^{\lambda}e^{-i\lambda\phi}\boldsymbol{\mathcal{A}}^{(\mathrm{tw})}_{m_l\lambda}(\boldsymbol{r}). \tag{3.14}$$

Again, as in the plane-wave description, ϕ denotes the tilt of the polarization vector $\boldsymbol{e}_{\boldsymbol{k}}$ with respect to the xz-plane, see Fig. 3.4. But, in contrast to Eq. (3.11), which describes states of general linear polarization for plane waves, in this expression the

additional phase factor $(-i)^\lambda$ is needed. The reason for this factor originates from the definition of the vector potential, (2.33) and (2.38), for a twisted Bessel beam (see also Eq. (2.34) and in Ref. [71]). The need of $(-i)^\lambda$ in Eq. (3.14) can be explained as follows. If we take the plane-wave limit, i.e. $\varkappa \to 0$ and therefore also $\theta_k \to 0$, $\boldsymbol{\mathcal{A}}^{(\mathrm{tw})}_{\mathrm{lin}}(\boldsymbol{r})$ should match the plane-wave form $\boldsymbol{\mathcal{A}}^{(\mathrm{pl})}_{\mathrm{lin}}(\boldsymbol{r})$.

If we chose the angle as $\phi = 0$, the twisted light is linearly polarized parallel to the xz-plane and the vector potential reads as

$$\boldsymbol{\mathcal{A}}^{(\mathrm{tw})}_{\parallel}(\boldsymbol{r}) = \frac{i}{\sqrt{2}}\left(\boldsymbol{\mathcal{A}}^{(\mathrm{tw})}_{m_l\lambda=+1}(\boldsymbol{r}) - \boldsymbol{\mathcal{A}}^{(\mathrm{tw})}_{m_l\lambda=-1}(\boldsymbol{r})\right) = \boldsymbol{e}_x\, J_{m_l}(\varkappa r_\perp)\, e^{im_l\varphi_k}\, e^{ik_z z} \tag{3.15}$$

and for $\phi = \dfrac{\pi}{2}$ the light is perpendicularly polarized and has got the following vector potential

$$\boldsymbol{\mathcal{A}}^{(\mathrm{tw})}_{\perp}(\boldsymbol{r}) = \frac{1}{\sqrt{2}}\left(\boldsymbol{\mathcal{A}}^{(\mathrm{tw})}_{m_l\lambda=+1}(\boldsymbol{r}) + \boldsymbol{\mathcal{A}}^{(\mathrm{tw})}_{m_l\lambda=-1}(\boldsymbol{r})\right) = \boldsymbol{e}_y\, J_{m_l}(\varkappa r_\perp)\, e^{im_l\varphi_k}\, e^{ik_z z}\,. \tag{3.16}$$

Figs. 3.5 depicts for parallelly (a) and perpendicularly (b) polarized twisted beams with an OAM of $m_l = 2$ the intensity profiles and the directions of the $\boldsymbol{E}$-vectors: the electric field, defined by vector potential $\boldsymbol{\mathcal{A}}^{(\mathrm{tw})}_{\parallel}$ (3.15), is always parallel to the xz-plane defined by the magnetic field direction and the light propagation direction, whereas the electric field for a twisted beam with $\boldsymbol{\mathcal{A}}^{(\mathrm{tw})}_{\perp}$ (3.16) is always perpendicular to the xz-plane, i.e. parallel to the yz-plane.

3.5 Vector Potential for Radially and Azimuthally Polarized Twisted Light

Apart from circular (2.38) and linear (3.15)-(3.16) polarizations, light beams can have radial and azimuthal polarizations [72]. In fact, such beams are linear combinations of two circularly polarized twisted beams with helicity $\lambda = \pm 1$ and OAM $m_l = \mp 1$ [73]. The vector potential of the radially polarized beam is defined as

$$\boldsymbol{\mathcal{A}}^{(\mathrm{tw})}_{\mathrm{r}}(\boldsymbol{r}) = -\frac{i}{\sqrt{2}}\left(\boldsymbol{\mathcal{A}}^{(\mathrm{tw})}_{m_l=-1\,\lambda=+1}(\boldsymbol{r}) + \boldsymbol{\mathcal{A}}^{(\mathrm{tw})}_{m_l=+1\,\lambda=-1}(\boldsymbol{r})\right) = \boldsymbol{e}_r\, J_1(\varkappa r_\perp)\, e^{ik_z z}\,. \tag{3.17}$$

The azimuthally polarized beam in turn can be written in the following form

$$\boldsymbol{\mathcal{A}}^{(\mathrm{tw})}_{\mathrm{az}}(\boldsymbol{r}) = \frac{1}{\sqrt{2}}\left(\boldsymbol{\mathcal{A}}^{(\mathrm{tw})}_{m_l=+1\,\lambda=-1}(\boldsymbol{r}) - \boldsymbol{\mathcal{A}}^{(\mathrm{tw})}_{m_l=-1\,\lambda=+1}(\boldsymbol{r})\right) = \boldsymbol{e}_\phi\, J_1(\varkappa r_\perp)\, e^{ik_z z}\,. \tag{3.18}$$

In Figs. 3.6 (a) and (b) illustrate the intensity profile and directions of the electric field vector for radially and azimuthally polarized beams. For radially polarized light the electric field vector points at any point in the beam profile radially outwards. And

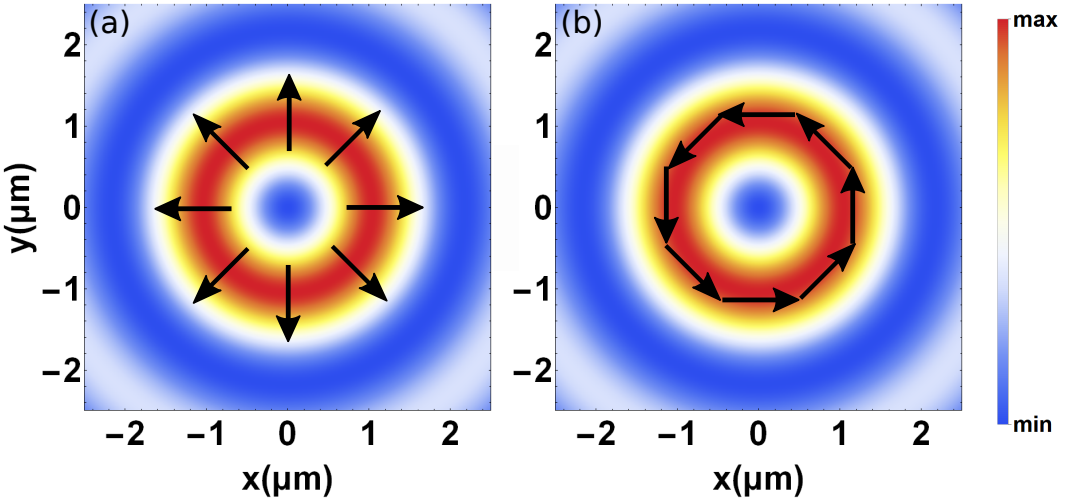

FIGURE 3.6: Intensity profiles of (a) radially and (b) azimuthally polarized beams with an OAM of $m_l = \pm 1$. The directions of the electric field are indicated by black arrows. All other parameters are as in Fig. 3.5. The figures are taken from our publication, Ref. [70].

if the beam is azimuthally polarized, the electric field vector is perpendicular to the radial axis.

In Chapter 1, two methods have been described to produce vortex light beams, namely spiral phase plates (cf. Fig. 1.1) and fork-like holograms (see Fig. 1.2). Also, radially and azimuthally polarized beams can be generated experimentally. There are various options. For example, space-variant dielectric gratings [74], polarization converter [75], or segmented phase plates [76, 77] can be used to create these states of polarization. Another method is to superpose two vortex beams [78]. The output will then depend on the topological charges and the helicities of both beams used for the superposition, similar as explained above. Thus, for radial and azimuthal polarization, the initial beams must have an OAM projection of $m_l = \pm 1$. However, with those methods also other higher-order vector beams with arbitrary polarization can be created.

In the next chapter, we show, how these states of polarization can be characterized and described by means of *higher order Poincaré spheres*.

3.6 Higher-Order Poincaré Sphere

In Sect. 3.3 we have introduced the Poincaré sphere. Each polarization state of a plane wave can be described as a point of the sphere's surface, if the light is completely polarized. Otherwise, the point is located inside the sphere. However, the representation of polarization states by the Poincaré sphere is limited to spatially homogeneous polarization, so-called *scalar* polarization [61, 79].

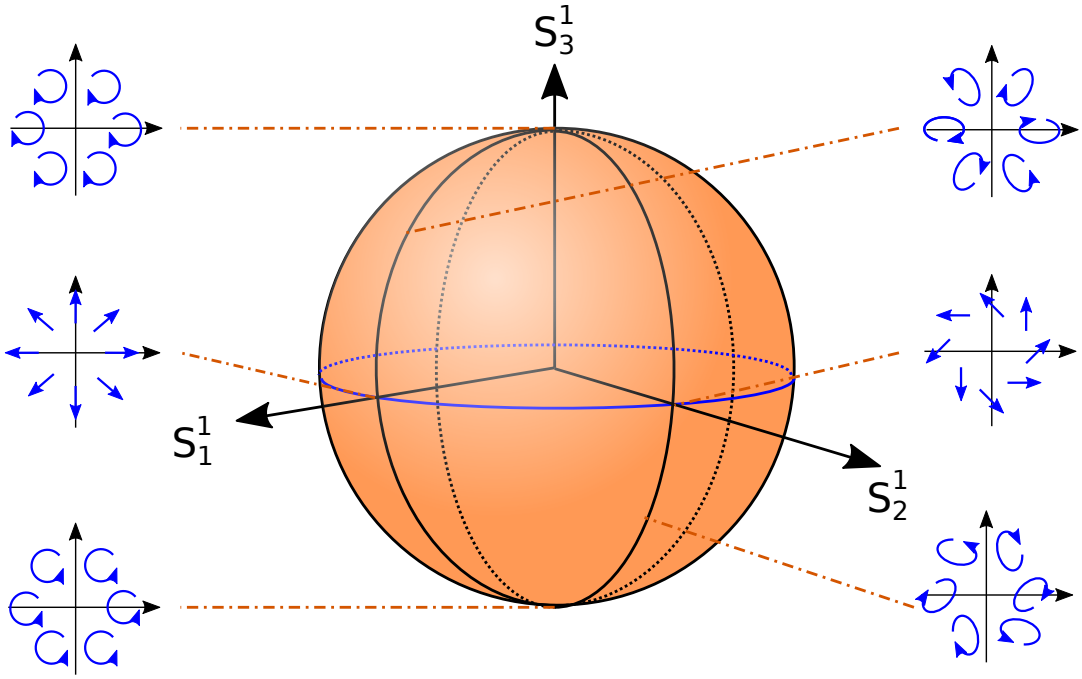

FIGURE 3.7: Higher-Order Poincaré Sphere (HOPS). The axes of the sphere are the higher-order Stokes parameters $S_1^{m_l}$, $S_2^{m_l}$ and $S_{3^{m_l}}$ of order m_l, where the radius is given by $S_0^l = 1$. Here the representation for a sphere of order $m_l = +1$ is shown. The poles correspond to right and left circular polarization states. While states that are (locally) linear polarized lie on the equator, elliptically polarized states can be found in between the poles and the equator.

As we have seen in the previous sections, there are states of polarization with a spatially inhomogeneous polarization pattern, which is why they are also known as *vector beams*. For those beams, the concept of the *higher-order Poincaré sphere* was developed. In this section, we will present its main ideas.

Based on the electric field, or with property $\boldsymbol{E}^{(\mathrm{tw})}(\boldsymbol{r},t) = -\frac{\partial}{\partial t}\boldsymbol{\mathcal{A}}^{(\mathrm{tw})}(\boldsymbol{r},t)$ also based on the vector potential, the polarization properties of Bessel beams are defined. The polarization states of twisted light beams are not constant within the plane transverse to the propagation direction. Therefore, also the Stokes parameters are position-dependent and Milione et al. introduced so-called *higher-order Stokes parameters* [61]. Like the *normal* Stokes parameters, they can be defined either in the linear polarization basis or in the circular one [45]. As mentioned above, dealing with twisted light, it is more appropriate to use the circular one. In this case, the

definitions for these higher-order Stokes parameters of order m_l read as

$$S_0^{m_l}(\boldsymbol{r}) = |\mathbf{u}_{\mathbf{k},+}^* \cdot \mathbf{E}_{\varkappa m_l}^{(\mathrm{tw})}(\boldsymbol{r})|^2 + |\mathbf{u}_{\mathbf{k},-}^* \cdot \mathbf{E}_{\varkappa m_l}^{(\mathrm{tw})}(\boldsymbol{r})|^2 , \tag{3.19a}$$

$$S_1^{m_l}(\boldsymbol{r}) = 2\,\mathrm{Re}\left[(\mathbf{u}_{\mathbf{k},+}^* \cdot \mathbf{E}_{\varkappa m_l}^{(\mathrm{tw})}(\boldsymbol{r}))^* (\mathbf{u}_{\mathbf{k},-}^* \cdot \mathbf{E}_{\varkappa m_l}^{(\mathrm{tw})}(\boldsymbol{r}))\right] , \tag{3.19b}$$

$$S_2^{m_l}(\boldsymbol{r}) = 2\,\mathrm{Im}\left[(\mathbf{u}_{\mathbf{k},+}^* \cdot \mathbf{E}_{\varkappa m_l}^{(\mathrm{tw})}(\boldsymbol{r}))^* (\mathbf{u}_{\mathbf{k},-}^* \cdot \mathbf{E}_{\varkappa m_l}^{(\mathrm{tw})}(\boldsymbol{r}))\right] , \tag{3.19c}$$

$$S_3^{m_l}(\boldsymbol{r}) = |\mathbf{u}_{\mathbf{k},+}^* \cdot \mathbf{E}_{\varkappa m_l}^{(\mathrm{tw})}(\boldsymbol{r})|^2 - |\mathbf{u}_{\mathbf{k},-}^* \cdot \mathbf{E}_{\varkappa m_l}^{(\mathrm{tw})}(\boldsymbol{r})|^2 . \tag{3.19d}$$

Comparing these parameters with the previous ones (3.10), they appear identical at first glance. What is different, however, is that the coordinates and the topological charge are also given here: The polarization states of a vector beam can be described with a *higher-order Poincaré sphere* of order m_l, which is constructed using the normalized parameters, $S_1^{m_l}$, $S_2^{m_l}$, and $S_3^{m_l}$, as (Cartesian) coordinates of the sphere [61]. There is another sphere for each topological charge. The characterization of the polarization state due to these parameters is similar as for the plane-wave case: Points on the equator represent states with (local) linear polarization, i.e. $S_3^{m_l}$ vanishes, the poles depict circular and all intermediate points between the poles and the equator elliptical polarization. Twisted light beams are at least solutions of the paraxial Helmholtz wave equation [79]. Bessel beams, the type of twisted light to which we limit ourselves in this work, are even solutions from the *general* (non-paraxial) Helmholtz equation (c.f. Sec. 2.4). Anyway, all are solutions of the paraxial Helmholtz equation, and therefore, the spatial polarization pattern does not change during the light propagation [79].

In the following, we present how the two polarization states, radial and azimuthal, can be characterized by a higher-order Poincaré sphere of order $m_l = +1$. Let us start with radially polarized vortex beams. In Sec. 3.5 we have derived the expression for the corresponding vector potential (3.17) and in addition we have shown its intensity profile together with the electric filed vectors in Fig. 3.6 (a).

With the help of the vector potential, the higher-order Stokes parameters can be calculated. In Fig. 3.8 we display the distributions of the three higher-order Stokes parameters, S_1^1, S_2^1, and S_3^1, for a radially polarized Bessel beam, which were calculated within the plane transverse to the propagation direction. The third parameter, S_3^1, vanishes for all points. This indicates, that the analyzed states lie on the equator of the Poincaré sphere (c.f. Fig. 3.7). As seen from the two other panels, the values change with the azimuthal angle. These two parameters indicate that this light beam is radially polarized: The perpendicular cones in the middle of S1 are red, indicating local perpendicular polarization, whereas the blue ones denote parallel polarization. For the second parameter, the pattern is rotated by 45°. This is also in line with the pattern that we determined in Sec. 3.5: Fig. 3.6 (a) shows that the vector points diagonally into the corners of the picture. Therefore, S_2^1 has to be equal to ± 1 in these positions.

The analysis of azimuthal polarization follows the same scheme as before for the

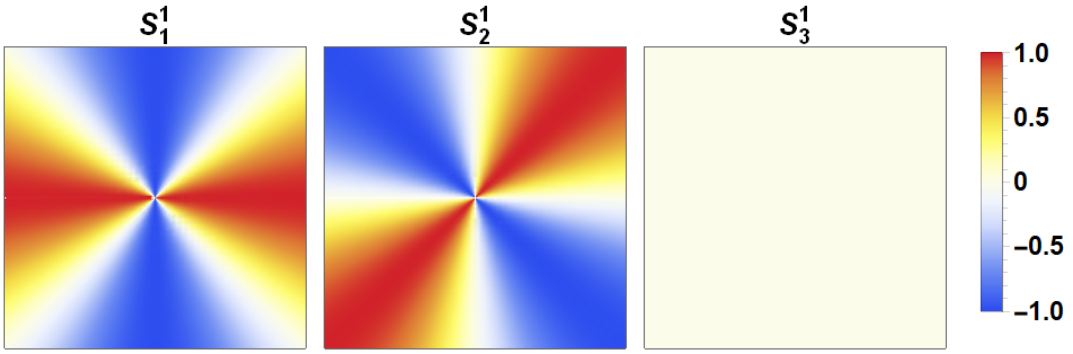

FIGURE 3.8: Higher-order Stokes parameters. The three panels depict the three (normalized) higher-order Stokes parameter of order $m_l = 1$ for a radially polarized Bessel beam. The local variation of the values can clearly be seen for S_1^1 and S_2^1. The third parameter, S_3^1, equals everywhere zero. This indicates, that the analyzed states are located on the equator of the (higher-order) Poincaré sphere (c.f. Fig. 3.7). Looking at the other two parameters reveals that it is radially polarized light: The vertical cones in the middle of S1 are blue (-1), indicating (local) perpendicular polarization, whereas the red ones (+1) denote (local) parallel polarization.

radially. The distributions of all three parameters are shown in Fig. 3.9. Again, S_3^1, vanishes everywhere. Therefore, this state of polarization lies also on the equator of the Poincaré sphere, but directly opposite the point that characterizes the radial polarization (Fig. 3.7). From the comparison with Fig. 3.8 is visible, that the patterns of the first two parameters, S_1^1 and S_2^1, are the same as in Fig. 3.8, but rotated by 90°. Thus, the electric field vector must also be rotated by 90°. This is in good agreement with the result presented in Fig. 3.6 (b). The electric field vectors form a circle around the beam center.

Vector beams are defined by spatially inhomogeneous states of polarization, i.e. the spatial distribution and the polarization state of the beam are non-separable [63]. The two analyzed states are examples of linear polarized vector beams. That means taking a closer look, that the electric field vector points in different directions throughout the plane but do not change locally at a fixed point. However, there are also vector beams with a non-zero $S_3^{m_l}$ parameter. Then, the state of polarization is not only spatially inhomogeneous, but now also the field vectors rotate locally, see Fig. 3.7, when the beam propagates.

We will conclude this chapter with a brief discussion of the time evolution for a polarized Bessel beam.

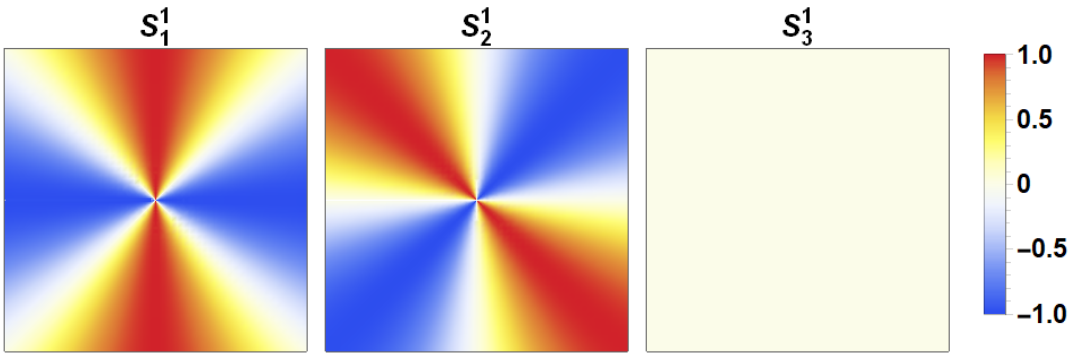

FIGURE 3.9: Higher-order Stokes parameters. The three panels depict the three (normalized) higher-order Stokes parameter of order $m_l = 1$ for an azimuthally polarized Bessel beam. Again, this can be seen from the first two panels: the maximum (+1: parallel) and minimum values (-1: perpendicular) are for S_1^1 on the vertical or horizontal lines, respectively, and for S_2^1 on the diagonals. This polarization states lies on the equator, because S_3^1 vanishes in all points.

3.7 Time Evolution of the Electric Field Distribution

Above we have mentioned that the polarization, which can be measured in the experiments, is time-averaged. However, in this section we want to analyze the time evolution of the electric field distribution over one period. We assume a harmonic time evolution, i.e. then the time evolution of the vector potential is given by $\boldsymbol{\mathcal{A}}(\boldsymbol{r}, t) = \boldsymbol{\mathcal{A}}(\boldsymbol{r})e^{-i\omega t}$ (2.7). Fig. 3.10 shows the time evolution of the electric field vector over one period at a fixed point plane $z = 0$ for a perpendicular linearly polarized Bessel beam. The field distribution is divided into four parts and it can clearly be seen that they are all rotating 360° around the beam center within one period. If one looks at a fixed single point in the xy- plane, it can be noticed that the field vector also changes its direction there during a period. After taking the time-average, one gets the result shown in Fig. 3.5 (b).

Exemplary, we have shown the time evolution for a perpendicular linearly polarized Bessel beam with an OAM of $m_l = 2$ here because one can imagine the behaviour of the different polarizations: For perpendicularly polarized Bessel beams the tip of the electric field vector points either to the left or to the right. In the case of radially polarized light all vectors within the plane point to the center or to the outside at a fixed time. And it views similar for azimuthally polarized beams, then all vectors form a circle in a clockwise or anti-clockwise direction.

But there is another difference. As seen in Fig. 3.10 the field is divided into four parts. In the shown case the light carries an OAM of $m_l = 2$. For higher topological charge, there are more divisions, namely $2\,m_l$.

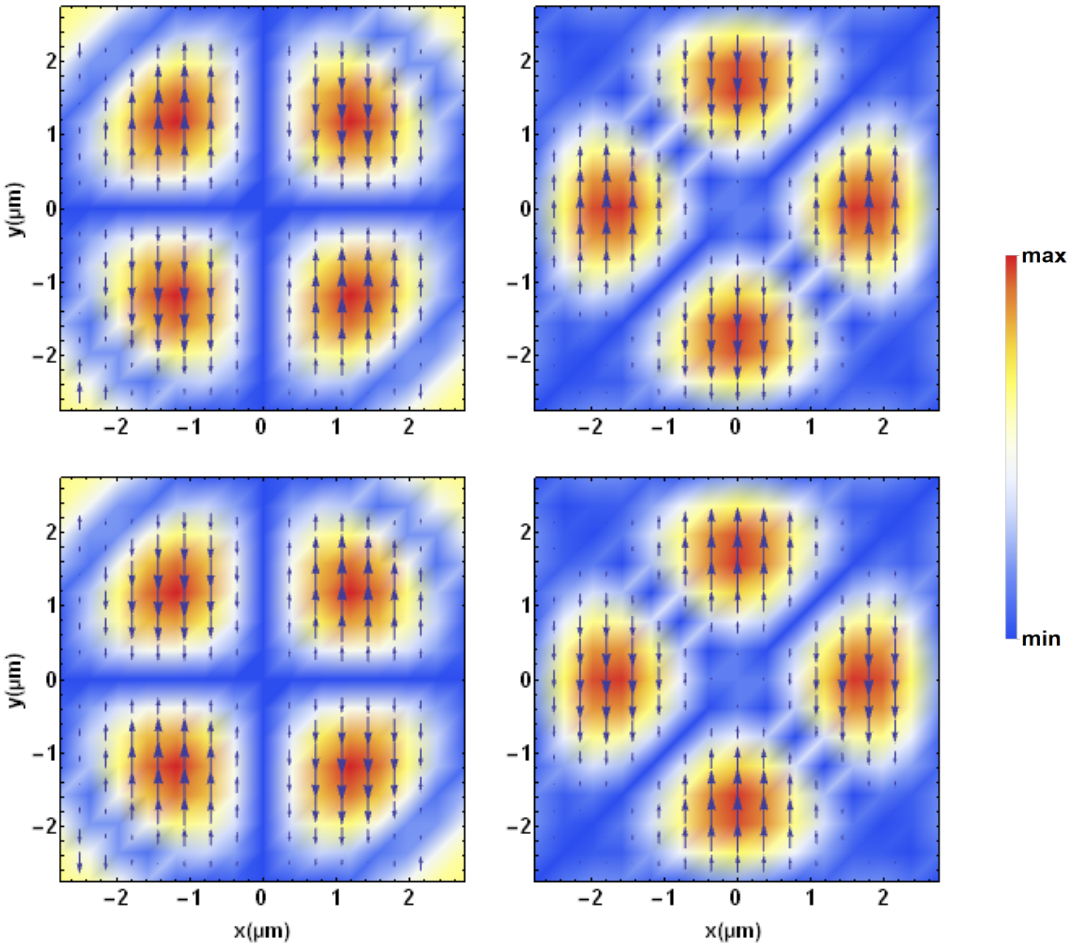

FIGURE 3.10: Electric field polarization. Time evolution of the electric field vector over one period at a fixed point plane $z = 0$ is shown for a perpendicular linearly polarized Bessel beam with an OAM of $m_l = +2$. The first figure (left upper panel) depicts the electric field distribution at $t = 0$, the second (right upper panel) for $t = \frac{1}{4}T$, the third (left lower panel) for $t = \frac{1}{2}T$, and the last one (right lower panel) for $t = \frac{3}{4}T$. The field distribution is divided into four parts and it can clearly be seen that they are all rotating 360° around the beam center within one period. Observing a fixed single point in the xy-plane, it can be determined that the field vector changes its direction at this point during a period.

Chapter 4

Atom-Light Interaction

So far, we have discussed how to describe different types of light, as well as various polarizations states. In this study, however, we want to analyze the photoexcitation of a single atom. Therefore, we still need to explain how to describe the atomic states and the interaction between the light and the atom. In order to do so, we make use of the so-called *density matrix theory*.

The density matrix formalism was introduced by John von Neumann in 1927 [80] to describe the statistical concept in quantum mechanics. Initially, the use of this method was mainly limited to statistical physics [81], but later in the middle of the 1950s, the applications of the theory have been gaining importance in many other fields of physics, for example, in modern scattering theory, optical pumping, and laser physics [81, 82]. With the concept of the *statistical tensors* Ugo Fano developed the density matrix theory in atomic physics [83]. Nowadays, this formalism is widely established in modern quantum physics.

However, since the theory and the applications of the density matrix and the statistical tensors have been summarized in many works, for example in [82–84], we will not go into all the details here, but we will outline the basic relations in the first part of this chapter, in Sec. 4.1.

Afterwards, we will focus on the interaction process between the light and the atom. To do so, we will use the (time-dependent) first-order perturbation theory. This is a well-established theory, that is of course often discussed. Therefore, we will just present the main ideas of this theory for a relativistic system in Sec. 4.2. On this basis, we will derive the matrix element for the photoabsorption in Sec. 4.3 in general, and we will then apply this method in the next Sec. 4.4. There we will examine the matrix elements and transition rates for the excitation of a single atom, which is induced by plane-wave or twisted radiation. Moreover, we will consider the realistic experimental case, when the atom is not well-localized and its position is only known with some uncertainty. Finally, at the end of this chapter, in Sec. 4.5, we will have a closer look at the section rules, where we have again to distinguish between the plane-wave and the twisted light case.

4.1 Density Matrix Formalism

A state of an atomic system needs to be described quantum mechanically. Basically, there are two possibilities. The first is to characterize the state with a single wave function (or state vector) $|\phi\rangle$. However, this is only possible, if the system is in a *pure* state. If the quantum system is in a statistical mixture of different (pure) states, it is said to be in a *mixed* quantum state [82–84]. To describe mixed quantum states the so-called *statistical* (or density) operators are used, which are superpositions of N pure states and have the general form [82, 85]

$$\hat{\rho} = \sum_{k=1}^{N} p_k \left|\varphi_k\right\rangle \left\langle\varphi_k\right| \ , \tag{4.1}$$

where $\{|\varphi_k\rangle\}$ is a set of states vectors and the N statistical weights p_k are non-zero and stratify the relations

$$0 < p_k \leq 1 \ , \text{ and } \quad \sum_{k=1}^{N} p_k = 1 \, . \tag{4.2a}$$

In this work, we want to analyze the interaction between light and a single atom. Then, the initial statistical operator $\hat{\rho}_i$ is the direct product of the atomic $\hat{\rho}_i^{(\mathrm{at})}$ and photonic $\hat{\rho}_i^{(\mathrm{ph})}$ operator

$$\hat{\rho}_i = \hat{\rho}_i^{(\mathrm{at})} \otimes \hat{\rho}_i^{(\mathrm{ph})} \, . \tag{4.3}$$

If the target atom is initially unpolarized the statistical operator $\hat{\rho}_i^{(\mathrm{at})}$ reads as follows

$$\hat{\rho}_i^{(\mathrm{at})} = \frac{1}{2J_i+1} \sum_{M_i=-J_i}^{J_i} \left|\alpha_i J_i M_i\right\rangle \left\langle\alpha_i J_i M_i\right| . \tag{4.4}$$

After the interaction the system is in the final state, characterized by operator $\hat{\rho}_f$, which can be expressed by using the initial state $\hat{\rho}_i$ and the transition operator $\widehat{\mathcal{T}}$

$$\hat{\rho}_f = \widehat{\mathcal{T}} \hat{\rho}_i \widehat{\mathcal{T}}^{\dagger} \, . \tag{4.5}$$

For the further analysis, it is convenient to write (4.5) in matrix form [86]

$$\begin{aligned} \left\langle \alpha_f J_f M_f \right| \hat{\rho}_f \left| \alpha_f J_f M_f' \right\rangle \ &= \ \frac{1}{2J_i+1} \sum_{M_i=-J_i}^{J_i} \left\langle \gamma_i \right| \hat{\rho}^{(ph)} \left| \gamma_i \right\rangle \\ &\times \left\langle \alpha_f J_f M_f \right| \widehat{\mathcal{T}} \left| \alpha_i J_i M_i, 1_{\gamma_i} \right\rangle \left\langle \alpha_i J_i M_i, 1_{\gamma_i} \right| \widehat{\mathcal{T}}^{\dagger} \left| \alpha_f J_f M_f' \right\rangle . \end{aligned} \tag{4.6}$$

Here $\left\langle \alpha_f J_f M_f \right| \widehat{\mathcal{T}} \left| \alpha_i J_i M_i, 1_{\gamma_i} \right\rangle$ is the matrix element, which represents the amplitude for the transition $\left|\alpha_i J_i M_i\right\rangle + \gamma_i \rightarrow \left|\alpha_f J_f M_f\right\rangle$ [85]. We see with this formula it is possible to describe different atomic processes. However since we are interested in the photoabsorption, the attention within this thesis will be paid to the transition matrix

element $\langle \alpha_f J_f M_f | \, \widehat{\mathcal{T}} \, | \alpha_i J_i M_i, 1_{\gamma_i} \rangle$. Nevertheless, all observables properties can be derived from the density matrix of the final state $\hat{\rho}_f$, if the correct projections are used [87]. For example, the diagonal elements ρ_{jj} of a density matrix $\hat{\rho}$ (4.1) have a direct physical interpretation. They correspond to the probability p_j of finding the system in the corresponding state

$$\rho_{jj} = \langle \varphi_j | \, \hat{\rho} \, | \varphi_j \rangle = p_j \, . \tag{4.7}$$

In the following of this chapter, we mainly focus on the evaluation of this transition matrix element.

4.2 (Relativistic) First-Order Perturbation Theory

It will be the object of the present section to explain, the dynamical behaviour of the atomic system. For simplicity, we restrict the discussion to an atom with a single electron. The treatment of the motion of the electrons requires a relativistic quantum mechanical description [88]. In order to do so, we use the time-dependent first-order perturbation theory. Since this has been discussed many times in the literature (see e.g. in [47, 55, 85, 89]), we outline here only the basic ideas that are needed for further evaluation. The dynamics of the relativistic electron can be described with the Dirac equation

$$i \frac{\partial \Psi(t)}{\partial t} = \widehat{H}_D \Psi(t) \, . \tag{4.8}$$

Here $\widehat{H}_D$ is the Dirac Hamiltonian for an electron being bound in the spherically symmetric potential $V(\boldsymbol{r})$ of the atomic nucleus and given by

$$\widehat{H}_D = \frac{1}{\alpha} \boldsymbol{\alpha} \cdot \boldsymbol{p} + \frac{1}{\alpha^2} \beta + V(\boldsymbol{r}) \mathbb{1} \, , \tag{4.9}$$

where $\boldsymbol{\alpha}$ denotes the vector of the $4x4$ Dirac matrices, $\beta = \mathrm{diag}[1, 1, -1, -1]$, and $\boldsymbol{p}$ is the four-momentum of the electron. The eigenfunctions $\Psi_{i,f}$ of $\hat{H}_D$ in Eq. (4.8) are four-component wave functions, the so-called *Dirac spinors* (for more details see [47]).

4.2.1 Interaction picture

Let us now consider the case when the atom interacts with an external field. The interaction between the atom and an external field can be described by the following Hamiltonian

$$\widehat{H}_I(\boldsymbol{r}) = -\frac{1}{\alpha} \boldsymbol{\alpha} \cdot \boldsymbol{\mathcal{A}}(\boldsymbol{r}), \tag{4.10}$$

through the vector potential $\boldsymbol{\mathcal{A}}(\boldsymbol{r})$.

In the following, we want to find transitions between the solutions (bound states) $\Psi_{i,f}$ of the eigenvalue problem (4.8), which are induced by the perturbation trough $\widehat{H}_I$. For this purpose, it is convenient to solve this perturbation problem in the *interaction picture*, where both the states and the operators are time-dependent. The time evolution in this representation for a state $\Psi(t)$ is given by

$$i\frac{\partial\Psi(t)}{\partial t} = \widehat{H}_I(t)\Psi(t)\,, \tag{4.11}$$

where $\widehat{H}_I(t)$ is the time-dependent interaction Hamiltonian

$$\widehat{H}_I(t) = e^{i\hat{H}_D t}\widehat{H}_I e^{-i\hat{H}_D t}\,. \tag{4.12}$$

Let us introduce the unitary propagation operator $\widehat{U}(t,t_0)$, which describes the time-evolution of a state Ψ at time $t = t_0$

$$\Psi(t) = \widehat{U}(t,t_0)\Psi(t_0). \tag{4.13}$$

We can use this expression (4.13) to further determine $\widehat{U}(t,t_0)$. From

$$i\frac{\partial\widehat{U}(t,t_0)\Psi(t_0)}{\partial t} = \widehat{H}_I(t)\widehat{U}(t,t_0)\Psi(t_0) \tag{4.14}$$

follows that also the operator $\widehat{U}(t,t_0)$ satisfies the following two properties

$$i\frac{\partial\widehat{U}(t,t_0)}{\partial t} = \widehat{H}_I(t)\widehat{U}(t,t_0), \tag{4.15a}$$

$$\widehat{U}(t_0,t_0) = \widehat{\mathbb{1}}\,, \tag{4.15b}$$

where $\widehat{\mathbb{1}}$ is the identity operator. The iterative solution [47] of

$$\widehat{U}(t,t_0) = \widehat{\mathbb{1}} - i\int_{t_0}^{t} d_{t_1}\widehat{H}_I(t)\widehat{U}(t_1,t_0) \tag{4.16}$$

is

$$\widehat{U}(t,t_0) = \sum_{n=0}^{\infty}(-i)^n\int_{t_0}^{t} d_{t_1}\widehat{H}_I(t_1)\int_{t_0}^{t_1} d_{t_2}\widehat{H}_I(t_2)\cdots\int_{t_0}^{t_{n-1}} d_{t_n}\widehat{H}_I(t_n). \tag{4.17}$$

The S operator

$$\widehat{S} = \widehat{U}(\infty,-\infty) \tag{4.18}$$

transforms the initial $|\Psi_i\rangle$ asymptotic states ($t = -\infty$) to final $|\Psi_f\rangle$ asymptotic states ($t = \infty$), where, in both cases (for $t = \pm\infty$), $\widehat{H}_I$ is assumed to vanish. The first-order transition amplitude is then given by [47]

$$S_{fi}^{(1)} = \left\langle\Psi_f\left|S^{(1)}\right|\Psi_f\right\rangle = -i\int_{-\infty}^{\infty} dt\left\langle\Psi_f\left|e^{i\hat{H}_D t}\hat{H}_I e^{-i\hat{H}_D t}\right|\Psi_i\right\rangle. \tag{4.19}$$

4.3 Matrix Element and Transition Probability for Photoabsorption

Let us consider a two-level atom that interacts with electromagnetic radiation. We assume a one-photon absorption. Therefore, we can write Eq. (4.19) as

$$\begin{aligned} S_{fi}^{(1)} &= -i\int_{-\infty}^{\infty} dt e^{i(E_f-E_i-\omega)t}\left\langle \Psi_f \left|\hat{H}_I\right| \Psi_i\right\rangle \\ &= -2\pi i\,\delta(E_f-E_i-\omega)\left\langle \Psi_f \left|\hat{H}_I\right| \Psi_i\right\rangle, \end{aligned} \tag{4.20}$$

where $\left\langle \Psi_f \left|H_I\right| \Psi_i\right\rangle$ is the *transition matrix element*. By inserting the relativistic interaction Hamiltonian H_I (4.10) we obtain the matrix element for photoabsorption

$$\mathcal{M}_{fi} = \left\langle \Psi_f \left|\boldsymbol{\alpha}\cdot\boldsymbol{\mathcal{A}}(\boldsymbol{r})\right| \Psi_i\right\rangle \ . \tag{4.21}$$

The transition probability for the photoexciation from state Ψ_i to state Ψ_f is given by the square of $S_{fi}^{(1)}$ [47]. If we assume that the system is initially in Ψ_i and the electromagnetic radiation field is monochromatic, the probability for the transition per unit time, the *transition rate*, is [47]

$$W_{fi} = \frac{2\pi}{\alpha^2}\,\delta(E_f-E_i-\omega)\left|\left\langle \Psi_f \left|\boldsymbol{\alpha}\cdot\boldsymbol{\mathcal{A}}(\boldsymbol{r})\right| \Psi_i\right\rangle\right|^2 . \tag{4.22}$$

4.4 Matrix Elements and Transition Rates for Excitations of a Single Atom

In the previous section, we derived the general expression of the matrix element for the photoabsorption. In this section, we apply this equation (4.21) to transitions between two fine-structure levels induced by either plane-wave or twisted radiation. For the analysis of interactions with Bessel light, we need to distinguish two cases. On the one hand we study the idealized (theoretical) situation of precise localization of the atom, but on the other hand, in real experiments, this is not the case. There the impact parameter b remains undetermined and can at best be described by some mean value. We derive analytical expressions for the matrix elements and transition rates for different cases.

4.4.1 Excitation by Plane-Wave Photons

First, we shall begin by considering the transition from an initial fine-structure state $|\alpha_i J_i M_i\rangle$ to a final higher-lying state $\left|\alpha_f J_f M_f\right\rangle$ driven by a plane-wave light field $\mathcal{A}_{\boldsymbol{k}\lambda}^{(\mathrm{pl})}$ (2.10). Here $J_{i,f}$ are the total angular momenta, $M_{i,f}$ their projections on the quantization axis (z_{atom}), which is defined by an applied external magnetic field $\boldsymbol{B}$, and $\alpha_{i,f}$ denote all additional quantum numbers. Then, the matrix element (4.21) for

this process has the following form

$$\mathcal{M}_{fi}^{(\mathrm{pl})} = \left\langle \alpha_f J_f M_f \left| \sum_q \boldsymbol{\alpha}_q \cdot \boldsymbol{\mathcal{A}}_{\boldsymbol{k}\lambda}^{(\mathrm{pl})}(\boldsymbol{r}_q) \right| \alpha_i J_i M_i \right\rangle . \tag{4.23}$$

This amplitude describes a transition between many-electron states. The sum in the electron-photon operator $\sum_q \boldsymbol{\alpha}_q \cdot \boldsymbol{\mathcal{A}}_{\boldsymbol{k}\lambda}^{(\mathrm{pl})}$ runs over all q electrons in the atom and $\boldsymbol{\alpha}_q$ denotes the vector of Dirac matrices for the q^{th} electron. We insert the plane-wave vector potential $\boldsymbol{\mathcal{A}}_{\boldsymbol{k}\lambda}^{(\mathrm{pl})}$ expanded in multipoles (2.27), into Eq. (4.23)

$$\begin{aligned} \mathcal{M}_{fi}^{(\mathrm{pl})} &= \sqrt{2\pi} \sum_{LM} \sum_{p=0,1} i^L \, [L]^{1/2} \, (i\lambda)^p \, D_{M\lambda}^{L}(\varphi_k, \theta_k, 0) \\ &\quad \times \left\langle \alpha_f J_f M_f \left| \sum_q \boldsymbol{\alpha}_q \cdot \boldsymbol{a}_{LM}^{(p)}(\boldsymbol{r}_q) \right| \alpha_i J_i M_i \right\rangle . \end{aligned} \tag{4.24}$$

By making use of the Wigner-Eckard theorem [85]

$$\left\langle \alpha_f J_f M_f \left| \boldsymbol{\alpha} \cdot \boldsymbol{a}_{LM}^{(p)} \right| \alpha_i J_i M_i \right\rangle = \frac{\left\langle J_i M_i \, LM \mid J_f M_f \right\rangle}{[J_f]^{1/2}} \left\langle \alpha_f J_f \left\| \boldsymbol{\alpha} \cdot \boldsymbol{a}_{L}^{(p)} \right\| \alpha_i J_i \right\rangle , \tag{4.25}$$

we obtain

$$\begin{aligned} \mathcal{M}_{fi}^{(\mathrm{pl})} &= \sqrt{2\pi} \sum_{LM} \sum_{p=0,1} i^L \, \frac{[L]^{1/2}}{[J_f]^{1/2}} \, (i\lambda)^p \, D_{M\lambda}^{L}(\varphi_k, \theta_k, 0) \\ &\quad \times \left\langle J_i M_i \, LM \mid J_f M_f \right\rangle \left\langle \alpha_f J_f \, || H_\gamma(pL) || \, \alpha_i J_i \right\rangle , \end{aligned} \tag{4.26}$$

where we introduced the shorthand notation

$$\left\langle \alpha_f J_f \, \| H_\gamma(pL) \| \, \alpha_i J_i \right\rangle = \left\langle \alpha_f J_f \left\| \sum_q \boldsymbol{\alpha}_q \cdot \boldsymbol{a}_{L}^{(p)}(\mathbf{r}_q) \right\| \alpha_i J_i \right\rangle . \tag{4.27}$$

Here $\left\langle \alpha_f J_f \left\| \sum_q \boldsymbol{\alpha}_q \cdot \boldsymbol{a}_{L}^{(p)}(\mathbf{r}_q) \right\| \alpha_i J_i \right\rangle$ are the reduced matrix elements. They do neither depend on the magnetic quantum numbers nor on the geometry of the interaction process. They just depend on the properties of the target atom itself.

We assume that the initial atomic state is unpolarized and the magnetic sublevel population of the final state remains unobserved. Then, by taking the modulus squared of the amplitude $\mathcal{M}_{fi}^{(\mathrm{pl})}$ (4.26), we can obtain the rate for the $|\alpha_i J_i\rangle + \gamma_i \rightarrow |\alpha_f J_f\rangle$ excitation of an atom by the plane-wave light [55]

$$W_{fi}^{(\mathrm{pl})} = \frac{2\pi}{[J_i]\alpha^2} \sum_{M_i M_f} \left| \mathcal{M}_{fi}^{(\mathrm{pl})} \right|^2 . \tag{4.28}$$

Since for any quantum number J_i there are $2J_i + 1$ states, the factor $[J_i] = 2J_i + 1$ is used for normalization. Henceforth, we will call this rate (4.28) *total transition rate*. This is due to the fact, that in this expression all multipole orders are considered,

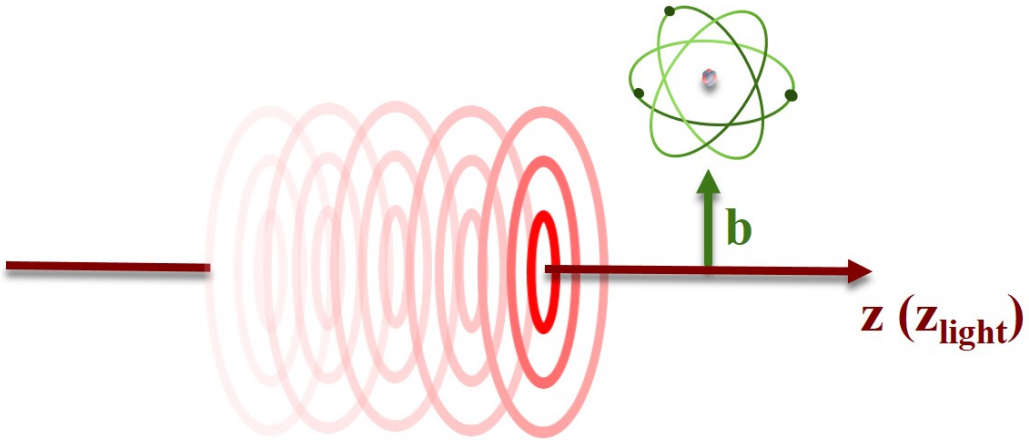

FIGURE 4.1: Geometry for the excitation of a single atom by a Bessel light beam. The quantization z (z_{light}) axis is taken along the propagation direction of the light beam. The atomic position is defined with regard to the beam center, parametrized by the so-called *impact parameter* $\boldsymbol{b}$. Here we assume that the atomic position is well-defined.

which affect the transition. Which multipoles contribute to a transition depends on the initial and final state, as well as on the light type and is determined by the selection rules that will be discussed in the next section.

4.4.2 Excitation by Bessel Beams

After having briefly described the excitation with plane-wave radiation, we can now start the discussion of the interaction between an atom and twisted light (2.30). This interaction process can be described, like in the plane-wave case (4.23), by the transition amplitude, which reads in this case as follows

$$\begin{aligned} \mathcal{M}_{fi}^{(\mathrm{tw})} &= \left\langle \alpha_f J_f M_f \left| \sum_q \boldsymbol{\alpha}_q \cdot \mathcal{A}^{(\mathrm{tw})}(\boldsymbol{r}_q) \right| \alpha_i J_i M_i \right\rangle \\ &= \int a_{\varkappa m_\gamma}(\boldsymbol{k}_\perp) e^{-i\boldsymbol{k}_\perp \cdot \boldsymbol{b}} \left\langle \alpha_f J_f M_f \left| \sum_q \boldsymbol{\alpha}_q \cdot \boldsymbol{e}_{\boldsymbol{k}\lambda} e^{i\boldsymbol{k}\cdot\boldsymbol{r}_q} \right| \alpha_i J_i M_i \right\rangle \frac{d^2\boldsymbol{k}_\perp}{(2\pi)^2} \,. \end{aligned} \tag{4.29}$$

But since the properties of a Bessel beam are position-dependent, we need to specify the position of the target atom by the additional exponential factor $e^{-i\boldsymbol{k}_\perp \cdot \boldsymbol{b}}$. In Sec. 2.4 we have seen that the transverse intensity profile of Bessel beams forms a concentric ring pattern. The impact parameter $\boldsymbol{b} = (b_x, b_y, 0)$ defines the position of the target atom with regard to the central point of this ring structure. The geometry for the photoexcitation of an atom, which is located at a distance $\boldsymbol{b}$ from the light axis, is illustrated in Fig. 4.1.

In analogy to the derivation for the excitation with plane waves, we make use of the multipole expansion (2.27), so that Eq. (4.29) becomes

$$\mathcal{M}_{fi}^{(\mathrm{tw})} = \int \frac{d^2\boldsymbol{k}_\perp}{(2\pi)^2} \sum_{LMp} i^L [L]^{1/2} (i\lambda)^p \, d^L_{LM}(\theta_k) \, \frac{2\pi}{\varkappa} \, (-i)^{m_\gamma} \delta(k_\perp - \varkappa) \times e^{i(m_\gamma - M)\varphi_k} \, e^{-i\boldsymbol{k}_\perp \boldsymbol{b}} \left\langle \alpha_f J_f M_f \left| \sum_q \boldsymbol{\alpha}_q \cdot \boldsymbol{a}^{(\mathrm{p})}_{LM}(\boldsymbol{r}_q) \right| \alpha_i J_i M_i \right\rangle . \quad (4.30)$$

After the application of the Wigner-Eckard theorem (4.25) we perform the integration over the transverse momentum $k_\perp$ by using the Dirac delta function $\delta(k_\perp - \varkappa)$ in Eq. (2.31). With the help of the integral representation for the Bessel function [58]

$$\int_0^{2\pi} e^{i(m_\gamma - M)\varphi_k - i\varkappa b \cos(\varphi_k - \varphi_b)} \frac{d\varphi_k}{2\pi} = (-i)^{m_\gamma - M} \, e^{i(m_\gamma - M)\varphi_b} \, J_{m_\gamma - M}(\varkappa b) \quad (4.31)$$

we can integrate over the azimuthal angle φ_k, and finally obtain the transition amplitude for the $|\alpha_i J_i M_i\rangle + \gamma \to |\alpha_f J_f M_f\rangle$ transition induced by Bessel light

$$\mathcal{M}_{fi}^{(\mathrm{tw})} = \sum_{LM} \sum_{p=0,1} i^{L+M} \, \frac{[L]^{1/2}}{[J_f]^{1/2}} \, (i\lambda)^p d^L_{M\lambda}(\theta_k) \, J_{m_\gamma - M}(\varkappa b) \, \mathrm{e}^{i(m_\gamma - M)\varphi_b} \times \left\langle J_i M_i \, LM \,|\, J_f M_f \right\rangle \left\langle \alpha_f J_f \,||H_\gamma(pL)||\, \alpha_i J_i \right\rangle . \quad (4.32)$$

Again, by taking the modulus squared of the amplitude (4.32) and summing over the magnetic quantum numbers of initial M_i and final states M_f, we derive the total rate for the excitation of atoms by Bessel light

$$W_{fi}^{(\mathrm{tw})} = \frac{2\pi}{[J_i]\alpha^2} \sum_{M_i M_f} \left| \mathcal{M}_{fi}^{(\mathrm{tw})} \right|^2 . \quad (4.33)$$

The normalization for the amplitude of the Bessel wave in Eq. (2.31) was chosen in such a way that expressions of twisted light reach those for plane waves if we take the *plane-wave limit* with $\varkappa \to 0$. Then, the Bessel function in Eq. (2.38) becomes a Dirac delta function, $J_{m_l}(\varkappa r_\perp) \to \delta_{m_l,0}$, and from which directly $\mathcal{M}_{fi}^{(\mathrm{tw})} \xrightarrow{\varkappa \to 0} \mathcal{M}_{fi}^{(\mathrm{pl})}$, and, therefore, $W_{fi}^{(\mathrm{tw})} \xrightarrow{\varkappa \to 0} W_{fi}^{(\mathrm{pl})}$ follows.

4.4.3 Excitation of a Delocalized Atom

So far, we studied the idealized situation, when the target atom is perfectly placed on one point. However, this can not be achieved in real experiments: The impact parameter $\boldsymbol{b}$ is always determined with some uncertainly. Therefore, we now want to study the realistic case of an atom, that is not well-localized. To take such a *delocalization* into account, we assume that the position of the atom is Gaussian distributed,

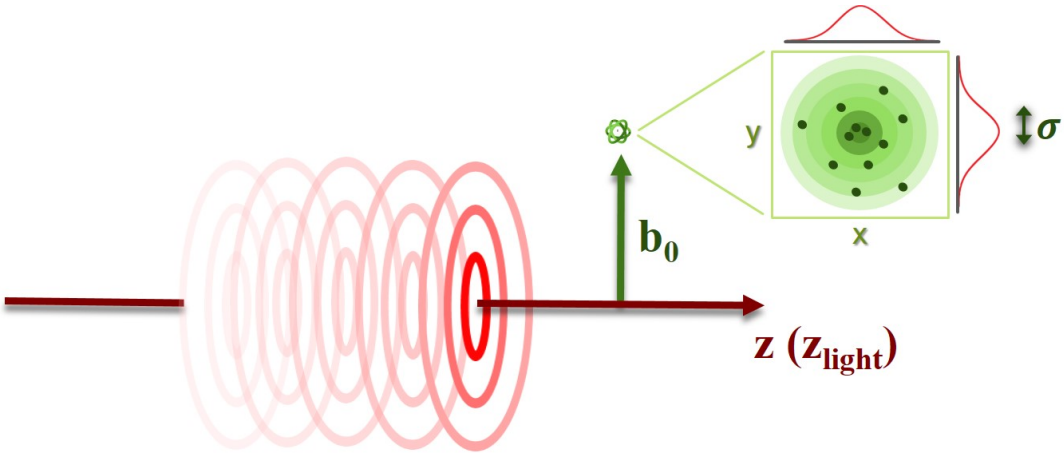

FIGURE 4.2: Geometry for the excitation process in a real experiment, where the position of the atom to be excited by a Bessel light beam is not perfectly known. We assume that the atomic position is Gaussian distributed with the most probable distance b_0 from the beam center. σ is the characteristic width of the distribution. And again, like in Fig. (4.1), the quantization $z(z_{light})$-axis is taken along the propagation direction of the light beam.

c.f. Fig. 4.2, so that its distance b from the center of the beam is given by

$$\begin{aligned} f(\boldsymbol{b};\boldsymbol{b}_0) &= \frac{1}{2\pi\sigma^2}\,\mathrm{e}^{-\frac{(\boldsymbol{b}-\boldsymbol{b}_0)^2}{2\sigma^2}} \\ &= \frac{1}{2\pi\sigma^2}\,\mathrm{e}^{-\frac{b^2+b_0^2-2bb_0\cos\varphi_b}{2\sigma^2}}\,, \end{aligned} \tag{4.34}$$

where $\boldsymbol{b}_0$ is the most likely position of the atom with respect to the beam axis. Moreover it is assumed that the deviations in x- and y-directions are the same: $\sigma_x = \sigma_y = \sigma$. Eq. (4.34) is a two dimensional Gaussian distribution and normalized to one.

Then the *mean* transition rates can be obtained by the integration over the impact parameter $\boldsymbol{b}$

$$W_{fi}^{(\mathrm{tw})}(\boldsymbol{b}_0,\sigma) = \int d^2\boldsymbol{b}\, f(\boldsymbol{b};\boldsymbol{b}_0)\, W_{fi}^{(\mathrm{tw})}(\boldsymbol{b})\,. \tag{4.35}$$

This equation describes the rate for the photoexciation of a delocalized atom (or ion), which has its mean position at point $\boldsymbol{b}_0$ and the transverse distribution σ. We will use this equation later in order to analyze the delocalization of the target atom in the calculations and to understand the importance of localization in experimental realizations.

4.5 Selection Rules

The excitation probability W_{fi} indicates how likely it is that the transition from the initial Ψ_i to the final state Ψ_f will occur. As already mentioned above, the transition matrix element $\mathcal{M}_{fi}$ (4.21) describes the interaction between the atom and the light. Its explicit form depends on the used radiation field and the states to be analyzed. With the help of Eq. (2.27) we expanded the matrix element in multipole terms. The total transition probability is a sum of the magnetic and electronic multipole transition probabilities (see Eqs. (4.28) and (4.33)).

The *selection rules* determine for a given radiation, which multipole transitions between two states are allowed and which are forbidden. These selection rules are derived from the transition matrix elements. A transition is referred to as *forbidden* if the associated multipole transition matrix element vanishes.

In this section, the selection rules for atomic excitations are presented. After a brief reminder on the well-known atomic selection rules for transitions induced by plane waves, it will be discussed how these selection rules are modified, when instead of plane-wave radiation twisted light is used.

4.5.1 Selection Rules for Plane Waves

The transition between two fine-structure states, $|\alpha_i J_i M_i\rangle$ and $|\alpha_f J_f M_f\rangle$, induced by circularly polarized plane-wave radiation is described by the matrix element (4.23). After the multipole expansion and some algebra, we found expression (4.26), which contains a summation over all multipoles. However, here we want to analyze single multipole terms of these matrix elements. In general, the selection rules depend on the orientation of the quantization axis and the propagation direction. Though we will but will begin to derive the well-known selection rules for the plane-wave case, when both, the quantization axis and the propagation direction, are parallel to each other. Then the Wigner-D function in Eq. (4.26) becomes a Dirac's delta function $D^L_{M\lambda}(\varphi_k, \theta_k, 0) = \delta_{M,\lambda}$ [58]. Thus, in each of the multipole terms is a Clebsch-Gordan coefficient of the form $\langle J_i M_i \, L\lambda \mid J_f M_f \rangle$ included. The properties of the Clebsch-Gordan coefficients imply the section rules for the orbital angular momentum

$$\left|J_i - J_f\right| \leq L \leq J_i + J_f \tag{4.36}$$

and for the magnetic quantum numbers

$$\Delta M = M_f - M_i = \lambda \,. \tag{4.37}$$

The parity selection rule

$$\pi_i \pi_f = (-1)^{L+p+1} \tag{4.38}$$

determines the type of the multipole transition, magnetic (p=0) or electric (p=1), where π_i and π_f are the parities of the initial and final atomic state.

4.5.2 Modified Selection Rules

Having discussed the selection rules for plane waves, we may now continue with those for twisted light. In the previous section, we found condition (4.37) for the magnetic quantum numbers. In the plane-wave case, ΔM is limited to 0 and ± 1. However, we will see that this is not the case for twisted light. For this process, now $\mathcal{M}_{fi}^{(\mathrm{tw})}$ (4.32) is the matrix element to be analyzed. Due to the position-dependent properties of the Bessel beam, we must take into account the position of the atom in the selection rules.

Let us start with an atom that is centered on the beam axis ($b = 0$). Then the Bessel function $J_{m_\gamma - M}$, contained in $\mathcal{M}_{fi}^{(\mathrm{tw})}$ (4.32), becomes a Dirac's Delta function $J_{m_\gamma - M}(0) = \delta(m_\gamma, M)$. As a result, we directly receive from the remaining Clebsch-Gordan coefficient, $\langle J_i M_i \, L m_\gamma \mid J_f M_f \rangle$, the following modified selection rule for the magnetic quantum numbers

$$\Delta M = M_f - M_i = m_\gamma. \tag{4.39}$$

m_γ is not limited to $0, \pm 1$, like the plane wave, it just has to be an integer. Therefore, it is possible to drive transitions with ΔM larger than $0, \pm 1$, so that transitions that would be prohibited for plane waves are allowed, if the incident light is twisted.

Moreover, the properties of the Clebsch-Gordan coefficients impliy an additional selection rule [85]: $\langle J_i M_i \, L m_\gamma \mid J_f M_f \rangle$ vanishes if $|m_\gamma| > L$ is not fullfilled. Thus, only multipoles with

$$L \geq |m_\gamma| \tag{4.40}$$

can contribute to the transition. Of course, also here the parity selection rule (4.38) must be fulfilled.

Although selection rule (4.39) is *modified* with regard to the plane-wave one (4.37), it has a similar physical interpretation: An atom placed on the beam axis can only be excited from the magnetic sublevel M_i to the final state $M_f = M_i + m_\gamma$, if the photon carries an TAM of m_γ, i.e. in the paraxial regime, an OAM of m_l and helicity λ.

If the atom is not centered on the beam axis ($\boldsymbol{b} \neq 0$), the situation becomes more complicated. The off-axis section rules were theoretically investigated in [90, 91]. It was shown there, that depending on the transition frequency ω, the opening angle θ_k, and the total angular momentum m_γ, the transition amplitude vanishes for particular impact parameters $\boldsymbol{b}$. However, it was found in [90] that after the averaging over the atomic position the transition amplitude approaches quickly the plane-wave behaviour for increasing distance from the beam center.

Chapter 5

Control of Multipoles

In the previous chapters, we developed the theoretical formalism to investigate the excitation of single atoms and ions by plane-wave or twisted Bessel photons. So far, we have not paid much attention to different multipoles. The multipole expansion of the radiation field was introduced in Sec. 2.3. In the following, we will apply the developed formalism to the scenario in which the excitation proceeds only via a few multipole channels. Special emphasis is put on the case, where only two channels are allowed by the selection rules. We start with the derivation of transition rates for individual multipole channels, as this will enable us to further analyze the modification of multipole transitions by twisted light with the help of the *geometrical* factor. The results of this chapter are published in our paper [92].

5.1 High Order Multipole Excitations

5.1.1 Partial Transition Rates

In Sec. 4.4 we derived the total transitions rates for excitations with plane waves (4.28) and twisted light (4.33). Since we want to investigate the modification of multipole transitions by twisted light, further analysis of these expressions is needed. The total transition rates arise from the squared matrix elements, which contain summations over p and L, i.e. all multipole channels that are allowed by the selection rules, see Eqs. (4.26) and (4.32). Now, the question arises: How does the total rate depend on the individual contributions of the partial multipole terms? To assay this, we start with the derivation of the total rate in terms of partial multipole transition rates for plane waves first. Therefore, we insert $\mathcal{M}_{fi}^{(\mathrm{pl})}$ (4.26) into Eq. (4.28) and find

the following equation

$$W_{fi}^{(\mathrm{pl})} = \frac{2\pi}{[J_i, J_f]\,\alpha^2} \sum_{M_i M_f} \left(\sum_{L_1 M_1 p_1} i^{L_1} [L_1]^{1/2} (i\lambda)^{p_1} \left\langle J_i M_i\, L_1 M_1 \mid J_f M_f \right\rangle \right. \tag{5.1}$$
$$\left. \times\, D^{L_1}_{M_1 \lambda}(\varphi_k, \theta_k, 0) \left\langle \alpha_f J_f \,||H_\gamma(pL)||\, \alpha_i J_i \right\rangle \right)$$
$$\times \left(\sum_{L_2 M_2 p_2} (-i)^{L_2} [L_2]^{1/2} (-i\lambda)^{p_2} \left\langle J_i M_i\, L_2 M_2 \mid J_f M_f \right\rangle \right.$$
$$\left. \times\, D^{L_2 *}_{M_2 \lambda}(\varphi_k, \theta_k, 0) \left\langle \alpha_f J_f \,||H_\gamma(p_2 L_2)||\, \alpha_i J_i \right\rangle^* \right).$$

Here we show the expanded form of this expression to point out all general dependencies. At first glance, one would suspect that in addition to partial multipole rates, also interference terms contributes to the total rate. However, this is not the case, because all mixed terms vanish, or, more accurately $\mathcal{M}(p_1 L_1)\left(\mathcal{M}(p_2 L_2)\right)^* = -\left(\mathcal{M}(p_1 L_1)\right)^* \mathcal{M}(p_2 L_2)$. All interference terms cancel. Then, after some algebra, we find for the total rate

$$W_{fi}^{(\mathrm{pl})} \;=\; \sum_{pL} W_{fi}^{(\mathrm{pl})}(pL), \tag{5.2}$$

where the partial multipole rates are

$$W_{fi}^{(\mathrm{pl})}(pL) \;=\; \frac{2\pi}{[J_i]\alpha^2} \left| \left\langle \alpha_f J_f \,||H_\gamma(pL)||\, \alpha_i J_i \right\rangle \right|^2 . \tag{5.3}$$

At this point, an annotation is necessary. In this chapter, only rates are considered at which we sum over all projections M_i and M_f. Consequently, the orientation of the atomic quantization axis does not play a role here. The situation is different, as we shall see in the next chapter when we analyze transitions between magnetic sublevels.

Let us continue now, with the calculation of the total transition rate for Bessel beams. We have to perform the same steps as in the plane-wave case and find

$$W_{fi}^{(\mathrm{tw})} \;=\; \frac{2\pi}{[J_i]\alpha^2} \sum_{M_i M_f} \left| \mathcal{M}_{fi}^{(\mathrm{tw})} \right|^2 = \sum_{pL} W_{fi}^{(\mathrm{tw})}(pL)$$
$$= \sum_{pL} \sum_{M} \left| d^L_{M\lambda}(\theta_k)\, J_{m_\gamma - M}(\varkappa b) \right|^2 W_{fi}^{(\mathrm{pl})}(pL)\,, \tag{5.4}$$

and, therefore, the partial transition rates for twisted photons have the following form

$$W_{fi}^{(\mathrm{tw})}(pL) = \sum_{M} \left| d^L_{M\lambda}(\theta_k)\, J_{m_\gamma - M}(\varkappa b) \right|^2 W_{fi}^{(\mathrm{pl})}(pL)\,. \tag{5.5}$$

As seen from the two formulas above (Eq. (4.28) and (5.4)), the total photoexcitation rates $W_{fi}^{(\mathrm{pl})}$ and $W_{fi}^{(\mathrm{tw})}$ are given as the *sum* of rates of individual electric and magnetic multipole transitions without any interference terms.

The summations $\sum_{Lp}$ in Eqs. (5.2) and (5.4) are restricted to the (pL)-terms that are allowed by the selection rules for a given choice of initial and final atomic states. Moreover, each partial rate $W_{fi}^{(\mathrm{tw})}(pL)$ is a product of its plane-wave counterpart (5.3) and a geometrical term $\left|d^L_{M\lambda}(\theta_k)\, J_{m_\gamma - M}(\varkappa b)\right|^2$, which describes the properties of the Bessel beam and the position of the target atom. This, therefore, implies that the relative contributions of the multipole channels (pL) to the total rate of the $|\alpha_i J_i\rangle + \gamma \to |\alpha_f J_f\rangle$ transition can be modified by the use of twisted light. This aspect will be the main focus of the next section.

5.2 Geometrical Factor

In this section, we want to quantify the relative contribution of the multipole components to the total transition rate. As already mentioned above, due to the geometrical term $\left|d^L_{M\lambda}(\theta_k)\, J_{m_\gamma - M}(\varkappa b)\right|^2$, the relative strength of allowed multipole components can be modified by the use of twisted light. The number of contributing multipoles, i.e. the sum over (pL) in Eqs. (5.4), is restricted by the parity and angular momentum selection rules. For this reason, an atomic transition $|\alpha_i J_i\rangle + \gamma \to |\alpha_f J_f\rangle$ may rather often proceed via only two channels and then its rate is given by

$$W_{fi}^{(\mathrm{tw})} = W_{fi}^{(\mathrm{tw})}(p_1 L_1) + W_{fi}^{(\mathrm{tw})}(p_2 L_2)\,. \tag{5.6}$$

In the previous section, we have seen that in the plane-wave case the relative contribution of these channels is mainly defined by the reduced matrix element $\langle \alpha_f J_f \,||H_\gamma(pL)||\, \alpha_i J_i\rangle$. The reduced matrix element does neither depend on the projections of the angular momenta, nor it depends on the orientation of the quantization axis (defined by the applied B-field) and the light propagation direction. It solely depends on the electronic structure of the target atom. Accordingly, the relative contribution of the multipole channels in the case of the plane wave is only determined by the electronic structure.
In contrast, twisted light has a helical phase- and annual transverse intensity structure. Consequently, its partial multipole rates $W_{fi}^{(\mathrm{tw})}(pL)$ depend additionally on the geometrical properties of the radiation and the position of the atom. Next, we want to analyze how the interaction with twisted light affects the relative strength of the multipoles. Therefore, we consider the probability ratio

$$\frac{W_{fi}^{(\mathrm{tw})}(p_1 L_1)}{W_{fi}^{(\mathrm{tw})}(p_2 L_2)} = \mathcal{R}_{L_1 L_2}(\varkappa b)\ \frac{W_{fi}^{(\mathrm{pl})}(p_1 L_1)}{W_{fi}^{(\mathrm{pl})}(p_2 L_2)}\,. \tag{5.7}$$

This ratio is written as a product of two terms, whereby we call the first term

$$\mathcal{R}_{L_1L_2}(\varkappa b) = \frac{\sum_M \left| d^{L_1}_{M\lambda}(\theta_k)\, J_{m_\gamma - M}(\varkappa b) \right|^2}{\sum_M \left| d^{L_2}_{M\lambda}(\theta_k)\, J_{m_\gamma - M}(\varkappa b) \right|^2} \tag{5.8}$$

geometrical factor because it depends on geometrical parameters: the TAM projection m_γ onto the quantitation ($z-$) axis, and the opening angle θ_k of the Bessel beam, as well as on the impact parameter b, which characterizes the position of the target atom with respect to the beam center. Now let us focus on the second term in Eq. (5.7). It is the squared ratio of the reduced matrix elements of multipole transitions

$$\frac{W^{(\mathrm{pl})}_{fi}(p_1L_1)}{W^{(\mathrm{pl})}_{fi}(p_2L_2)} = \frac{\left| \langle \alpha_f J_f \,||H_\gamma(p_1L_1)||\, \alpha_i J_i \rangle \right|^2}{\left| \langle \alpha_f J_f \,||H_\gamma(p_2L_2)||\, \alpha_i J_i \rangle \right|^2} \tag{5.9}$$

and is independent of the geometry of the process. The ratio (5.9) only reflects the electronic structure of the atom.

One can clearly see from Eq. (5.7) that the relative strength of multipole transitions can be modified compared to the usual plane-wave radiation, if the transition is induced by twisted light. The factor $\mathcal{R}_{L_1L_2}(\varkappa b)$ (5.8) determines this modification for an atom with well-defined impact parameter b.

5.2.1 Quadrupole-to-Dipole Factor

It was shown above that only the geometrical factor $\mathcal{R}_{L_1L_2}(\varkappa b)$ (5.8) relates the ratios of multipole transition probabilities for plane waves and twisted light to each other. How strongly the twisted light affects the relative contribution of multipole terms is determined by the magnitude of these factors. In the following, we will calculate $\mathcal{R}_{L_1L_2}(\varkappa b)$ for some pairs of multipoles, which are typical in atomic spectroscopy.

Our first example will cover the leading terms in the multipole expansion, hence, $L_1 = 2$, $L_2 = 1$. From Eq. (5.8) it can be seen that the geometric factors do not depend on the type p of the transition. As a consequence, the *quadrupole-to-dipole factor* $\mathcal{R}_{L_1=2,\,L_2=1}(\varkappa b)$ describes the enhancement (or reduction) of both probability ratios $M2/E1$ and $E2/M1$.

In Fig. 5.1 the geometrical factor $\mathcal{R}_{L_1=2,\,L_2=1}(\varkappa b)$ is shown for the $M2/E1$ and $E2/M1$ probability ratios. The calculations for this factor were performed as a function of the dimensionless parameter $kb = \alpha\, \omega\, b$ and for an incident Bessel beam with positive helicity $\lambda = 1$ and three different TAM projections, namely $m_\gamma = 1$ (left panel), $m_\gamma = 2$ (middle panel), and $m_\gamma = 3$ (right panel). The results are shown for the following three opening angles: $\theta_k = 1^\circ$ (black dotted line), $\theta_k = 10^\circ$ (blue dashed line) and $\theta_k = 30^\circ$ (red solid line). As it can be observed from this figure, the geometrical factor $\mathcal{R}_{L_1=2,\,L_2=1}(\varkappa b)$ is very sensitive to both parameters, that characterized the twisted light beam, the opening angle θ_k and the TAM projection

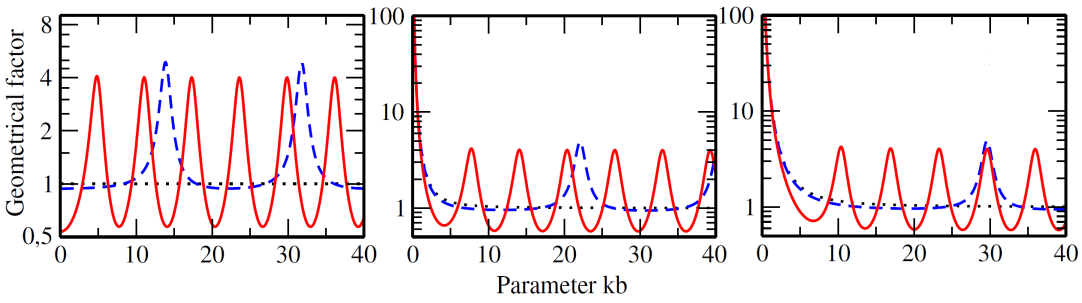

FIGURE 5.1: The geometrical factor $\mathcal{R}_{L_1=2,\,L_2=1}\,(\varkappa b)$ for the $M2/E1$ and $E2/M1$ probability ratios. Calculations have been performed for the incident Bessel light with helicity $\lambda = 1$, TAM projections $m_\gamma = 1$ (left panel), $m_\gamma = 2$ (middle panel) and $m_\gamma = 3$ (right panel) and with opening angles $\theta_k = 1^\circ$ (black dotted line), $\theta_k = 10^\circ$ (blue dashed line) and $\theta_k = 30^\circ$ (red solid line). The figures are taken from our publication, Ref. [92].

m_γ. Let us now focus on the left panel in this figure. It depicts a twisted Bessel with $m_\gamma = 1$. For a small opening angle $\theta_k = 1^\circ$ (black dashed line) the geometrical factor $\mathcal{R}_{L_1L_2}\,(\varkappa b)$ is approximately one. If the geometrical factor is one, this means, that there is no modification due to the twisted light properties in comparison to the plane-wave case. This behaviour is expected because it represents the plane-wave limit, where $\theta_k \to 0$ and $m_\gamma = \lambda$. Moreover, that is also reflected in the dependency on the opening angle. With increasing θ_k the geometrical factor clearly exceeds the value for the plane-wave prediction $\mathcal{R}^{(pl)} = 1$. Then mainly two modifications become visible. The first one concerns all three TAM projections: From some distance from the beam center $kb \gtrsim 5$, the factor $\mathcal{R}_{L_1=2,\,L_2=1}\,(\varkappa b)$ starts to oscillate with amplitudes of about 5. This implies that the quadrupole ($L = 2$) term strongly predominates the dipole ($L = 1$) counterpart for certain kb. The second modification does not apply to cases with a TAM projection of $m_\gamma = 1$: For TAM projections with $m_\gamma > 1$ and close to the vortex, i.e. $kb \to 0$, the interaction with Bessel light is most pronounced. This effect can be observed in the middle and right panel of Fig. 5.1. As can be seen from both figures and for all (non-zero) opening angles θ_k, the geometrical factor $\mathcal{R}_{L_1=2,\,L_2=1}\,(\varkappa b)$ is several orders of magnitudes larger than $\mathcal{R}^{(pl)} = 1$. This enhancement can be explained with the help of *selection rules* for a transition $|\alpha_i J_i M_i\rangle + \gamma \to |\alpha_f J_f M_f\rangle$ induced by twisted light.

In Sec. 4.5.2, we have discovered that these *modified selection rules*, depend in general strongly on the position of the target atom within the Bessel wavefront. However, we found that for the particular case of $b \to 0$, that is when the atom is located at the beam axis, the magnetic quantum numbers M_i and M_f of the initial and final state are related to the TAM projection m_γ of the Bessel beam by the following

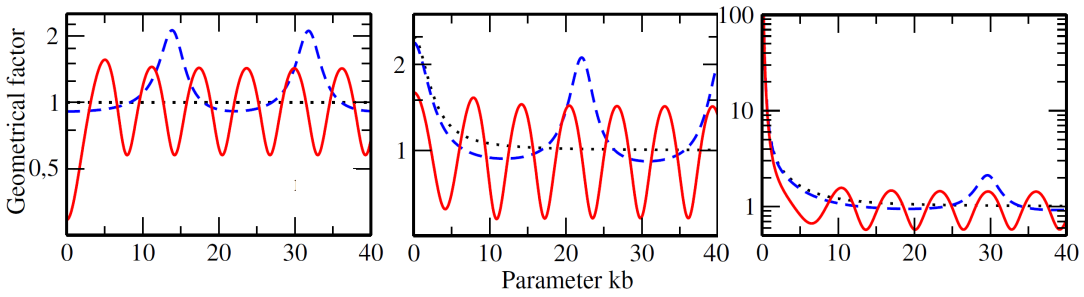

FIGURE 5.2: The same as Fig. 5.1 but for the geometrical factor $\mathcal{R}_{L_1=3,\,L_2=2}\,(\varkappa b)$ for the $E3/M2$ and $M3/E2$ probability ratios. The figures are taken from our publication, Ref. [92].

relation

$$M_f = m_\gamma + M_i\,. \tag{5.10}$$

Moreover, it was concluded from this expression and Eq. (4.32) that only multipoles with

$$L \geq |m_\gamma| \tag{5.11}$$

can contribute to an excitation. Consequently, for $m_\gamma = 2$ and small impact parameters, i.e. $b \approx 0$, so that (5.11) can be applied, dipole transitions are *forbidden* and therefore strongly suppressed. As a consequence $\mathcal{R}_{L_1=2,\,L_2=1}\,(\varkappa b)$ is greatly increased. For higher TAM projections, i.e. $m_\gamma > 2$, both $L = 1$ and $L = 2$ terms are forbidden for $b = 0$. However, the quadrupole transition rate rises faster than the dipole for an increasing impact parameter. Near the beam center ($kb \lesssim 1$), this results again in very large values of $\mathcal{R}_{L_1=2,\,L_2=1}\,(\varkappa b)$.

5.2.2 Octupole-to-Quadrupole Factor

So far, we have discussed only one geometrical factor, namely $\mathcal{R}_{L_1=2,\,L_2=1}\,(\varkappa b)$, which enables an investigation of the quadrupole-to-dipole transition probability ratios. However, there are of course others. Therefore, we now turn our attention to the pair of multipoles that comes next in the multipole expansion: $\mathcal{R}_{L_1=3,\,L_2=2}\,(\varkappa b)$. This factor describes the probability (or rate) ratios $E3/M2$ or $M3/E2$.

We display in Fig. 5.2 this geometrical factor $\mathcal{R}_{L_1=3,\,L_2=2}\,(\varkappa b)$, again, for an incident Bessel beam with helicity $\lambda = 1$, the three different TAM projections, $m_\gamma = 1$ (left panel), $m_\gamma = 2$ (middle panel), and $m_\gamma = 3$ (right panel), and the opening angles, $\theta_k = 1^\circ$ (black dotted line), $\theta_k = 10^\circ$ (blue dashed line) and $\theta_k = 30^\circ$ (red solid line). As in the quadrupole-to-dipole case discussed above, also $\mathcal{R}_{L_1=3,\,L_2=2}\,(\varkappa b)$ strongly dependents on the TAM projection m_γ and the opening angle θ_k. For an atom displaced from the beam center by $kb \gtrsim 5$, the values of θ_k have a strong influence on the ratio. For $\theta_k = 1^\circ$ the geometrical factor $\mathcal{R}_{L_1=3,\,L_2=2}\,(\varkappa b)$ reproduces

almost identically the plane-wave result $\mathcal{R}^{(pl)} = 1$, while it oscillates for large opening angles $\theta_k = 10^\circ$ and $\theta_k = 30^\circ$.

If we compare the amplitudes of these oscillations with those of the quadrupole–to–dipole case, we find that they are only half the size. Nevertheless, the results indicate that the $E3/M2$ and $M3/E2$ rate ratios can be increased and decreased, respectively, by almost a factor of two if one chooses a proper distance of the target atom from the light axis.

Again, as before in the $M2/E1$ (or $E2/M1$) case (see Fig. 5.1), the largest enhancement of the factor $\mathcal{R}_{L_1=3,\,L_2=2}\,(\varkappa b)$ can be found near the beam center, if $kb \to 0$. But, in contrast to $\mathcal{R}_{L_1=2,\,L_2=1}\,(\varkappa b)$, the octupole-to-quadrupole factor only grows tremendously for TAM projections $m_\gamma > 2$. This can also be explained here with the transition selection rules. They allow both the quadrupole ($L = 2$) and the octupole ($L = 3$) excitations of an atom, which is located at the center of the Bessel beam ($b = 0$) with $m_\gamma \leq 2$. For the higher topological charge $m_\gamma = 3$ the dipole terms are forbidden at $b = 0$. Therefore, the $M2$ (or $E2$) transition is suppressed near the beam center. Consequently, that leads to a strong increase of the factor $\mathcal{R}_{L_1=3,\,L_2=2}\,(\varkappa b)$, which can be clearly seen in the right panel of Fig. 5.2.

5.2.3 Averaged Geometrical Factor

Until now, we have considered only the geometrical factor for a well-localized target atom. In Sec. 4.4.3 we have already mentioned, that this is an idealized theoretical scenario and it can not be realized like that in the present experiments. Experimentally, the impact parameter b can only be determined with a relatively high degree of uncertainty σ. By making use of Eq. (4.34), the expression for the photoexcitation rate for the realistic scenario of a delocalized atom, and Eq. (5.4) we can express the rate in terms of partial rates $W_{fi}^{(\mathrm{pl})}(pL)$

$$W_{fi}^{(\mathrm{tw})}(\boldsymbol{b}_0, \sigma) = \sum_{pL} \sum_{M} \left| d^L_{M\lambda}(\theta_k) \right|^2 \, \mathcal{J}_{m_\gamma - M}(b_0)\, W_{fi}^{(\mathrm{pl})}(pL)\,. \tag{5.12}$$

The function $\mathcal{J}_{m_\gamma - M}(b_0)$ is given as

$$\begin{aligned} \mathcal{J}_{m_\gamma - M}(b_0) \;&=\; \int f(\boldsymbol{b}; \boldsymbol{b}_0)\, \left| J_{m_\gamma - M}(\varkappa b) \right|^2 \mathrm{d}\boldsymbol{b} \\ &= \frac{1}{\sigma^2} \int_0^\infty \mathrm{d}b\, b\, I_0\left(\frac{b b_0}{\sigma^2} \right) \left| J_{m_\gamma - M}(\varkappa b) \right|^2 \mathrm{e}^{-\frac{b^2 + b_0^2}{2\sigma^2}}\,, \end{aligned} \tag{5.13}$$

where I_0 is the modified Bessel function of the first kind [58]. Similarly as before, the partial multipole rates in Eq. (5.12) can be written as a product of their plan-wave counterparts $W_{fi}^{(\mathrm{pl})}(pL)$ and a term, which depends on the properties of twisted

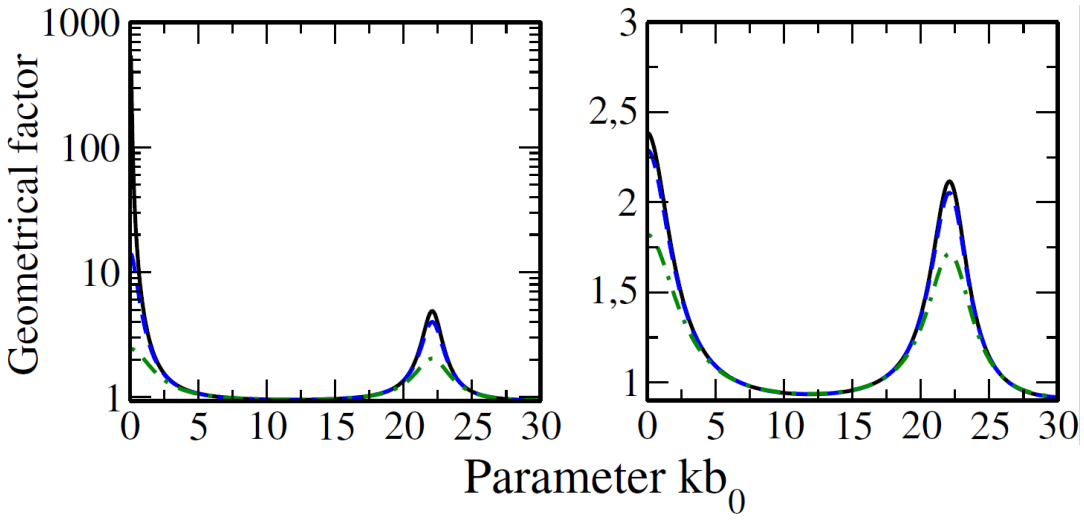

FIGURE 5.3: The averaged geometrical factors $\widetilde{\mathcal{R}}_{L_1=2,\,L_2=1}\,(\varkappa b_0)$ (left panel) and $\widetilde{\mathcal{R}}_{L_1=3,\,L_2=2}\,(\varkappa b_0)$ (right panel). Calculations have been performed for the incident Bessel light with helicity $\lambda = 1$, TAM projection $m_\gamma = 2$ and opening angle $\theta_k = 10^\circ$. The position of a target atom is described by the Gaussian distribution (4.34) with the width $\sigma = 1/\,(15k)$ (blue dashed line) and $\sigma = 1/\,(5k)$ (green dash–dotted line). These results are compared, moreover, with the prediction obtained for a well–localized atom (black solid line). The figures are taken from our publication, Ref. [92].

beam and geometry of atomic target. With these expressions, we are ready to consider the *averaged* geometrical factor

$$\widetilde{\mathcal{R}}_{L_1L_2}\,(\varkappa b_0) = \frac{\sum\limits_M \left|d^{L_1}_{M\lambda}(\theta_k)\right|^2 \mathcal{J}_{m_\gamma - M}(b_0)}{\sum\limits_M \left|d^{L_2}_{M\lambda}(\theta_k)\right|^2 \mathcal{J}_{m_\gamma - M}(b_0)} \tag{5.14}$$

for the realistic scenario of delocalized atom, where $\mathcal{J}_{m_\gamma - M}(b_0)$ is given by Eq. (5.13). Since the probability ratio (5.7) is a product of two terms, where only the one, the geometrical factor, depends on the position of the target atom, $\mathcal{R}_{L_1L_2}\,(\varkappa b)$ can simply be replaced by $\widetilde{\mathcal{R}}_{L_1L_2}\,(\varkappa b_0)$. That means this averaged factor allows one to analyze the relative strength of the multipoles in atomic trap experiments.

In Figs. 5.1 and 5.2 we displayed the quadrupole-to-dipole $\mathcal{R}_{L_1=2,\,L_2=1}\,(\varkappa b)$ and octupole-to-quadrupole factors $\mathcal{R}_{L_1=3,\,L_2=2}\,(\varkappa b)$ for a well-defined positioned target atom.

Now we want to investigate, how the uncertainty of the atomic position affects the relative strength of multipole transitions. Therefore, we compare in Fig. 5.3 the geometrical factors for a well-localized (black solid line) and delocalized atom.

We considered two cases for the the latter case: a width of the position distribution $\sigma = 1/(15k)$ (blue dashed line) and $\sigma = 1/(5k)$ (green dashed–dotted line). Also in these figures, we depict both the quadrupole–to-dipole and the octupole–to–quadrupole factor as functions of the dimensionless parameter $kb_0 = \alpha\omega b_0$, with $b_0 = b$ for the case of a well-localized atom.

In Fig. 5.3, in contrast to Figs. 5.1 and 5.2, we have limited our calculations to a single TAM projection and a single opening angle, namely $m_\gamma = 2$ and $\theta_k = 10^\circ$. The left panel shows the averaged quadrupole-to-dipole $\widetilde{\mathcal{R}}_{L_1=2,L_2=1}(\varkappa b_0)$ and the right panel the octupole-to-quadrupole factors $\widetilde{\mathcal{R}}_{L_1=3,L_2=2}(\varkappa b_0)$. It is noticeable in both figures, that the peaks become smaller with increasing σ, indicating the delocalization of the target atom causes the geometrical factor $\widetilde{\mathcal{R}}_{L_1L_2}(\varkappa b_0)$ to approach the plane–wave result $\mathcal{R}^{(pl)} = 1$. Again, as before in the case of $\mathcal{R}_{L_1L_2}(\varkappa b_0)$, the most pronounced effect can be determined, for the quadrupole-to-dipole factor and small impact parameters, $b \to 0$, cf. right panel in Fig. 5.3. However, in this case, $\widetilde{\mathcal{R}}_{L_1=2,L_2=1}(\varkappa b_0)$ is reduced by at least one order of magnitude if the atomic position is not well-defined within the transverse plane of the twisted beam. Moreover, these results indicate a decrease at $kb_0 \approx 22$ of the geometrical factor $\widetilde{\mathcal{R}}_{L_1=2,L_2=1}(\varkappa b_0)$ by almost a factor of three with the increase in the location uncertainty σ.

These findings clearly show that the requirement for precise localization of the target atom is essential to be able to observe an efficient modification of the relative strength of multipole atomic transitions by a twisted light.

5.2.4 Example: $^3P_1 \to {}^1P_1$ Transition in Neutral Mg

In the sections before, we discussed the geometrical factors $\mathcal{R}_{L_1L_2}(\varkappa)$ and $\widetilde{\mathcal{R}}_{L_1L_2}(\varkappa b_0)$. They make it possible to analyze how much the relative strength of multipole components can be modified by the use of twisted light. Even though this method can be applied to any *arbitrary* atom and *arbitrary* transition, electric-dipole forbidden excitations are of particular interest. The reason for this is that for transitions, which involve an electric dipole term, the plane-wave $pL/E1$ probability ratios are usually very small. Consequently, it will be difficult to notice modifications in the relative contributions of pL and $E1$ multipole components for interactions of twisted light with a delocalized atom. On the contrary, in atomic spectroscopy, several transitions proceed via various higher-order multipole channels, i.e. *non*–E1 channels, which have almost the same (plane-wave) transition strength. For this reason, the effect of photoabsorption of twisted photons is strong in such cases and can be observed experimentally.

Here we consider as an example the $3s3p\,^3P_1 \to 3s3p\,^1P_1$ transition in neutral Mg, see Fig. 5.4, which is electric-dipole forbidden due to the parity selection rule (4.38) (both states have odd parity). This triplet-to-singlet transition has a wavelength of 758 nm and well separated from much stronger E1 transitions [93], and can be induced by red diode lasers. The atom can be excited either via the magnetic dipole M1 or via the electric quadrupole E2 transition.

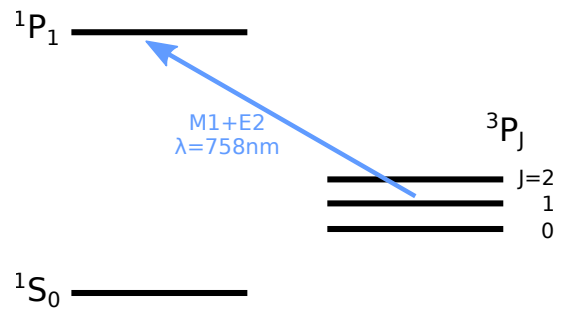

FIGURE 5.4: The $3s3p\,^3P_1 \rightarrow 3s3p\,^1P_1$ transition in Mg atom has a wavelength of 758 nm and may proceed via either the magnetic dipole M1 or via the electric quadrupole E2 channel

To proceed further, we need to estimate the probabilities of these multipole transitions. Therefore, the multiconfiguration Dirac-Fock (MCDF) approach was used, which makes it possible to take into account the relativistic and magnetic interaction effects in many-electron systems. These detailed MCDF calculations were performed by Prof. Fritzsche with the help of the JAC code [94] and yielded the following values for the oscillator strengths: $f_{M1} = 3.5 \times 10^{-12}$ and $f_{E2} = 4.8 \times 10^{-12}$ for the M1 and E2 transitions, respectively.
The oscillator strength is proportional to the square modulus of the transition matrix element [55]. Hence, we can use these values and if the $^3P_1 \rightarrow {}^1P_1$ transition is induced by plane-wave radiation, we insert this into Eq. (5.9). We find that the rates of both channels will be nearly the same, namely $W_{fi}^{(\mathrm{pl})}(E2)/W_{fi}^{(\mathrm{pl})}(M1) \approx 1.37$. But, as already discussed above, one can modify this ratio by using twisted light: For example, we have shown that the contribution of the quadrupole transition can be significantly enhanced, if the Mg atom is placed near the beam center ($kb < 5$) with TAM projection $|m_\gamma| > 1$, see Fig. 5.1. But this enhancement depends greatly on how well the target atom can be positioned. As seen from Fig. 5.3, already an uncertainty of $\sigma = 1/(5k)$, causes an increase of many orders of magnitude in the averaged geometrical factor $\widetilde{\mathcal{R}}_{L_1=2,L_2=1}\,(\varkappa b_0 = 0)$ and, as a consequence, also of the ratio $W_{fi}^{(\mathrm{tw})}(E2)/W_{fi}^{(\mathrm{tw})}(M1)$. This corresponds, for the $^3P_1 \rightarrow {}^1P_1$ transition in Mg with energy $\hbar\omega = 1.84$ eV, to an uncertainty of $\sigma = 21$ nm, which agrees well with the position uncertainty achieved in present experiments [95].

For this transition, we calculated the partial rates. These results are shown in Fig. 5.5, where the calculations for the magnetic dipole (green dashed–dotted line) and electric quadrupole (blue dashed line) transition rates were performed for the uncertainty σ =21 nm from Eq. (5.12), and displayed as functions of the impact parameter b_0. For better comparison, these rates, as well as their sum (black solid line), are normalized in relation to the total plane-wave counterpart $W_{fi}^{(\mathrm{pl})}$ and are calculated for an incident Bessel beam with an opening angle of $\theta_k = 10^\circ$ and a TAM projection of $m_\gamma = 2$. From this figure it can be easily obtained, the rate of the magnetic dipole $W_{fi}^{(\mathrm{tw})}(M1)$ is strongly suppressed near the beam center ($b \approx 0$).

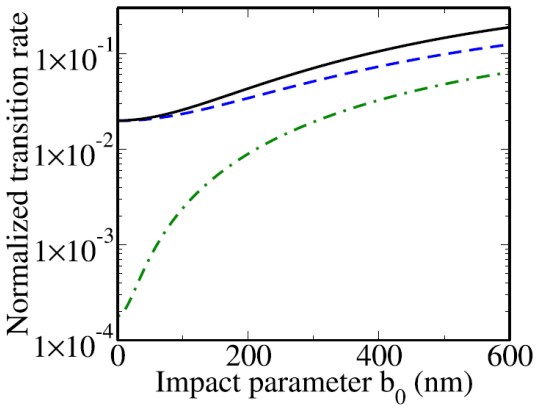

FIGURE 5.5: The normalized rates of the magnetic dipole (green dash–dotted line), electric quadrupole (blue dashed line) and the sum of both (black solid line) components of the $3s3p\,^3P_1 \rightarrow 3s3p\,^1P_1$ photo–excitation of neutral Mg atom. Calculations have been performed for the incident Bessel light with helicity $\lambda = 1$, TAM projection $m_\gamma = 2$ and opening angle $\theta_k = 10^\circ$. The rates are normalized by $W_{tot}^{(pl)}$. The target Mg atom is placed at the beam axis with the uncertainty σ = 20 nm. The figure is taken from our publication, Ref. [92].

This can be understood from the modified selection rule from which we know that transitions (for a well-located atom at $b_0 = 0$) with $|m_\gamma| > L$ are not allowed. Therefore, especially for $b_0 = 0$, the $^3P_1 \rightarrow {}^1P_1$ transition proceeds predominantly via the $E2$ channel. Moreover, as seen in Fig. 5.5, the transition rates are lower for excitations induced by Bessel light compared to those which were caused by plane waves. Again, this effect is most pronounced near the beam center and well expected, since for the rather small spread, $\sigma = 21$ nm, of the impact parameter, the target atom experiences only low light intensity, if the impact parameter b_0 is small. Of course, by increasing the uncertainty σ of the impact parameter, the twisted excitation rate can be significantly enhanced and can become comparable to the plane-wave one $W_{fi}^{(\mathrm{pl})}$, if $\sigma \rightarrow \infty$. Hence, a modification of the multipole transitions by twisted light will not be possible since $\widetilde{\mathcal{R}}_{L_1=2,L_2=1}\left(\varkappa b_0\right) \approx 1$, see Fig. 5.3 and Eq. (5.14). That means, it is necessary to achieve a precise position control of the trapped atom to observe the twisted light effect.

Chapter 6

Transition between Magnetic Hyperfine Levels

In this chapter, we study excitations of electric-dipole forbidden transitions between two hyperfine sublevels in a single trapped ion. In the previous chapter, we have already analyzed the transition matrix elements for the photoabsorption process. However, here we study the generalized excitation process when the light propagation direction does not coincide with the applied magnetic field, which defines the atomic quantization axis. When considering the excitation induced by twisted light, the position of the target atom within the transverse plane of the Bessel beam is important due to the local beam properties. First, the atom is assumed to be well-localized on the beam axis, and afterwards, we turn over to the more realistic scenario of a delocalized target atom. As an example we calculate the excitation rates for the ${}^2S_{1/2}(F_i = 0, M_i = 0) \to {}^2F_{7/2}(F_f = 3, M_f = 0)$ electric octupole (E3) hyperfine transition in the ${}^{171}\mathrm{Yb}^+$ ion, when the transition is driven by linearly, radially, and azimuthally polarized Bessel beams. The chapter concludes with a discussion of the AC-Stark shift. This frequency shift originates from the interaction of the external electric fields with the induced dipole moment of the atom. After a brief introduction to the theory of the AC-Stark effect, we continue with calculations taking into account both excitations from plane waves and twisted light. But before we start with the calculations, we shall explain the motivation to use twisted light in precision experiments. Parts of this chapter are based on Ref. [70].

6.1 Motivation (Experiments)

OAM-carrying light beams have some interesting and unique properties that differ from plane waves. In this section, we will mention some of them and explain why they are valuable for experimentalists. In Chapter 2 we analyzed the transverse intensity profile of twisted Bessel beams. There, we have already highlighted one of its characteristic features: The intensity minimum in the beam center. This property makes twisted light interesting for experiments. Photoexcitations of atoms (or ions) are surprisingly possible in this *dark* region, if the transition is induced by a vortex light beam. The reasons for this are excitations driven by higher multipole orders.

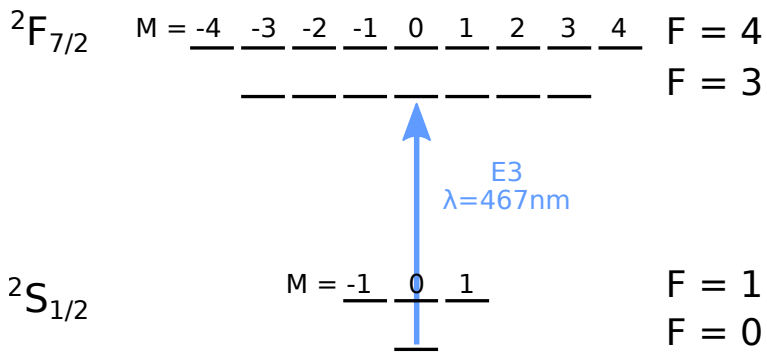

FIGURE 6.1: We consider the $^2S_{1/2}(F_i = 0) \rightarrow {}^2F_{7/2}(F_f = 3)$ transition in the $^{171}Yb^+$ ion. This is a E3 transition and has a wavelength of 467 nm. An applied magnetic field splits the hyperfine multiplets due to the Zeeman effect: For the lower with $F_i = 0$ there is only one sublevel and the upper hyperfine level $F_f = 3$ splits into 7 sublevels. In the experiment the $M_i = 0 \rightarrow M_f = 0$ transition is driven because it is insensitive to small magnetic perturbations.

While electric-dipole transitions are driven by the electric field, quadrupole transitions are caused by the field gradient and octupole ones are induced by the second derivative of the field [96].

Moreover, we have seen, that the helical phase factor $e^{im_l\varphi}$ modified the transition matrix element and therefore leads to selection rules, which differ from the plane-wave selection rules (see Sec. 4.5.2). That makes transitions possible, which are normally not allowed. We will analyze this in more detail in the remaining chapter.

These properties offer applications in many different areas, e.g. in quantum information theory [24], quantum cryptography [97], solid state systems [73] , but we will restrict ourselves to possible applications of twisted light in single-ion clocks.

Optical clocks are defined by the output of a certain optical frequency standard. Therefore, next we will briefly discuss the basics of (optical) frequency standards. In doing so, we will pay special attention to the E3 transition in the $^{171}Yb^+$ ion, which is used as a clock transition in the Yb single-ion clock [38, 39, 98].

6.1.1 Optical Frequency Standard with a Single $^{171}Yb^+$ Ion

Frequency standards are systems that generate periodic events. There are a variety of different oscillating devices, but to make them frequency standards, two essential requirements must be fulfilled: First, the device must produce a frequency that is stable in time. The frequency standard is "good" if it produces a stable frequency with only small variations. And secondly, the frequency has to be well-known, i.e., it must have been determined by comparison with a frequency, which can be traced back to a primary frequency standard [99]. Moreover, a frequency standard can

be used as a clock. The frequency standard becomes a clock by adding a counting mechanism for the events [100].

One of the most stable frequencies is the transition frequency in atoms. Due to this stability atomic standards are -so far- the *best* frequency standards. Therefore, they are used to define time. The definition of the second is based on the transition in a caesium-133 atom [101]

> *The second, symbol s, is the SI unit of time. It is defined by taking the fixed numerical value of the caesium frequency $\Delta\nu_{Cs}$, the unperturbed ground-state hyperfine transition frequency of the caesium-133 atom, to be 9 192 631 770 when expressed in the unit Hz, which is equal to s^{-1}.*

However, the invention of the frequency comb by Theodor W. Hänsch in 1998, made it possible to measure frequencies in the optical regime. *Optical* atomic clocks are realized with a transition in the optical frequency regime and because of the higher frequencies, they are more stable and accurate than microwave clocks [99]. They are based on the radiation that corresponds to the optical transition between two states in a single unperturbed atom. The frequency standards are characterized by their accuracy and (in)stabilities. In this work, we will restrict ourselves to transitions in a single-ion clock.

Having presented the main ideas of frequency standards, we may continue now with the discussion of one particular example: the $^{171}Yb^{+}$ single-ion clock. The ^{171}Yb isotope has a nuclear spin of $\frac{1}{2}$ and offers two optical reference transitions: the electric-quadrupole transition (E2) $^2S_{1/2}(F_i = 0) \rightarrow {}^2D_{3/2}(F_f = 2)$, and the electric-octupole (E3) $^2S_{1/2}(F_i = 0) \rightarrow {}^2F_{7/2}(F_f = 3)$. Both transitions are driven between two zero-valued magnetic hyperfine sublevels $M_i = 0 \rightarrow M_f = 0$, which has the advantage that the clock transitions are insensitive to small magnetic fields [39].

Optical clocks are based on electric-dipole (E1) forbidden transitions. Excitations that decay via a forbidden transition have a longer lifetime compared to those which decay through E1 transitions. Due to this long lifetime, a narrow resonance linewidth can be observed during the laser exaction [38]. A narrow resonance line is an important prerequisite for a precise optical clock. However, since such transitions are strongly prohibited, a high laser intensity is required for the excitation, which perturbs the electrical structure of the atom (or ion) and results, therefore, in a shift of the resonance frequency. Various effects disturb the excitation and enter the error budget of an atomic clock [102]. Here we will confine our attention to the AC-Stark shift in the $^{171}Yb^{+}$ single-ion clock, where the clock transition is based on an E3 hyperfine transition with an extremely narrow linewidth in the order of 10^{-9} Hz [38].

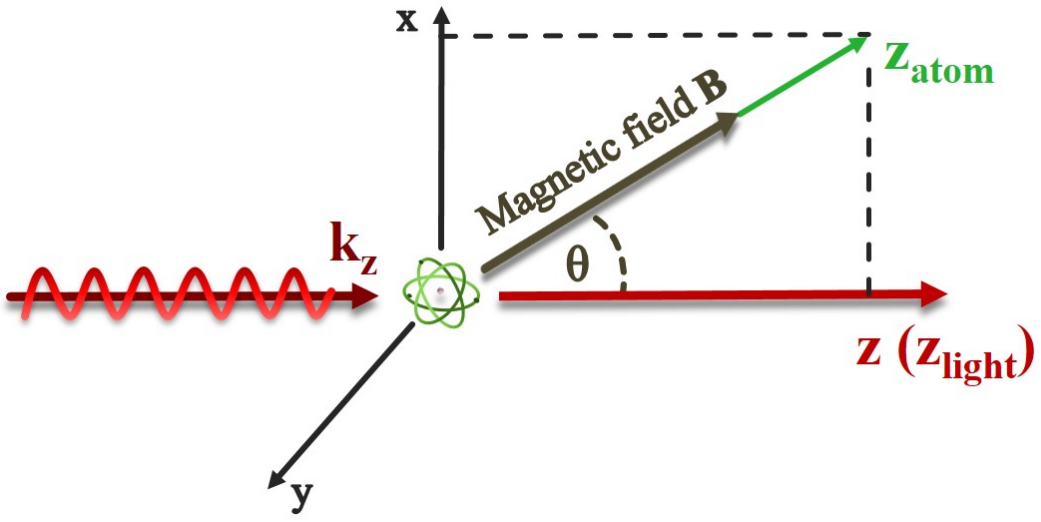

FIGURE 6.2: (Generalized) Geometry for the excitation of a single trapped atom in an external magnetic field by twisted light. In the general case, the light propagation direction (dark red) does not coincide with the atomic quantization axis z_{atom} (green). The Bessel beam propagates along the z_{light} (or z) axis with a well-defined longitudinal momentum $\boldsymbol{k_z}$. The applied magnetic ($\boldsymbol{B}$-)field defines the quantization axis z_{atom} of the atom. θ is the *magnetic field angle* and determines the direction of $\boldsymbol{B}$-field with respect to the propagation direction of the light beam.

6.2 Geometrical Setup

In this section, we are going to analyze the hyperfine transition of a single trapped ion, which is exposed to an external magnetic field $\boldsymbol{B}$. But before we can study the photoabsorption process, we need to explain the geometrical setup. In this particular case, that means, not only the position of the target atom has to be specified, but also the orientation of the additional magnetic field. The first point, the description of the atomic position, we already set with the introduction of the impact parameter $\boldsymbol{b}$, see Fig. 4.1, or the averaged atomic position with the Gaussian distribution (Fig. 4.2). While the static $\boldsymbol{B}$-field of the trap determines the quantization axis of an atom z_{atom}, the light propagation direction is chosen as the light quantization axis z_{light}. Until now, we have assumed that the quantization axis z_{atom} of an atom is in parallel with the quantization axis of the light. In the general case, when the propagation direction and the B-field do not coincide, the two quantization axes do not match. Such a general scenario is illustrated in Fig 6.2. However, for the further evaluation we have to rotate the states. Otherwise, they could not be related to each other. For example, the projections of the total angular momentum, M_i and M_f, as used in Eq. (4.23) or Eq. (4.29), are defined with respect to this atomic axis z_{atom}, while

the angular momentum m_l of light is projected on z_{light}. Therefore, to evaluate the matrix element for the general case, one has either to rotate the atomic states to the light axis z_{light}, or, vice versa, the photon multipoles to the atomic quantization axis z_{atom}. Both transformations are mathematically equivalent, but in this work, we perform the rotation of the atomic states

$$|\alpha_k F_k M_k\rangle_{\text{atom}} = \sum_{M_k'} d^{F_k}_{M_k M_k'}(\theta) \, |\alpha_k F_k M_k'\rangle_{\text{light}} \,, \tag{6.1}$$

where the index k is either i or f to denote quantum numbers of the initial or final state. $|\alpha_k F_k M_k\rangle_{\text{atom}}$ and $|\alpha_k F_i M_k'\rangle_{\text{light}}$ are states with the projections M_k and M_k' of the total angular momentum F onto the axes z_{atom} and $z(z_{\text{light}})$, respectively. In this expression, moreover, $d^{F_k}_{M_k M_k'}(\theta)$ is the (small) Wigner-D function and θ is the angle between the light propagation direction (along z_{light}) and the atomic quantization axis z_{atom}, see Fig. 6.2.

6.3 Matrix Elements and Excitation Rates of Hyperfine Transitions

6.3.1 Hyperfine Transitions Induced by Plane Waves

In the previous chapters, we performed calculations for fine structure transition. However, we now want to account for transitions between hyperfine structure levels. We assume, that the nucleus of the atom has non-zero spin $\boldsymbol{I}$. As a consequence, now the atomic states are characterized by their total angular momentum $\boldsymbol{F} = \boldsymbol{I} + \boldsymbol{J}$, and the transition amplitude for hyperfine transitions has the following form

$$\mathcal{M}_{fi}^{(\text{pl; tw})} = \left\langle \alpha_f F_f M_f \left| \sum_q \boldsymbol{\alpha}_q \cdot \boldsymbol{\mathcal{A}}(\boldsymbol{r}_q) \right| \alpha_i F_i M_i \right\rangle \,, \tag{6.2}$$

where for $\boldsymbol{\mathcal{A}}$, either $\boldsymbol{\mathcal{A}}^{(\text{pl})}$ (2.10) or $\boldsymbol{\mathcal{A}}^{(\text{tw})}$ (2.30), has to be inserted depending on the used radiation. Since we focus now on transitions between hyperfine levels, the states are labeled by the corresponding quantum numbers: the total angular momenta $F_{i,f}$ of the atom and their projections $M_{i,f}$ on the quantization axis (z_{atom}).

Furthermore, we assume that the light interacts only with the electrons, not with the nucleus. In this case, we can decouple the nuclear and electronic degrees of freedom, and write the hyperfine wave-functions $|\alpha_i F_i M_i\rangle$ as linear combinations of the corresponding atomic $|\alpha_k J_k M_{J_k}\rangle$ and nuclear states $|I M_I\rangle$ as follows [55]

$$|\alpha_k F_k M_k'\rangle = \sum_{M_{J_k} M_I} \langle J_k M_{J_k} \, I M_I \mid F_k M_k'\rangle \, |\alpha_k J_k M_{J_k}\rangle \, |I M_I\rangle \,. \tag{6.3}$$

For further calculation, we need to perform the rotation of the atomic states (6.1). In order to evaluate the matrix element, we have to substitute these expressions (6.1) and (6.3) into Eq. (6.2), make again use of the multipole expansion (2.27), and

apply afterwards the Wigner-Eckard theorem (4.25). However, these calculations are rather lengthy. For this reason, we defer the details of this derivation to Appendix A. As shown there, the transition amplitude for a transition between hyperfine level induced by a circularly polarized plane wave propagating along the z-axis, reads then as

$$\mathcal{M}_{fi}^{(\mathrm{pl})} = \sum_{Lp} C_{\alpha_i J_i \alpha_f J_f}^{F_i F_f I}(pL)\ (i\lambda)^p\ d^L_{\lambda \Delta M}(\theta)\ \langle F_i M_i\, L\Delta M \mid F_f M_f \rangle, \tag{6.4}$$

where $\Delta M = M_f - M_i$ is the difference between the initial and final angular momentum projection onto the atomic quantization axis z_{atom}. The factor $C_{\alpha_i J_i \alpha_f J_f}^{F_i F_f I}(pL)$ contains all information about the dynamics of the excitation process and is defined by

$$\begin{aligned} C_{\alpha_i J_i \alpha_f J_f}^{F_i F_f I}(pL) &= \sqrt{2\pi}\, i^L [L, F_i]^{1/2}\, (-1)^{J_f + I + F_i + L} \\ &\quad \times \left\{ \begin{array}{ccc} F_f & F_i & L \\ J_i & J_f & I \end{array} \right\} \langle \alpha_f J_f \,\|H_\gamma(pL)\|\, \alpha_i J_i \rangle\,. \end{aligned} \tag{6.5}$$

We can further simplify Eq. (6.4), if we consider only the leading multipole term. In that case we get the following

$$\mathcal{M}_{fi}^{(\mathrm{pl})}(pL) = C_{\alpha_i J_i \alpha_f J_f}^{F_i F_f I}(pL)\ (i\lambda)^p\, d^L_{\lambda\, \Delta M}(\theta)\, \langle F_i M_i\, L\Delta M | F_f M_f \rangle\,. \tag{6.6}$$

The transition rate for the $|\alpha_i F_i M_i\rangle + \gamma_i \to |\alpha_f F_f M_f\rangle$ excitation of an atom by plane-wave light can be calculated with the help of the amplitude $\mathcal{M}_{fi}^{(\mathrm{pl})}$ [55]

$$W_{fi}^{(\mathrm{pl})} = \frac{2\pi}{\alpha^2} \left| \mathcal{M}_{fi}^{(\mathrm{pl})} \right|^2. \tag{6.7}$$

This equation is similar to that one we derived in Sec. 4.4.1. It is worth to stress at this point, that the matrix element $\mathcal{M}_{fi}^{(\mathrm{pl})}$ (6.4) in Eq. (6.7) consists of summations over pL. Due to the same symmetry reasons as in Sec. 5.1.1, the mixed terms $\mathcal{M}_{fi}^{(\mathrm{pl})}(p_1 L_1)(\mathcal{M}_{fi}^{(\mathrm{pl})}(p_2 L_2))^*$ also cancel each other out in this case. Consequently, the total transition rate (6.7) for the hyperfine transition can be expressed in terms of the partial multipole transition rates $W_{fi}^{(\mathrm{pl})}(pL)$. However, it is recognizable that, in comparison to Eqs. (5.2) and (5.3), the summations over M_i and M_f are missing because we are now examining the transitions between sublevels. And for that reason, also the refactor $[J_i]^{-1}$ is dropped.

6.3.2 Hyperfine Transitions Induced by Twisted Light

In the first part of this section, we obtained the matrix element (6.4) and the transition rate (6.9) for a transition between two magnetic hyperfine levels, which is indued by plane-wave radiation. Now, in this second part, we consider the case when this excitation is driven by vortex beams. Therefore, we have to insert the twisted vector

potential $\mathcal{A}^{(\mathrm{tw})}$ (2.30) in transition matrix element (6.2). The steps for the derivation of the matrix element for transitions between magnetic hyperfine levels induced by twisted light are analog to those we made above for excitations by plane waves. Because of that, we will not present them here. The detailed derivation can be found in Appendix A. There, the transition amplitude for a single multipole in paraxial approximation is obtained as

$$\begin{aligned}\mathcal{M}_{fi}^{(\mathrm{tw})}(pL) &= C^{F_i F_f I}_{\alpha_i J_i \alpha_f J_f}(pL)\ (i\lambda)^p\,(-1)^{m_l+\lambda}\left\langle F_i M_i\, L\Delta M \mid F_f M_f\right\rangle \\ &\quad\times \sum_M i^M\, e^{i(m_l+\lambda-M)\varphi_b} J_{m_l+\lambda-M}(\varkappa b)\, d^L_{M\,\lambda}(\theta_k)\, d^L_{M\,\Delta M}(\theta)\,. \qquad (6.8)\end{aligned}$$

The *total* transition rates look similar to those that were derived for fine-structure transitions (cf. Eq. (5.4))

$$W_{fi}^{(\mathrm{tw})} = \frac{2\pi}{\alpha^2}\left|\mathcal{M}_{fi}^{(\mathrm{tw})}\right|^2 \qquad (6.9)$$

and can again be written as a sum of the separate multipole transition rates $W_{fi}^{(\mathrm{tw})}(pL)$. The center of a vortex beam is the position at which the light field differs most from plane waves. And therefore, it is most interesting for experimental applications. If we assume that the atom is placed there on the beam axis ($\boldsymbol{b} = 0$), $J_{m_l+\lambda-M} = \delta(m_l+\lambda-M)$, the sum in (6.8) reduces to a single term with $m_l+\lambda = M$, and the transition amplitude simplifies to

$$\begin{aligned}\mathcal{M}_{fi}^{(\mathrm{tw})}(pL;\, b=0) &= C^{F_i F_f I}_{\alpha_i J_i \alpha_f J_f}(pL)\ (i\lambda)^p\,(-i)^{m_l+\lambda} \\ &\quad\times \left\langle F_i M_i\, L\Delta M \mid F_f M_f\right\rangle d^L_{m_l+\lambda,\,\lambda}(\theta_k)\, d^L_{m_l+\lambda,\,\Delta M}(\theta)\,. \qquad (6.10)\end{aligned}$$

From this expression, it is easy to see, that the transitions are affected by the beam parameters, namely the helicity λ, opening angle θ_k and the OAM m_l, and, in addition, by the magnetic field angle θ. Both dependencies are expressed through the two Wigner-D functions $d^L_{m_l+\lambda,\,\lambda}(\theta_k)$ and $d^L_{m_l+\lambda,\,\Delta M}(\theta)$. On the latter, we will focus in the next section.

6.4 Angular Distributions

In this section, we will analyze how the light field should be aligned with respect to the applied magnetic field in order to achieve the highest transition probability. This study will be done for excitations by both plane-wave and twisted light radiation. Particular emphasis is paid to the electric octupole (E3) transition ${}^2S_{1/2} \to {}^2F_{7/2}$ between the hyperfine levels $M_i = 0 \to M_f = 0$ in a single trapped $^{171}\mathrm{Yb}^+$ ion, driven by linearly, radially, or azimuthally polarized Bessel light. But before we study the twisted case, we will first look at the excitations by linearly polarized plane waves.

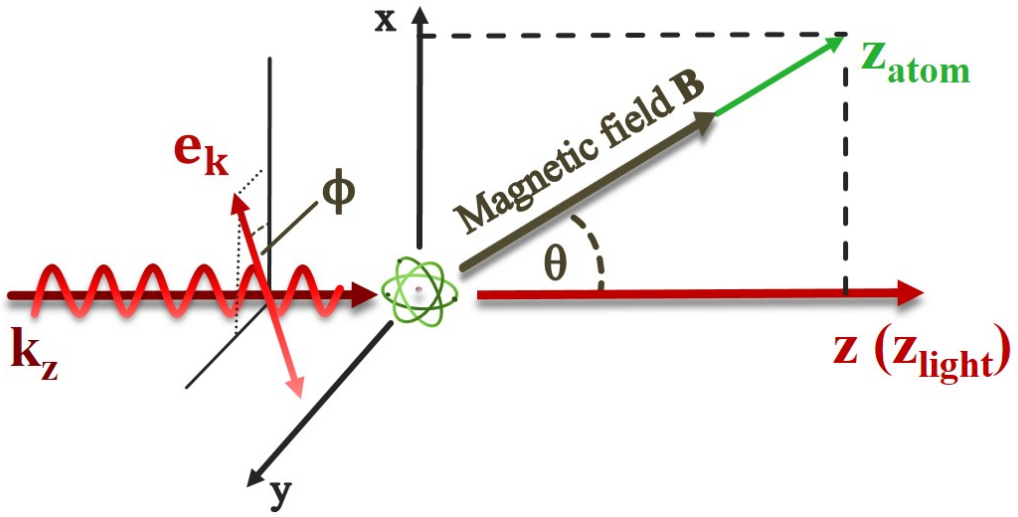

FIGURE 6.3: Same geometry as in Fig. (6.2), but here we consider also the orientation of the polarization vector $\boldsymbol{e_k}$. We assume that the light is linearly polarized and, again, propagating along $z(z_{\text{light}})$. The angle ϕ determines the orientation of the polarization vector $\boldsymbol{e_k}$ with regard to the plane spanned by the quantization axes of the atom z_{atom} and the light z_{light}.

There, in addition to the $\boldsymbol{B}$-field orientation, the alignment of the polarization vector will be taken into account.

6.4.1 Excitation by Linearly Polarized Plane Waves

The transition rates depend on the orientation of the applied magnetic field, which induces the splitting of the magnetic sublevels, see Eqs. (6.4) and (6.7). But this is not the only influence to consider, as proper alignment of the polarization vector can result in significant differences in the transition probabilities.
In what follows in this section, we derive angular distributions for hyperfine transitions between different Zeeman components $M_{i,f}$ induced by linearly polarized plane waves.

The partial transition rates $W_{\text{lin}}^{(\text{pl})}(pL)$ for linearly polarized plane waves (3.11) can be evaluated with the help of Eq. (6.6), so that

$$\begin{aligned} W_{\text{lin}}^{(\text{pl})}(pL) &= \left| C^{F_i F_f I}_{\alpha_i J_i \alpha_f J_f}(pL) \right|^2 \frac{2\pi}{\alpha^2} \langle F_i M_i \, L \Delta M | F_f M_f \rangle \\ &\quad \times \frac{1}{2} \left| \sum_{\lambda=\pm 1} (i\lambda)^p \, d^L_{\lambda \, \Delta M}(\theta) \, e^{-i\lambda\phi} \right|^2 , \end{aligned} \tag{6.11}$$

where, just to remind, angle ϕ determines the orientation of the polarization vector $\boldsymbol{e_k}$ with regard to the xz-plane, see Fig. 6.3. This equation describes the transition rate between two Zeeman sublevels, M_i and $M_f = M_i + \Delta M$, induced by a single

multipole term pL. As seen from this expression (6.11), the transition rate $W_{\mathrm{lin}}^{(\mathrm{pl})}(pL)$ can be parametrized as a product of two terms. The term in the first line of Eq. (6.11) depends on the electronic structure of an atom and the magnetic quantum numbers of its initial and final states. The term in the second line reflects the geometry of the process. Namely, it is sensitive to the magnetic field angle θ, as well as to the tilt ϕ of the polarization vector $\boldsymbol{e_k}$.

Next, we will focus on the second term in Eq. (6.11), and which, for the sake of shortness, we denote as

$$Q_{\Delta M}(pL) = \left| \sum_{\lambda=\pm 1} (i\lambda)^p \; d^L_{\lambda\,\Delta M}(\theta) \; e^{-i\lambda\phi} \right|^2 . \tag{6.12}$$

The angular distribution of the transition probability (6.11) 1 is determined solely by $Q_{\Delta M}(pL)$. And it can be seen from this expression, that $Q_{\Delta M}$ is insensitive on the electronic structure of a particular atom, but depends on the multipolarity L and the type p of transition.

Let us consider some typical examples: For instance, for the electric quadrupole $(E2;\ p = 1, L = 2)$ transition and for different $\Delta M's$ this factor reads as

$$Q_0(E2) = 6\cos^2\theta\cos^2\phi\sin^2\theta, \tag{6.13a}$$

$$Q_1(E2) = \cos^2\phi(\cos^2\theta - \sin^2\theta)^2 + \sin^2\phi\cos^2\theta, \tag{6.13b}$$

$$Q_2(E2) = \sin^2\theta(\cos^2\theta\cos^2\phi + \sin^2\phi). \tag{6.13c}$$

We can also derive $Q_{\Delta M}$ for the electric octupole $(E3;\ p = 1, L = 3)$ transition

$$Q_0(E3) = \frac{3}{4}(1 - 5\cos^2\theta)^2\cos^2\phi\sin^2\theta, \tag{6.14a}$$

$$Q_1(E3) = \frac{1}{16}(\cos^2\theta(11 - 15\cos^2\theta)^2\cos^2\phi + (1 - 5\cos^2\theta)^2\sin^2\phi), \tag{6.14b}$$

$$Q_2(E3) = \frac{5}{8}\sin^2\theta\left((1 - 3\cos^2\theta)^2\cos^2\phi + 4\cos^2\theta\sin^2\phi\right), \tag{6.14c}$$

$$Q_3(E3) = \frac{15}{16}\sin^4\theta(\cos^2\theta\cos^2\phi + \sin^2\phi). \tag{6.14d}$$

These results coincide with those of Refs. [103–105], and they clearly indicate a strong dependency of the relative intensities on the $\boldsymbol{B}$-field orientation.

One can see various dependencies: For example, if we choose a particular polarization orientation, there are still differences in the angle dependence of the excitation probability for different values of ΔM. This can be used in an experiment to increase or decrease certain relative intensities of the Zeeman levels by choosing both θ and ϕ in dependence on each other carefully [104].

We want to analyze the dependence on θ a little bit further. In order to do so, we focus on one example, namely the excitation of the sublevel with $M_i = 0$ to $M_f = 0$ in the $^{171}Yb^+$ ion exposed with linearly polarized octupole radiation ($p = 1, L = 3$), which is either parallel ($\phi = 0$) or perpendicular ($\phi = \pi/2$) to the plane spanned by $\boldsymbol{k}$ and $\boldsymbol{B}$ (see Fig. 6.3). We introduce $W_{\text{tot}}^{(\text{pl})}$, the total transition rate summed over the parallel and perpendicular polarization, and integrated over the magnetic field angle θ, to make the rates dimensionless and easier to compare, also with regard to the following comparison with twisted light. Then, the normalized transition rates for the absorption of parallelly polarized light are given by

$$\begin{aligned} W_{\parallel}^{(\text{pl})}(\theta) =& \frac{N}{W_{\text{tot}}^{(\text{pl})}} \left| \frac{1}{\sqrt{2}} \left[\mathcal{M}_{fi}^{(\text{pl})}(\lambda = +1) + \mathcal{M}_{fi}^{(\text{pl})}(\lambda = -1) \right] \right|^2 \\ =& \frac{[L]}{8} \left| i^p \, d^L_{+1\,\Delta M}(\theta) + (-i)^p \, d^L_{-1\,\Delta M}(\theta) \right|^2, \end{aligned} \tag{6.15}$$

where N is a constant, covering all constant prefactors of the transition rates. For perpendicular polarization we find

$$\begin{aligned} W_{\perp}^{(\text{pl})}(\theta) =& \frac{N}{W_{\text{tot}}^{(\text{pl})}} \left| \frac{i}{\sqrt{2}} \left[\mathcal{M}_{fi}^{(\text{pl})}(\lambda = -1) - \mathcal{M}_{fi}^{(\text{pl})}(\lambda = +1) \right] \right|^2 \\ =& \frac{[L]}{8} \left| - i^p \, d^L_{+1\,\Delta M}(\theta) + (-i)^p \, d^L_{-1\,\Delta M}(\theta) \right|^2. \end{aligned} \tag{6.16}$$

The advantage of introducing $W_{\text{tot}}^{(\text{pl})}$ is that we get rid of all additional factors, which can be found, for example, in Eq. (6.11). Moreover, after inserting $\mathcal{M}_{fi}^{(\text{pl})}(\lambda = -1)$ and $\mathcal{M}_{fi}^{(\text{pl})}(\lambda = +1)$ into Eq. (6.15) and (6.16), we find compact expressions (c.f. the 2nd lines of (6.15) and (6.16)) that are then easier to analyze. In particular, the combination of the small Wigner-d-functions in the second lines of these two expressions for $W_{\parallel}^{(\text{pl})}(\theta)$ and $W_{\perp}^{(\text{pl})}(\theta)$ reflects the geometry of the excitation process.
We can also use this notation to simplify Eq. 6.11 so that the transition rate for linearly polarized plane waves becomes the following

$$W_{\text{lin}}^{(\text{pl})}(\theta) \;=\; \frac{N}{W_{\text{tot}}^{(\text{pl})}} \left| \sum_{\lambda = \pm 1} (i\lambda)^p \, d^L_{\lambda\,\Delta M}(\theta) \, e^{-i\lambda\phi} \right|^2. \tag{6.17}$$

In Fig. 6.4, the (normalized) transition rates for the absorption of parallelly (black solid line) and perpendicularly (red dashed line) polarized plane-wave light are shown. It is noticeable that the probability to excite the $M_i = 0 \to M_f = 0$ octupole transition for a perpendicularly polarized plane wave is zero for all directions of the magnetic field. In contrast, there may be a non-zero probability for the excitation by plane-wave light with parallel polarization. To be more precise, for the latter case the corresponding transition probability exhibits an oscillatory behaviour as a function of the magnetic field angle θ. Principal maxima occur at $\theta = 30^\circ$ and $\theta = 150^\circ$,

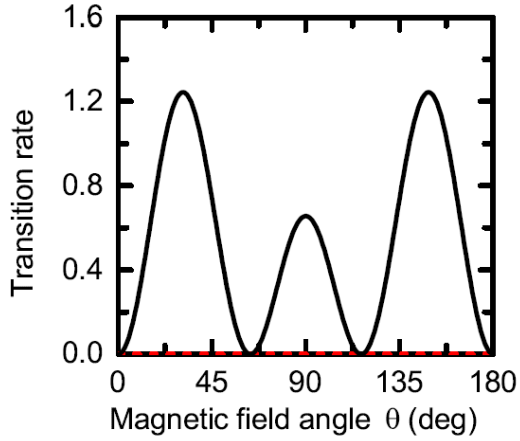

FIGURE 6.4: (Normalized) transition rates for absorption of parallel (black solid line) and perpendicular (red dashed line) linearly polarized plane-wave light. The results are shown as a function of magnetic field angle θ for the $^2S_{1/2}(F_i = 0, M_i = 0) \rightarrow {}^2F_{7/2}(F_f = 3, M_f = 0)$ electric octupole (E3) transition in a single $^{171}Yb^+$ ion. Calculations were performed for the photon energy $\hbar\omega = 2.65$ eV. The figure is taken from our publication, Ref. [70].

and one subsidiary maximum occurs between them at $\theta = 90°$. These results can also be derived from Eq. (6.14a): $Q_0(E3) \propto \cos^2\phi$. Therefore, $Q_0(E3)$ vanishes for perpendicular polarization ($\phi = \pi/2$). For parallel polarization ($\phi = 0$) the course is not so obvious but gives the values shown in Fig. 6.4.

Unfortunately, it is not possible to find such simple formulas, like Eq. (6.11), for twisted light, nevertheless, we will examine the angle dependencies for selected cases when the excitation is driven by with Bessel light beams in the following subsection.

6.4.2 Dependency of Transition Rates on the Magnetic Field Angle for Excitations with Twisted Light

After the discussion of the B-field orientation for plane-wave excitation, we continue now with the examinations for vortex light beams. The transition rate for parallelly polarized twisted light (3.15), again like in the plane-wave case normalized with $W_{\text{tot}}^{(\text{pl})}$ and N, can be derived with the help of Eq. (6.9) and is then given by

$$W_{\parallel}^{(\text{tw})}(\theta, \boldsymbol{b}) = \frac{N}{W_{\text{tot}}^{(\text{pl})}} \left| \frac{i}{\sqrt{2}} \left[\mathcal{M}_{fi}^{(\text{tw})}(m_l, \lambda = +1) - \mathcal{M}_{fi}^{(\text{tw})}(m_l, \lambda = -1) \right] \right|^2 . \quad (6.18)$$

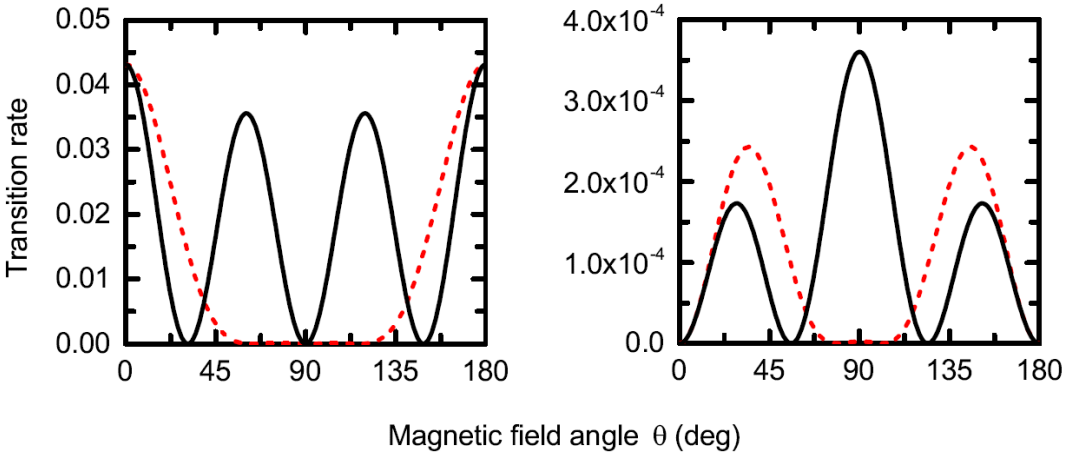

FIGURE 6.5: (Normalized) transition rates for absorption of parallel (black solid lines) and perpendicular (red dashed lines) linearly polarized twisted Bessel light with OAM $m_l = +1$ (left panel) and $m_l = +2$ (right panel), and an opening angle $\theta_k = 7.53°$. All other parameters are as in Fig. 6.4. The figures are taken from our publication, Ref. [70].

And, for perpendicularly polarized twisted light, we get

$$W_{\perp}^{(\mathrm{tw})}(\theta, \boldsymbol{b}) = \frac{N}{W_{\mathrm{tot}}^{(\mathrm{pl})}} \left| \frac{1}{\sqrt{2}} \left[\mathcal{M}_{fi}^{(\mathrm{tw})}(m_l, \lambda = +1) + \mathcal{M}_{fi}^{(\mathrm{tw})}(m_l, \lambda = -1) \right] \right|^2 . \quad (6.19)$$

If the atoms are placed at the beam center ($b = 0$) these equations can be simplified further and can be expressed with one formula, namely

$$W_{\parallel,\perp}^{(\mathrm{tw})}(\theta, b = 0) = \frac{[L]}{8} \Big| - i^{p+1}\, d^L_{m_l+1,\,+1}(\theta_k)\, d^L_{m_l+1,\,\Delta M}(\theta) \mp (-i)^{p-1}\, d^L_{m_l-1,\,-1}(\theta_k)\, d^L_{m_l-1,\,\Delta M}(\theta) \Big|^2 , \quad (6.20)$$

where we have used Eq. (6.10).

The orientation of the magnetic field with respect to the light field is especially important for transitions with a narrow linewidth. Therefore, the calculations in this chapter are based on the E3 hyperfine transition in the $^{171}\mathrm{Yb}^+$ ion, due to its very narrow linewidth. We start by presenting in Fig. 6.5 the results for the excitation of an atom centered on the beam axis ($b = 0$). The transition is induced by vortex light with an opening angle of $\theta_k = 7.53°$ and photon energy of $\hbar\omega = 2.65$ eV, which is in resonance with the electric octupole transition (see Fig. 6.1).

At this point, we have to put a short explanation in between. The expressions (3.14)-(3.17), which were introduced in Chapter 3 to describe the different polarizations of twisted Bessel beams, have been derived for the paraxial regime. Consequently, the question arises: What is the maximum angle θ_k that can be used so that these formulas are still applicable? The paraxial regime applies to twisted light with small

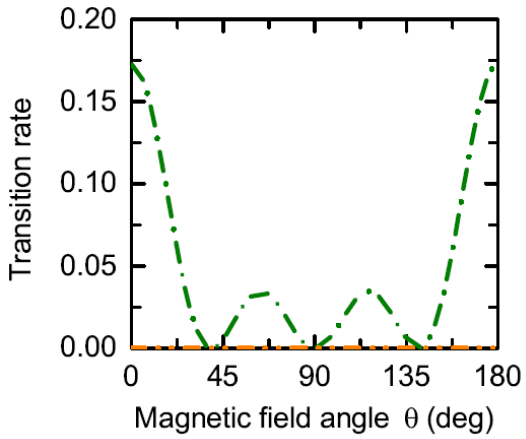

FIGURE 6.6: Transition rates for absorption of radially (green dash-dotted line) and azimuthally (orange dash-dot-dotted line) polarized Bessel beams. All other parameters are as in Fig. 6.4. The figure is taken from our publication, Ref. [70].

opening angles for which $\sin\theta_k \approx \theta_k$, $\tan\theta_k \approx \theta_k$ and $\cos\theta_k \approx 1$ applies [41]. Of course, strict limits cannot be specified for an approximation. The applicability of an approximation always depends on the desired accuracy. In our case, the deviation is small for angles below 10°, and accordingly, the paraxial approximation can be used.

The rates are shown for parallelly (black solid lines) and perpendicularly (red dashed lines) polarized light with an OAM projection of $m_l = +1$ (left panel) and $m_l = +2$ (right panel). Again, large differences between the two polarization states can be determined. Nevertheless, the results differ considerably from those for plane waves (see Fig. 6.4). While in the plane-wave case the rate (for $\Delta M = 0$) for perpendicular polarization was always zero regardless of θ, in the twisted case it no longer vanishes everywhere: For certain orientations of the magnetic field, depending on the OAM protection, the rate increases remarkably. The maxima occur at magnetic field angles $\theta = 0°$ and $\theta = 180°$ for OAM $m_l = +1$, or at $\theta = 35°$ and $\theta = 145°$ if OAM $m_l = +2$. In the case of parallel polarization, the excitation probability is now also enhanced at other angles, namely, if OAM $m_l = +1$, then they are at $\theta = 0°, 60°, 120°,$ and 180°, whereby the maxima at 60° and 120° are a bit lower. For OAM $m_l = +2$ the principal maximum occurs at $\theta = 90°$ with two sidelobes at $\theta = 30°$ and 150°. By looking at the values on the y-axis in Fig. 6.5, it is worth stressing, that the excitation of ions centered on the beam axis is less probable than the excitation with plane-wave radiation. This is due to the fact, that the light intensity at the beam center is decreased and this leads to a small excitation probability. For example, the probability with a vortex beam with OAM $m_l = +1$ is 30 times smaller than one obtained with a plane wave. And for light carrying an OAM of $m_l = +2$ it is even 3000 times smaller.

As we have mentioned in Sec. 3.5, twisted light beams can be apart from linearly and circularly polarized, also radially or azimuthally polarized. Next, we shall consider the angular dependence when the ion is exposed to light in one of these polarization states.

The transition rate for the absorption of radially polarized radiation is given in terms of the matrix elements (6.8) by

$$W_{\mathrm{r}}^{(\mathrm{tw})}(\theta, \boldsymbol{b}) = \frac{N}{W_{\mathrm{tot}}^{(\mathrm{pl})}} \left| -\frac{i}{\sqrt{2}} \left[\mathcal{M}_{fi}^{(\mathrm{tw})}(m_l = -1, \lambda = +1) + \mathcal{M}_{fi}^{(\mathrm{tw})}(m_l = +1, \lambda = -1) \right] \right|^2 , \tag{6.21}$$

and for the azimuthal polarization, we find

$$W_{\mathrm{az}}^{(\mathrm{tw})}(\theta, \boldsymbol{b}) = \frac{N}{W_{\mathrm{tot}}^{(\mathrm{pl})}} \left| \frac{1}{\sqrt{2}} \left[\mathcal{M}_{fi}^{(\mathrm{tw})}(m_l = +1, \lambda = -1) - \mathcal{M}_{fi}^{(\mathrm{tw})}(m_l = -1, \lambda = +1) \right] \right|^2 . \tag{6.22}$$

Again, these expressions can be simplified by considering the atoms to be well-localized on the beam axis ($b = 0$). Then we can use Eq. (6.10), insert it in Eqs. (6.21) and (6.22), and obtain the transition rates

$$W_{\mathrm{r,az}}^{(\mathrm{tw})}(\theta, b = 0) = \frac{[L]}{8} \left| d^L_{0\,\Delta M}(\theta) \right|^2 \left| (-i)^p \, d^L_{0\,-1}(\theta_k) \pm i^p \, d^L_{0\,+1}(\theta_k) \right|^2 , \tag{6.23}$$

where we have used the fact that both twisted components have the TAM projection $m_\gamma = m_l + \lambda = 0$. The results for these calculations are shown in Fig. 6.6. Here, it is noticeable that the transition rate for the electric octupole (E3) $M_i = 0 \to M_f = 0$ transition for azimuthally polarized beams (red dashed line) is zero, independently of the magnetic field angle θ, if the ion is placed in the vortex ($b = 0$). However, for the absorption with radially polarized light (green dashed-dotted line) the transition rate can be enhanced for certain $\boldsymbol{B}$-field orientations: It is increased when both the propagation direction of the light $\boldsymbol{k_z}$ and the magnetic field ($\theta = 0^\circ$ and 180°) are in parallel to each other. In between, there are two sidelobes at $\theta = 65^\circ$ and 115°. Again, a decrease in the probability compared to the plane-wave analog can be determined. At this time it is about 7 times lower.

Above, in Sections 4.4.3 and 5.2.4, we have mentioned that the precise positioning of an atom is very hard to realize in experiments. Therefore, the atomic position is at best known as an averaged value. In order to take into account the experimental scenario, additional calculations were performed to examine the effect of the spatial distribution of the atom placed at the beam axis on the excitation probability.

In Fig. 6.7 the (normalized) transition rates (4.35) for parallelly (left panel) and perpendicularly (right panel) polarized Bessel beams with an OAM of $m_l = +2$ are plotted for an ion with a position distribution of $\sigma = 20$ nm (red dashed lines) and

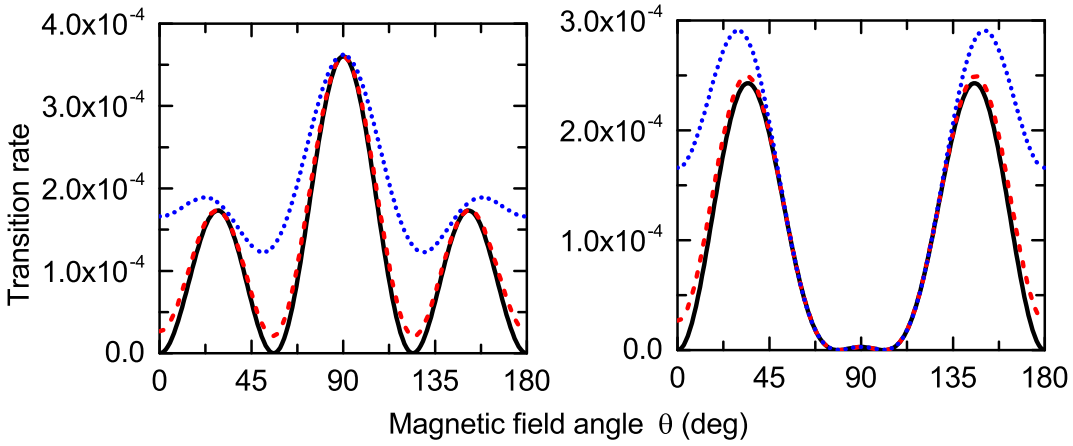

FIGURE 6.7: Transition rates for the absorption of parallel (left panel) and perpendicular (right panel) linearly polarized twisted Bessel light with OAM $m_l = +2$ by a single-ion, which is well-located on the beam axis (black solid lines), or has a spatial spread of $\sigma = 20$ nm (red dashed lines) or $\sigma = 50$ nm (blue dotted lines) in the beam center. All other parameters are as in Fig. 6.5. The figures are taken from our publication, Ref. [70].

$\sigma = 50$ nm (blue dotted lines). For comparison, the case of an atom centered perfectly at the beam axis (black solid lines) is also shown. As seen from the figure, the rates increase with rising uncertainty σ when the magnetic field is (nearly) parallel to the light propagation direction, but not for the orientation perpendicular. Moreover, it can also be seen that the maximum values are slightly shifted to other angels. This has consequences for experimental applications. It is important to choose the orientation in such a way that the transition rate is maximized. The transitions used are often very narrow so that the highest possible rate should be sought.

Fig. 6.8 depicts the (normalized) transition rates for the absorption of radially (left panel) and azimuthally (right panel) polarized twisted Bessel light with OAM $m_l = +2$ and an opening angle $\theta_k = 7.53°$ when a single ion is either well-located on the beam axis (black solid lines), or has a spatial spread of $\sigma = 20$ nm (red dashed lines) or $\sigma = 50$ nm (blue dotted lines) in the beam center. The figure shows that the transition rate for radially polarized light is insensitive to modifications of the ion spatial distribution, while the rates for azimuthally polarized could become non-zero for an ion that is not well-positioned on the beams axis. Besides, the values seem to approach the values of parallelly polarized plane waves.

The results show that with increasing σ, the transition rates become larger. But at the same time, the twisted light effects smear out.

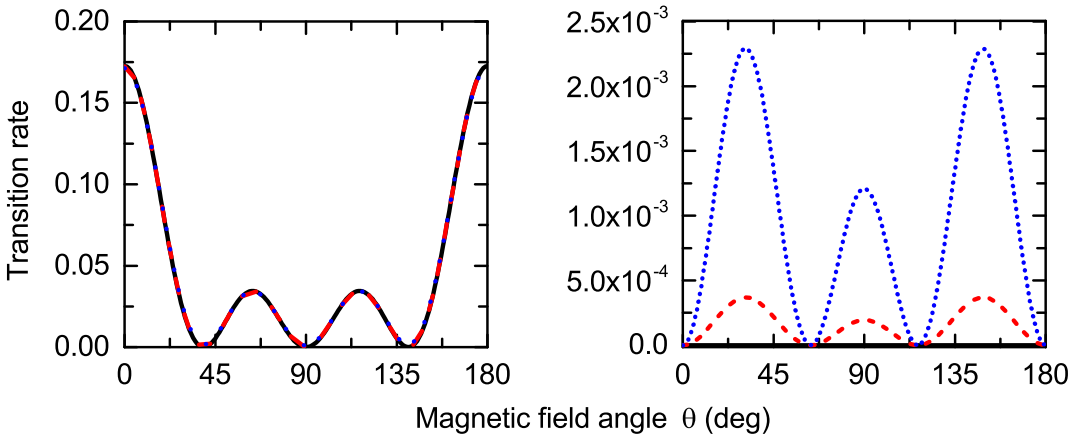

FIGURE 6.8: Transition rates for the absorption of radially (left panel) and azimuthally (right panel) polarized twisted Bessel light with OAM $m_l = +2$ and an opening angle $\theta_k = 7.53°$ by a single ion, which is well-located on the beam axis (black solid lines), or has a spatial spread of $\sigma = 20$ nm (red dashed lines) or $\sigma = 50$ nm (blue dotted lines) in the beam center. All other parameters are as in Fig. 6.5. The figures are taken from our publication, Ref. [70].

6.5 Light Shift

We have seen that the excitation probabilities strongly depend on the alignment of the applied magnetic field, but at the same time, the polarization of the used light also plays a major role. As already mentioned above the linewidth of electric-dipole forbidden transitions are usually very narrow. Therefore, it is essential to choose the alignment angle θ in such a way that the transition rates are maximized. However, the electric field of the laser disturbs the atomic levels, which is known as the *AC-Stark effect*.

The Stark effect originates from the interaction between the atom and an external electric field. This perturbation leads to a shift, the *Stark shift*, of the atomic levels. However, this shift is generally different for each atomic level. Due to this the distance between the levels also changes and thus the required frequency for the excitation. If the disturbing $\boldsymbol{E}$-field is not static but dynamical, it is referred to as AC-Stark effect. If the interference is caused by a laser field, one sometimes speaks of a *light shift*.

In the remaining part of this chapter, we will investigate in detail how twisted light can be used to decouple the atom (or ion) from the field environment and consequently reduce the AC-Stark shift.

6.5.1 Theory of the Light Shift

The light shift (AC-Stark shift) is a phenomenon whereby the energy levels of an atom are disturbed by an external dynamic electric field, and depends, on the dynamical polarizabilities of the atomic states and the laser intensity. To analyze the AC-Stark effect, we will treat the oscillating E-field of a laser beam $\boldsymbol{E}(t) = E_0 \boldsymbol{e}_\lambda e^{-(i\omega t - \boldsymbol{k}\cdot\boldsymbol{r})}$ with E_0 being the field amplitude and $\boldsymbol{e}_\lambda$ the polarization vector, as a perturbation.

The theory of the quadratic Stark shift for the hyperfine structure of a free atom is presented in [106]. In their work, a perturbation theory approach is performed and according to this the AC-Stark shift is given by

$$\Delta\nu_{AC} = -\frac{|\boldsymbol{E}|^2}{4}\left(2\,\Delta\alpha_S + \left(3\cos^2\theta - 1\right)\frac{3M_f^2 - F(F+1)}{F(2F-1)}\,\Delta\alpha_T\right), \tag{6.24}$$

where differential polarizabilities $\Delta\alpha_{S,T} = \alpha_{S,T}^{(i)} - \alpha_{S,T}^{(f)}$ are the differences between the scalar α_S and tensorial α_T polarizabilities of the ground state and the excited state, and $\boldsymbol{E}$ is the electric field of the laser. From this expression one can obtain, that the light shift $\Delta\nu_{AC}$ is proportional to the squared electric field $\boldsymbol{E}^2$. If one wants to reduce the value of the shift, there are two options: One is to lower the polarizabilities α_S and α_T, the other is to decrease the laser intensity. Polarizability is an atomic property. Therefore, it is only possible to reduce it by changing the atom, but this is avoided because the atom has other advantages. Next, let us explain the idea that allows excitations with low intensity by using Bessel beams.

6.5.2 AC-Stark Shift: Calculations

After having briefly discussed the theory of the AC-Stark above, we now want to consider a concrete example, and calculate the frequency shift for the E3 hyperfine transition in $^{171}\mathrm{Yb}^+$. The calculations are performed for the electric-octupole (E3) hyperfine transition $4f^{14}6s\ {}^2S_{1/2} \rightarrow\ 4f^{13}6s^2\ {}^2F_{7/2}$ in the $^{171}\mathrm{Yb}^+$ ion, which is used as the clock transition in the Yb clock at the PTB [39]. This transition has one outstanding feature: The lifetime of the excited state is in the range of about ten years [105, 107]. Based on this transition a single-ion clock with a current systematic uncertainty of $3.2 \cdot 10^{-18}$ was realized [39]. A long lifetime is directly connected to a very narrow line width. As already mentioned before, to achieve the needed population in the ${}^2F_{7/2}$ state a high laser power must be used, which leads to a significant light shift. Therefore, this transition is a suitable candidate for the application of twisted light.

Theoretical calculations for the dynamical polarizabilities of a realistic atom are non-trivial and complex [108]. Therefore, we used values for the scalar and tensorial differential polarizabilities of the octupole transition, which were obtained experimentally and are, respectively, $\Delta\alpha_S = 0.854 \cdot 10^{-40} JV^{-2}m^2$

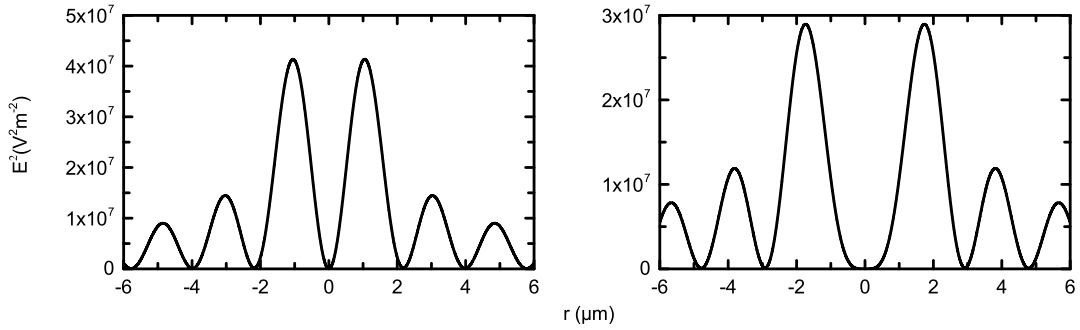

FIGURE 6.9: Squared of the electric field for a parallel linearly polarized twisted Bessel beam of photon energy $\hbar\omega = 2.65$ eV and with an opening angel $\theta_k = 7.53^\circ$, and two different OAM projections, namely $m_l = 1$ (left panel) and $m_l = 2$ (right panel).

and $\Delta\alpha_T = -0.206 \cdot 10^{-40} J V^{-2} m^2$ [109].

The light shift (6.24) is mainly influenced by the electric field. Hence, we first investigate the transverse $\boldsymbol{E}$-field of the light. A plane wave has a homogenous transverse intensity profile, see Fig. 2.1(a). Thus, both values, the squared electric field $\boldsymbol{E}^2$ and the light shift $\Delta\nu_{AC}$ are constant in the transverse plane. With the help of Eq. (2.48) the electric field of the twisted Bessel beams can be computed. Fig. 6.9 depicts the squared of the electric field for a twisted Bessel beam with an OAM projection $m_l = 1$ (left panel) and $m_l = 2$ (right panel) as a function of the radial distance from the beam center. The laser intensity is proportional to $\boldsymbol{E}^2$. Consequently, the ring structure of the intensity profile, which can be clearly seen from the figure, is expected (c.f. Fig. 2.3). There is an intensity minimum in the beam center for both cases $m_l = 1$ (left panel) and $m_l = 2$ (right panel). However, for $m_l = 2$ the first maximum is further away from the beam center and its magnitude is about a third smaller than it is the case for the beam with $m_l = 1$.

Now, let us consider the light shift. We are especially interested in the differences between the light shift induced by the excitation with plane waves and the shift caused by twisted radiation. Therefore, the resented light shift in Fig. 6.10 is calculated as the ratio $\Delta\nu_{AC}^{(\mathrm{tw})}/|\Delta\nu_{AC}^{(\mathrm{pl})}|$, where $\Delta\nu_{AC}^{(\mathrm{pl})}$ is the light shift created by plane-wave radiation with the same polarization, that is considered for $\Delta\nu_{AC}^{(\mathrm{tw})}$, but with another magnetic field angle θ. The reason for this is the following: We want to compare the AC-Stark shifts for maximized transition probability. However, we have seen in the previous section that for different radiation fields the magnetic field angle θ, i.e. the alignment between the external magnetic field and the propagation direction of the light beam, needs to be examined individually. Consequently, also the angle $\theta_{\max}$ to maximized the transition probability is different. In Fig. 6.10 we display the light shift ratio $\Delta\nu_{AC}^{(\mathrm{tw})}/|\Delta\nu_{AC}^{(\mathrm{pl})}|$ of the E3 hyperfine transition in $^{171}\mathrm{Yb}^+$ for parallel linear polarization. For the twisted radiation two OAM projections were considered,

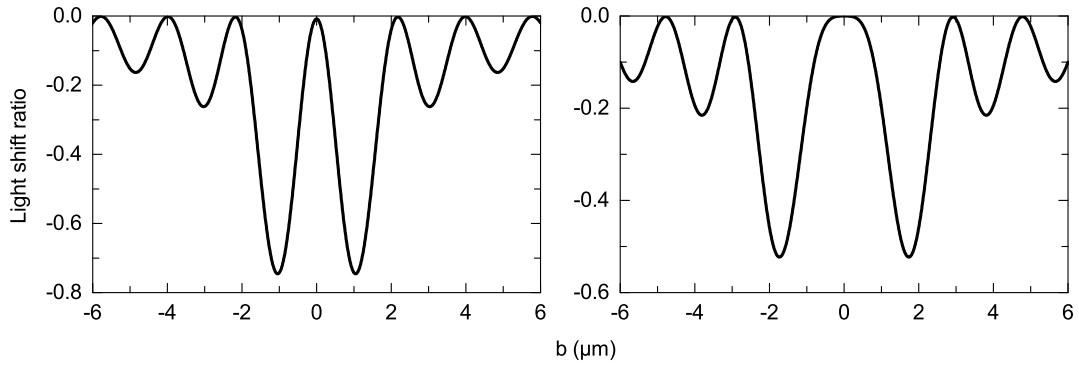

FIGURE 6.10: Light shift ratios $\Delta\nu_{AC}^{(\mathrm{tw})}/|\Delta\nu_{AC}^{(\mathrm{pl})}|$ for the E3 hyperfine transition in $^{171}\mathrm{Yb}^{+}$ induced by parallel linearly polarized light. Two OAM projection, $m_l = 1$ (left panel) and $m_l = 2$ (right panel), were used for the twisted radiation. The calculations have been performed for the corresponding magnetic field angles of $\theta_{\mathrm{max}}^{(\mathrm{tw})} = 90^\circ$ for $m_l = 1$ and $\theta_{\mathrm{max}}^{(\mathrm{tw})} = 0^\circ$ for $m_l = 2$, and for the plane wave $\theta_{\mathrm{max}}^{(\mathrm{pl})} = 30^\circ$, i.e., the angles θ_{max} were chosen to maximize the transition rate.

$m_l = 1$ (left panel) and $m_l = 2$ (right panel). In the calculations the magnetic field angle θ was chosen in such a way that the transition probability is maximized, see Fig. 6.5. Thus, for $m_l = 1$ (left panel) this angle is $\theta_{\mathrm{max}}^{(\mathrm{tw})} = 90^\circ$ for $m_l = 2$ (right panel) it is $\theta_{\mathrm{max}}^{(\mathrm{tw})} = 0^\circ$, and for the plane wave $\theta_{\mathrm{max}}^{(\mathrm{pl})} = 30^\circ$ (c.f. Fig. 6.4). The results are shown as a function of the impact parameter b. As seen from these figures, in the beam center, where the laser intensity is low, the light shift can be significantly reduced, when twisted light is used for the excitation instead of plane-wave radiation. Moreover, a compassion between the left ($m_l = 1$) and the right panel $m_l = 2$ of Fig. 6.10 indicates, that higher topological charges induce a lower light shift. For $b = 0$ the electric field of an OAM carrying beam vanishes. Consequently, the light shift would also disappear. However, as we argued before, this is only theoretically possible, if the atom is perfectly positioned in the beam center. Therefore, in the realistic case of a delocalized atom, there will always be at least a small shift.

To conclude this section, however, we can say that our results show the following. For a well-chosen magnetic field angle, the photoexcitations of single trapped atoms by twisted light with different polarizations are possible and result in a significantly reduced light shift compared to excitations by plane-wave radiation.

Chapter 7

Summary and Outlook

In the present thesis, we theoretically investigated the photoexcitation of single atoms (or ions) by twisted Bessel beams. To do so, we started in Chapter 2 with the theory of light based on Maxwell's equations. We considered three different solutions of the wave equation: Firstly, we briefly reviewed the plane-wave solutions, followed by the spherical waves and the multipole expansion of the radiation field. And finally, we introduced the twisted Bessel beams. The vector potentials and basic characteristics for both, plane-wave and twisted light beams, were presented. In contrast to the plane waves, the transverse intensity profile of vortex beams is highly inhomogeneously consisting of concentric rings with an intensity minimum in the beam center. Moreover, it was shown that these twisted photons carry orbital angular momentum along their propagation direction. However, we explained that OAM and SAM are only for small opening angles (in the paraxial regime) well-defined.

We started Chapter 3 with a general introduction to the polarization of light. Then we introduced the *Stokes parameters*, which are defined in terms of observables, and allow a characterization of the radiation field. We discussed how to construct linearly, radially, and azimuthally polarized Bessel beams. Our analysis showed that one has to consider the time-averaged radiation field in order to get results that can be related to experimental observations. We found that the polarization for twisted beams is position depended. While ordinary polarization states of plane waves can be classified by the *Poincaré sphere*, for polarization states of these vector beams *higher order Poincaré spheres* need to be used.

Next, in Chapter 4, we focused on the interaction between the atom and the light. The well-established *density matrix formalism* allowed us to describe the state of the atom before and after the interaction. To describe the dynamic behaviour of the system we made use of the relativistic first-order perturbation theory, which led us to the expression of the transition matrix element for the photoabsorption. Afterwards, we used this formalism to investigate the interaction of a single atom with plane-wave or twisted radiation. For both cases, we presented detailed expressions for the matrix elements and transition rates. In this analysis, special attention was paid to the position of the atom. First, we considered the theoretical scenario of a well-localized atom. Afterwards, we investigated the more realistic situation, where the atomic position can at best be specified with some uncertainty. We completed this

chapter with a consideration of the selection rules. It was shown that the selection rules for the excitation by twisted photons are modified in comparison to those for plane waves. We emphasized that also here the position of the atom within the wavefront has a high influence on the result.

Then, in Chapter 5, we applied this theoretical framework to examine the multipole excitation of fine-structure levels. In particular, we focused here on the scenario, where the transition is just allowed via two multipole channels. We found that the total transition rates, i.e. the summations over all electric and magnetic multipole transitions, can be expressed solely in terms of *individual* multipole transition rates without any interference terms. Our results have shown that the use of twisted light can significantly modify the relative strength of these multipole channels. In order to quantify this modification we introduced the *geometrical factor*. It was found that this factor reflects the kinematic properties and the topological charge of the incident beam, but is independent of the electronic structure of the target atom. Moreover, it is sensitive to the atomic position. Therefore, we introduced the *averaged geometrical factor*, which accounts for the case of a not well-localized atom. It is worth noting that this method is universal and can be applied to any atomic system. However, our analysis has shown that in order to achieve an efficient modification by twisted light, precise localization of the target atom is imperative.

Finally, in Chapter 6, we analyzed transitions between magnetic hyperfine levels. We began by explaining the advantages of the application of twisted light in (precision) experiments. We established a formalism that accounts also for the alignment of the applied magnetic field with respect to the light propagation direction. Special attention was paid to the electric octupole (E3) hyperfine transition $^2S_{1/2}(F=0) \to {}^2F_{7/2}(F=3)$ in the $^{171}\mathrm{Yb}^+$ ion, which is used in the Ytterbium single-ion clock. We explained that due to the narrow linewidth a precise alignment of the magnetic field is mandatory to achieve the configuration for the highest transition probability. At this point, it is important to note that the maximization of the transition probability depends not only on the direction of the applied magnetic field but also on the polarization and the topological charge of the incident light beam. Although the calculations were performed for the electric octupole (E3) hyperfine transition $^2S_{1/2}(F=0) \to {}^2F_{7/2}(F=3)$ in the $^{171}\mathrm{Yb}^+$ ion, the derived expressions are general and can be employed to any atomic transition of arbitrary multipole order.

The suggestions for further research can be divided into two main scopes: On the one hand, the inclusion of target objects others than single atoms, and, on the other hand, the investigation of photoexcitation by twisted light beams others than Bessel beams. Let us delve into the first research direction a little further. In this work, was only the excitation of a single atom considered, but the application of the developed formalism to other target objects, such as several atoms, mesoscopic or macroscopic atomic targets, and molecular targets, would be very interesting. We have seen, that many properties of the twisted light are position-dependent and it is not clear how

the twisted beams modify the interaction with such objects. First studies in this direction have already been performed for the excitation of mesoscopic atomic targets [110, 111]. These studies have shown that effects with twisted light can also be observed for larger targets. However, it would be interesting, how different multipole orders influence the photoabsorption and which impact on the topological charge, the alignment of the magnetic field, and the polarization of the light have on these processes.

In addition to another target, one can also think about using a different type of twisted beam for the excitation. In this work, we considered Bessel beams. But there are other twisted beam types, for example, Laguerre-Gaussian or Bessel-Gaussian beams. Our present computations were carried out for a Bessel beam only, the results obtained here are also applicable to the excitation with a twisted Laguerre-Gaussian beam of the same frequency, orbital angular momentum (OAM), and polarization. This is due to the fact that both the paraxial Bessel and Laguerre-Gaussian beams with non-zero OAM m_l behave like $r^{m_l} e^{i m_l \varphi}$ for small r. When the atoms are placed close to the beam center, the results should be nearly the same. Nevertheless, it would be interesting to know, how these beams behave when the atom is not placed close to the beam center, and how (strong) focussing affect the process. At the end of this thesis, was the *light shift* examined. In the experiments, the transition is stimulated with a pulsed laser. Therefore it would be interesting to consider this aspect in future considerations.

Appendix A

Transition Matrix Elements

The final equations of the transition matrix elements were already used in the main part of the thesis. However, here in the appendix, we provide the full calculation. Some parts will be repeated from Chapter 6, but we would like to present here a complete derivation of the transition matrix element. We will derive the expressions for the most general case: the excitation of hyperfine-structure levels which are spilt by an applied magnetic field with arbitrary orientation regarding the propagation direction of the light. We start with the excitation by plane waves. Afterwards we derive the transition matrix element for the excitation driven by a twisted Bessel beam.

A.1 Plane-wave Matrix Element

The transition amplitude to be calculated is given in Chapter 6 by Eq. (6.2) and has the following form

$$\mathcal{M}_{fi}^{(\mathrm{pl})} = \left\langle \alpha_f F_f M_f \left| \sum_q \boldsymbol{\alpha}_q \cdot \boldsymbol{\mathcal{A}}^{(\mathrm{pl})}(\boldsymbol{r}_q) \right| \alpha_i F_i M_i \right\rangle , \tag{A.1}$$

where, just to remind, $\boldsymbol{\mathcal{A}}^{(\mathrm{pl})}$ (2.10) is the plane-wave vector potential introduced in Chapter 2, and $F_{f,i}$ and $M_{f,i}$ are the total angular momenta and the corresponding projections onto the quantization (z_{atom}), all additional quantum numbers are denoted by $\alpha_{f,i}$.

As already mentioned in Chapter 6, we assume that the light interacts only with the electrons, and not with the nucleus. Therefore, the nuclear and electronic degrees of freedom decouple and we can write them as follows

$$|\alpha_k F_k M_k\rangle = \sum_{M_{J_k} M_I} \left\langle J_k M_{J_k}\, I M_I \mid F_k M_k' \right\rangle |\alpha_k J_k M_{J_k}\rangle\, |I M_I\rangle , \tag{A.2}$$

where $|\alpha_k F_k M_k\rangle$ is a linear combinations of the corresponding atomic $|\alpha_k J_k M_{J_k}\rangle$ and nuclear states $|I M_I\rangle$. The rotation of the atomic quantization axis (z_{atom}) to the light

axis (z_{light}) can be performed with a Wigner-D matrix, given by

$$\left|\alpha_k F_k M_k'\right\rangle = \sum_{M_k'} D^{F_k}_{M_k M_k'}(\phi,\theta,0)\left|\alpha_k F_k M_k'\right\rangle, \tag{A.3}$$

where index k denotes either the quantum numbers of the initial (i) or the final (f) atomic state, M_k and M_k' are projections onto the axes z_{atom} and $z(z_{\text{light}})$, respectively. And, $D^{F_k}_{M_k M_k'}(\phi,\theta,0)$ is the Wigner-D function with θ being the angle between the light propagation direction (along z_{light}) and the atomic quantization axis z_{atom} and ϕ determines the tilt of the electric field vector with respect to the plane spanned by the magnetic field and the propagation direction, see Fig. 6.3.

Now, we have collected all equations that are needed to compute the matrix element A.1. Firstly, we substitute Eq. (A.3) into Eq. (A.1) and get

$$\mathcal{M}^{(\text{pl})}_{fi} = \left\langle \alpha_f F_f M_f \left| \sum_q \boldsymbol{\alpha}_q \cdot \boldsymbol{\mathcal{A}}^{(\text{pl})}(\boldsymbol{r}_q) \right| \alpha_i F_i M_i \right\rangle \tag{A.4}$$

$$= \sum_{M_f', M_i'} D^{F_f\,*}_{M_f M_f'}(\phi,\theta,0) D^{F_i}_{M_i M_i'}(\phi,\theta,0) \left\langle \alpha_f F_f M_f' \left| \sum_q \boldsymbol{\alpha}_q \cdot \boldsymbol{\mathcal{A}}^{(\text{pl})}(\boldsymbol{r}_q) \right| \alpha_i F_i M_i' \right\rangle .$$

Secondly, we decouple the nuclear and electronic wave functions, so that

$$\mathcal{M}^{(\text{pl})}_{fi} = \sum_{M_f', M_i'} \sum_{M_{J_f}, M_{I_i}, M_I} \left\langle J_i M_{J_i}\ I M_I \mid F_i M_i' \right\rangle \left\langle J_f M_{J_f}\ I M_I \mid F_f M_f' \right\rangle$$

$$\times D^{F_f\,*}_{M_f M_f'}(\phi,\theta,0) D^{F_i}_{M_i M_i'}(\phi,\theta,0) \left\langle \alpha_f F_f M_f' \left| \sum_q \boldsymbol{\alpha}_q \cdot \boldsymbol{\mathcal{A}}^{(\text{pl})}(\boldsymbol{r}_q) \right| \alpha_i F_i M_i' \right\rangle . \tag{A.5}$$

In order to multiply the two Wigner-D functions, we use the following transformation of the Wigner-D function [85]

$$D^{F_f\,*}_{M_f M_f'}(\phi,\theta,0) = (-1)^{M_f - M_f'} D^{F_f}_{-M_f - M_f'}(\phi,\theta,0), \tag{A.6}$$

and then we can perform the multiplication [85]

$$\begin{aligned} D^{F_f\,*}_{M_f M_f'}(\phi,\theta,0) D^{F_i}_{M_i M_i'}(\phi,\theta,0) \;&=\; (-1)^{M_f - M_f'} \sum_{\nu=|F_f - F_i|}^{F_f + F_i} \sum_{\mu,\mu'} \left\langle F_i M_i \;\; F_f \mid \nu\mu \right\rangle \\ &\quad \times \left\langle F_i M_i'\, F_f - M_f' \mid \nu\mu' \right\rangle D^{\nu}_{\mu\mu'}(\phi,\theta,0) . \end{aligned} \tag{A.7}$$

As next step, we apply the Wigner-Eckard theorem (4.25) and expand the vector potential in its multipole terms (2.27). To sum up, these steps lead us to the following

expression

$$\begin{aligned}\mathcal{M}_{fi}^{(\mathrm{pl})} &= \sum_{\substack{M_f',M_i',\\ M_{J_f},M_{J_i},M_I}} \left\langle J_i M_{J_i}\ IM_I \mid F_i M_i' \right\rangle \left\langle J_f M_{J_f}\, IM_I \mid F_f M_f' \right\rangle \\ &\quad \times (-1)^{M_f - M_f'} \sum_{\nu,\mu,\mu'} \left\langle F_i M_i \ \ F_f - M_f \mid \nu\mu \right\rangle \left\langle F_i M_i' \, F_f - M_f' \mid \nu\mu' \right\rangle D^{\nu}_{\mu\mu'}(\phi,\theta,0) \\ &\quad \times \sqrt{2\pi} \sum_{L,M,p} i^L \,[L]^{1/2}\, (i\lambda)^p \, D^L_{M\lambda}(\varphi_k,\theta_k,0)\, \frac{1}{[J_f]} \left\langle J_i M_{J_i}\ LM \mid J_f M_{J_f} \right\rangle \\ &\quad \times \left\langle \alpha_f J_f \,\|H_\gamma(pL)\|\, \alpha_i J_i \right\rangle , \end{aligned} \tag{A.8}$$

where we used again the short-hand notation (4.27)

$$\left\langle \alpha_f J_f \,\|H_\gamma(pL)\|\, \alpha_i J_i \right\rangle = \left\langle \alpha_f J_f \left\| \sum_q \boldsymbol{\alpha}_q \cdot \boldsymbol{a}_L^{(p)}(\mathbf{r}_q) \right\| \alpha_i J_i \right\rangle .$$

This expression (A.8) can be simplified by carrying out the summations. First, we sum over M_f', M_i', and M_I, and get the following

$$\begin{aligned}&\sum_{\substack{M_f',M_i',\\ M_I}} (-1)^{M_f - M_f'} \left\langle J_i M_{J_i}\ IM_I \mid F_i M_i' \right\rangle \left\langle J_f M_{J_f}\, IM_I \mid F_f M_f' \right\rangle \left\langle F_i M_i' \, F_f - M_f' \mid \nu\mu' \right\rangle \\ &\quad = (-1)^{M_f - M_{J_i} + J_f - M_{J_f} + \nu + I} \, \frac{[F_i,F_f]^{1/2}}{[J_i,J_f]^{1/2}} \, [\nu,J_i]^{1/2} \\ &\qquad \times \left\langle \nu\mu'\, J_i - M_{J_i} \mid J_f - M_{J_f} \right\rangle \left\{ \begin{array}{ccc} F_f & F_i & L \\ J_i & J_f & I \end{array} \right\} . \end{aligned} \tag{A.9}$$

Next, we perform the summation over the two quantum numbers M_{J_f} and M_{J_i}

$$\begin{aligned}&\sum_{M_{J_f},M_{J_i}} \left\langle J_i M_{J_i}\ LM \mid J_f M_{J_f} \right\rangle \left\langle \nu\mu'\, J_i - M_{J_i} \mid J_f - M_{J_f} \right\rangle \\ &\qquad = \frac{[J_f]}{[L,\nu]^{1/2}} \, \delta_{L,\nu} \, \delta_{-M,\mu'} . \end{aligned} \tag{A.10}$$

If we put it all together, we get the following

$$\begin{aligned}\mathcal{M}_{fi}^{(\mathrm{pl})} &= \sum_{L,M,p} \sqrt{2\pi}\, i^L \,[L]^{1/2}\, (i\lambda)^p \, D^L_{M\lambda}(\varphi_k,\theta_k,0) \left\{ \begin{array}{ccc} F_f & F_i & L \\ J_i & J_f & I \end{array} \right\} \\ &\quad \times D^L_{-M\ -\Delta M}(\phi,\theta,0)\, [F_i,L]^{1/2}\, (-1)^{F_i + J_f + L + I + \Delta M} \\ &\quad \times \left\langle F_i M_i \ \ L\Delta M \mid F_f M_f \right\rangle \left\langle \alpha_f J_f \,\|H_\gamma(pL)\|\, \alpha_i J_i \right\rangle , \end{aligned} \tag{A.11}$$

with $\Delta M = M_f - M_i$. A remaining step is to express the Wigner-D function in terms of the small Wigner-d function

$$D^L_{-M\,-\Delta M}(\phi,\theta,0) = (-1)^{-\Delta M+M}\, e^{+iM\phi}\, d^L_{M\,\Delta M}(\theta)\,. \tag{A.12}$$

If we assume that the circularly polarized plane-wave is propagating along the z-axis, $D^L_{M,\lambda}(\varphi_k,\theta_k,0) \to \delta_{M,\lambda}$, and we get the final form of the transition amplitude

$$\mathcal{M}^{(\mathrm{pl})}_{fi} = \sum_{Lp} C^{F_iF_fI}_{\alpha_iJ_i\alpha_fJ_f}(pL)\ (i\lambda)^p (-1)^{-\Delta M+M} e^{iM\phi}\, d^L_{\lambda\Delta M}(\theta)\, \left\langle F_iM_i\, L\Delta M \mid F_fM_f \right\rangle , \tag{A.13}$$

where $C^{F_iF_fI}_{\alpha_iJ_i\alpha_fJ_f}(pL)$ is a constant factor for a particular transition and contains all information about the dynamics of the excitation process. It is defined by

$$\begin{aligned} C^{F_iF_fI}_{\alpha_iJ_i\alpha_fJ_f}(pL) \;&=\; \sqrt{2\pi}\, i^L [L,F_i]^{1/2}\, (-1)^{J_f+I+F_i+L} \\ &\quad\times \left\{ \begin{array}{ccc} F_f & F_i & L \\ J_i & J_f & I \end{array} \right\} \left\langle \alpha_fJ_f \,\|H_\gamma(pL)\|\, \alpha_iJ_i \right\rangle . \end{aligned} \tag{A.14}$$

A.2 Transition Matrix Element: Bessel beam

The derivation of the transition matrix element for the excitation of hyperfine levels by twisted Bessel beams follows the same pattern as the earlier for plane waves. Now, we have to insert the vector potential for Bessel beams $\mathcal{A}^{(\mathrm{tw})}$ (2.30) into the transition matrix element (6.2)

$$\mathcal{M}^{(\mathrm{pl})}_{fi} = \left\langle \alpha_fF_fM_f \left| \sum_q \boldsymbol{\alpha}_q \cdot \boldsymbol{\mathcal{A}}^{(\mathrm{tw})}(\boldsymbol{r}_q) \right| \alpha_iF_iM_i \right\rangle . \tag{A.15}$$

The first steps are the same as in the plane-wave case. Also here we have to rotate the states with Wigner-D matrices, multiply the two of them, and write the initial ($k = i$) and final ($k = f$) state $|\alpha_kF_kM_k\rangle$ as linear combinations of $|\alpha_kJ_kM_{J_k}\rangle$ and $|IM_I\rangle$. The difference comes from the vector potential, i.e. when we develop it into the multipoles. Together with the other steps we get then the following

$$\begin{aligned} \mathcal{M}^{(\mathrm{tw})}_{fi} \;&=\; \sum_{M_{J_f},M_{J_i}} \sum_{\nu,\mu,\mu'} \left\langle F_iM_i\ F_f-M_f \mid \nu\mu \right\rangle (-1)^{M_f+\mu'+J_f+I+\nu}\, \frac{[F_i,L,\nu]^{1/2}}{[J_f]} \\ &\quad\times \left\langle \nu\mu'\ \ J_i-M_{J_i} \mid J_f-M_{J_f} \right\rangle D^\nu_{\mu\mu'}(\phi,\theta,0) \left\{ \begin{array}{ccc} F_f & F_i & \nu \\ J_i & J_f & I \end{array} \right\} \\ &\quad\times \sqrt{2\pi}\, (-1)^{m_l+\lambda} \sum_{L,M,p} i^{L+M}\, [L]^{1/2}\, (i\lambda)^p\, e^{i(m_l+\lambda-M)\varphi_b} J_{m_l+\lambda-M}(\varkappa b)\, d^L_{M\,\lambda}(\theta_k) \\ &\quad\times \left\langle J_iM_{J_i}\ LM \mid J_fM_{J_f} \right\rangle \left\langle \alpha_fJ_f \,\|H_\gamma(pL)\|\, \alpha_iJ_i \right\rangle . \end{aligned} \tag{A.16}$$

After the summation over M_{J_f} and M_{J_i} (A.10), we get the final form of the transition amplitude for transitions between hyperfine states driven by a twisted Bessel beam, which is given by

$$\begin{aligned}\mathcal{M}_{fi}^{(\mathrm{tw})}(pL) &= C_{\alpha_i J_i \alpha_f J_f}^{F_i F_f I}(Lp)\ (i\lambda)^p\ (-1)^{m_l+\lambda}\left\langle F_i M_i\, L\Delta M \mid F_f M_f\right\rangle \\ &\quad\times \sum_M i^M\, e^{i(m_l+\lambda-M)\varphi_b} J_{m_l+\lambda-M}(\varkappa b)\, d^L_{M\,\lambda}(\theta_k)\, D^L_{M\,\Delta M}(\phi,\theta,0) \qquad \text{(A.17)}\end{aligned}$$

Here the factor $C_{\alpha_i J_i \alpha_f J_f}^{F_i F_f I}(pL)$ is the same as before for the plane waves.

Bibliography

[1] L. Allen, Philosophical transactions. Series A, Mathematical, physical, and engineering sciences **375** (2017).

[2] L. Allen, M. W. Beijersbergen, R. J. C. Spreeuw, and J. P. Woerdman, Phys. Rev. A **45**, 8185 (1992).

[3] M. W. Beijersbergen, L. Allen, H. van der Veen, and J. P. Woerdman, Opt. Commun. **96**, 123 (1993).

[4] M. Padgett, *Les Allen (1935–2016)* (IOP (Institute of Physics): available: iop.org/about/obituaries/page_72183.html, 04.12.2019).

[5] J. H. Poynting, Proc. R. Soc. Lond. A **82**, 560 (1909).

[6] R. A. Beth, Physical Review **50**, 115 (1936).

[7] J. P. Torres and L. Torner, *Twisted Photons: Applications of Light with Orbital Angular Momentum* (Weinheim, Germany: Wiley-VCH, 2011).

[8] M. Padgett, J. Courtial, and L. Allen, Phys. Today **57**, 35 (2004).

[9] V. Garcés-Chávez, D. McGloin, M. J. Padgett, W. Dultz, H. Schmitzer, and K. Dholakia, Phys. Rev. Lett. **91**, 093602 (2003).

[10] A. T. O'Neil, I. MacVicar, L. Allen, and M. J. Padgett, Phys. Rev. Lett. **88**, 053601 (2002).

[11] N. B. Simpson, K. Dholakia, L. Allen, and M. J. Padgett, Opt. Lett. **22**, 52 (1997).

[12] S. M. Barnett and L. Allen, Opt. Commun. **110**, 670 (1994).

[13] Nienhuis and Allen, Phys. Rev. A **48**, 656 (1993).

[14] Kim, Allen, and Loudon, Phys. Rev. A **50**, 3614 (1994).

[15] S. Katz, N. Kaplan, and I. Grossinger, Laser Technik J. **15**, 29 (2018).

[16] M. W. Beijersbergen, R. Coerwinkel, M. Kristensen, and J. P. Woerdman, Opt. Commun. **112**, 321 (1994).

[17] A. M. Yao and M. J. Padgett, Adv. Opt. Photon. **3**, 161 (2011).

[18] J. E. Curtis, B. A. Koss, and D. G. Grier, Opt. Commun. **207**, 169 (2002).

[19] D. O. Pabon, S. A. Ledesma, G. F. Quinteiro, and M. G. Capeluto, Appl. Opt. **56**, 8048 (2017).

[20] J. Bahrdt, K. Holldack, P. Kuske, R. Müller, M. Scheer, and P. Schmid, Phys. Rev. Lett. **111**, 034801 (2013).

[21] J. Dou, T. Xi, C. Ma, J. Di, and J. Zhao, Opt. Express **27**, 7968 (2019).

[22] I. P. Kaminow, T. Li, and A. E. Willner, *Optical Fiber Telecommunications VIA: Components and Subsystems*, Optics and Photonics, 6th ed. (Oxford: Elsevier, 2013).

[23] S. S. R. Oemrawsingh, J. A. W. van Houwelingen, E. R. Eliel, J. P. Woerdman, E. J. K. Verstegen, J. G. Kloosterboer, and G. W. 't Hooft, Appl. optics **43**, 688 (2004).

[24] M. Erhard, R. Fickler, M. Krenn, and A. Zeilinger, Light, science & applications **7**, 17146 (2018).

[25] F. Tamburini, B. Thidé, G. Molina-Terriza, and G. Anzolin, Nature Phys **7**, 195 (2011).

[26] G. F. Quinteiro and J. Berakdar, Opt. Express **17**, 20465 (2009).

[27] K. T. Kapale and J. P. Dowling, Phys. Rev. Lett. **95**, 173601 (2005).

[28] Y.-Y. Chen, J.-X. Li, K. Z. Hatsagortsyan, and C. H. Keitel, Phys. Rev. Lett. **121**, 074801 (2018).

[29] O. V. Bogdanov, P. O. Kazinski, and G. Y. Lazarenko, Phys. Rev. D **99**, 116016 (2019).

[30] X. Zhang, B. Shen, Y. Shi, L. Zhang, L. Ji, X. Wang, Z. Xu, and T. Tajima, New J. Phys. **18**, 083046 (2016).

[31] G. F. Quinteiro, D. E. Reiter, and T. Kuhn, J. Phys.: Conf. Ser. **906**, 012014 (2017).

[32] G. F. Quinteiro, F. Schmidt-Kaler, and C. T. Schmiegelow, Phys. Rev. Lett. **119**, 253203 (2017).

[33] G. F. Quinteiro, A. O. Lucero, and P. I. Tamborenea, J. Phys.: Condens. Matter **22**, 505802 (2010).

[34] O. Matula, A. G. Hayrapetyan, V. G. Serbo, A. Surzhykov, and S. Fritzsche, J. Phys. B **46**, 205002 (2013).

[35] A. Surzhykov, D. Seipt, and S. Fritzsche, Physical Review A **94** (2016).

[36] A. A. Peshkov, A. V. Volotka, A. Surzhykov, and S. Fritzsche, Phys. Rev. A **97** (2018).

[37] M. Babiker, D. L. Andrews, and V. E. Lembessis, J. Opt. **21**, 013001 (2019).

[38] N. Huntemann, M. Okhapkin, B. Lipphardt, S. Weyers, C. Tamm, and E. Peik, Phys. Rev. Lett. **108**, 090801 (2012).

[39] N. Huntemann, C. Sanner, B. Lipphardt, C. Tamm, and E. Peik, Phys. Rev. Lett. **116**, 063001 (2016).

[40] M. S. Zubairy, *Optics in Our Time*, edited by M. D. Al-Amri, M. El-Gomati, and M. S. Zubairy, 3–24 (s.l.: Springer, 2016).

[41] E. Hecht, *Optics*, Pearson global edition, 5th ed. (Boston and Columbus and Indianapolis: Pearson, 2017).

[42] J. C. Maxwell, Philosophical Transactions of the Royal Society of London **155**, 459 (1865).

[43] A. Einstein, Annalen der Physik **322**, 132 (1905).

[44] R. Loudon, *The Quantum Theory of Light*, Oxford science publications, 3rd ed. (Oxford: Oxford Univ. Press, 2010).

[45] J. D. Jackson, *Classical Electrodynamics*, third edition ed. (New York, NY: Wiley, 1999).

[46] T. Kundu, *Ultrasonic and Electromagnetic NDE for Structure and Material Characterization: Engineering and Biomedical Applications* (Boca Raton, Fla.: CRC Press, 2012).

[47] W. R. Johnson, *Atomic Structure Theory: Lectures on Atomic Physics* (Berlin, Heidelberg: Springer-Verlag Berlin Heidelberg, 2007).

[48] M. E. Rose, *Elementary Theory of Angular Momentum*, Structure of matter series, 2nd ed. (New York: Wiley, 1961).

[49] A. Das, *Lectures on Electromagnetism* (Singapore: World Scientific Publishing Company, 2013).

[50] D. L. Andrews and M. Babiker, editors, *The Angular Momentum of Light* (Cambridge: Cambridge University Press, 2013).

[51] Y. B. Band and Y. Avishai, *Quantum Mechanics with Applications to Nanotechnology and Information Science* (Elsevier Science, 2013).

[52] P. A. Tipler and R. A. Llewellyn, *Modern Physics*, 6th ed. (New York: W.H. Freeman, 2012).

[53] G. Nienhuis, Phil. Trans. R. Soc. A **375** (2017).

[54] R. R. Freeman, J. A. King, and G. P. Lafyatis, *Electromagnetic Radiation* (OUP Oxford, 2019).

[55] B. H. Bransden and C. J. Joachain, *Physics of Atoms and Molecules*, 2nd ed. (Harlow: Prentice Hall, 2006).

[56] J. Eichler, A. Ichihara, and T. Shirai, Phys. Rev. A **58**, 2128 (1998).

[57] H. M. Scholz-Marggraf, S. Fritzsche, V. G. Serbo, A. Afanasev, and A. Surzhykov, Phys. Rev. A **90** (2014).

[58] M. Abramowitz, I. A. Stegun, *Handbook of Mathematical Functions* (Washington, DC: National Bureau of Standards, 1964).

[59] I. N. Bronstein, K. A. Semendjajew, G. Musiol, and H. Mühlig, *Taschenbuch der Mathematik*, DeskTop, 5th ed. (Frankfurt am Main: Deutsch, 2001).

[60] A. Afanasev, C. E. Carlson, and A. Mukherjee, J. Opt. Soc. Am. B **31** (2014).

[61] G. Milione, H. I. Sztul, D. A. Nolan, and R. R. Alfano, Phys. Rev. Lett. **107**, 053601 (2011).

[62] V. Shvedov and W. Krolikowski, New J. Phys. **20**, 103034 (2018).

[63] M. McLaren, T. Konrad, and A. Forbes, *Laser Beam Shaping XVI*, edited by A. Forbes and T. E. Lizotte, SPIE Proceedings, 958106 (SPIE, 2015).

[64] E. Collett, *Polarized Light in Fiber Optics*, vol. 147 of */SPIE PM* (Lincroft, NJ: The PolaWave Group, 2003).

[65] M. Born and E. Wolf, *Principles of Optics: Electromagnetic Theory of Propagation, Interference and Diffraction of Light*, 7th ed. (Cambridge: Cambridge Univ. Press, 2003).

[66] G. G. Stokes, Trans. Cambridge Philos. Soc. 399 (1852).

[67] E. Collett, *Field Guide to Polarization*, vol. 5 of *SPIE field guides*, 3rd ed. (Bellingham, Wash.: SPIE Press, 2012).

[68] E. Collett, American Journal of Physics **36**, 713 (1968).

[69] H. Poincaré, *Théorie Mathématique de la Lumière*, Cours de la Faculté des sciences de Paris. Cours de physique mathématique (Paris: Gauthier Villars, 1892).

[70] S. A.-L. Schulz, A. A. Peshkov, R. A. Müller, R. Lange, N. Huntemann, C. Tamm, E. Peik, and A. Surzhykov, Phys. Rev. A ***(to be published)*** (2020).

[71] I. P. Ivanov, Phys. Rev. D **85** (2012).

[72] T. A. Fadeyeva, V. G. Shvedov, Y. V. Izdebskaya, A. V. Volyar, E. Brasselet, D. N. Neshev, A. S. Desyatnikov, W. Krolikowski, and Y. S. Kivshar, Opt. Express **18**, 10848 (2010).

[73] G. F. Quinteiro, D. E. Reiter, and T. Kuhn, Phys. Rev. A **95**, 012106 (2017).

[74] Z. Bomzon, G. Biener, V. Kleiner, and E. Hasman, Optics letters **27**, 285 (2002).

[75] R. Torres, T. Kaempfe, M. Delaigue, O. Parriaux, C. Honninger, J. Lopez, R. Kling, and E. Mottay, J. Laser Micro/Nanoeng. **8** (2013).

[76] J. Kalwe, M. Neugebauer, C. Ominde, G. Leuchs, G. Rurimo, and P. Banzer, Eur. J. Phys. **36**, 025011 (2015).

[77] J. A. Davis, N. Hashimoto, M. Kurihara, E. Hurtado, M. Pierce, M. M. Sánchez-López, K. Badham, and I. Moreno, Applied optics **54**, 9583 (2015).

[78] C. Maurer, A. Jesacher, S. Fürhapter, S. Bernet, and M. Ritsch-Marte, New Journal of Physics **9**, 78 (2007).

[79] G. Milione, *Vector Beams for Fundamental Physics and Applications*, Ph.d. thesis, City University of New York (2016).

[80] J. von Neumann, Nachrichten von der Gesellschaft der Wissenschaften zu Göttingen, Mathematisch-Physikalische Klasse **1927**, 245 (1927).

[81] J. von Neumann, *Mathematische Grundlagen der Quantenmechanik* (Berlin: Julius Springer Berlin, 1932).

[82] K. Blum, *Density Matrix Theory and Applications*, 3rd ed. (New York: Springer, 2012).

[83] U. Fano, Rev. Mod. Phys. **29**, 74 (1957).

[84] D. T. Haar, Reports on Progress in Physics **24**, 304 (1961).

[85] V. V. Balashov, A. N. Grum-Grzhimailo, and N. M. Kabachnik, *Polarization and Correlation Phenomena in Atomic Collisions* (New York: Kluwer, 2000).

[86] A. Surzhykov, D. Seipt, V. G. Serbo, and S. Fritzsche, Phys. Rev. A **91** (2015).

[87] T. Radtke, S. Fritzsche, and A. Surzhykov, Physical Review A **74**, 1484 (2006).

[88] J. Eichler, *Lectures on Ion-Atom Collisions* (Amsterdam: Elsevier, 2005).

[89] I. Grant, *Relativistic Quantum Theory of Atoms and Molecules: Theory and Computation*, vol. 40 of *Springer Series on Atomic, Optical, and Plasma Physics* (New York, NY and Berlin and Heidelberg: Springer, 2007).

[90] A. Afanasev, C. E. Carlson, and A. Mukherjee, Physical Review A **88** (2013).

[91] Y. Duan, R. A. Müller, and A. Surzhykov, J. Phys. B: At. Mol. Opt. Phys. **52**, 184002 (2019).

[92] S. A.-L. Schulz, S. Fritzsche, R. A. Müller, and A. Surzhykov, Phys. Rev. A **100** (2019).

[93] A. Kramida, Y. Ralchenko, J. Reader, and NIST ASD Team, *NIST Atomic Spectra Database, version 5.6.1, available: https://physics.nist.gov/asd (18. Jul 2019)* (Gaithersburg, MD: National Institute of Standards and Technology, 2019).

[94] S. Fritzsche, Comp. Phys. Commun. **240**, 1 (2019).

[95] C. T. Schmiegelow, J. Schulz, H. Kaufmann, T. Ruster, U. G. Poschinger, and F. Schmidt-Kaler, Nat. commun. **7**, 12998 (2016).

[96] Z. B. Maksić, *Theoretical Treatment of Large Molecules and Their Interactions: Part 4 Theoretical Models of Chemical Bonding* (Berlin and Heidelberg: Springer, 1991).

[97] M. Mirhosseini, O. S. Magaña-Loaiza, M. N. O'Sullivan, B. Rodenburg, M. Malik, M. P. J. Lavery, M. J. Padgett, D. J. Gauthier, and R. W. Boyd, New J. Phys. **17**, 033033 (2015).

[98] N. Huntemann, *High-Accuracy Optical Clock Based on the Octupole Transition in 171Yb+*, Ph.d. thesis, Universität Hannover (2014).

[99] F. Riehle, *Frequency Standards: Basics and Applications* (Weinheim: Wiley-VCH, 2010).

[100] H. Hellwig, *Frequency Standards and Clocks: A Tutorial Introduction*, 2nd ed. (Boulder, Colerado: National Bureau of Standards, 1977).

[101] Bureau International des Poids et Mesures, *SI Brochure: The International System of Units (SI)*, 9th ed. (2019).

[102] A. D. Ludlow, M. M. Boyd, J. Ye, E. Peik, and P. O. Schmidt, Rev. Mod. Phys. **87**, 637 (2015).

[103] I. I. Sobelman, *Atomic Spectra and Radiative Transitions*, vol. 12 of *Springer Series on Atoms+Plasmas*, second edition ed. (Berlin and Heidelberg: Springer, 1992).

[104] P. Taylor, *Observervation of an Ultra-High Q Resonance in a Single Ion of 172Yb+*, Ph.d. thesis, Clarendon Laboratory, University of Oxford (1996).

[105] M. Roberts, P. Taylor, G. P. Barwood, P. Gill, H. A. Klein, and W. R. C. Rowley, Phys. Rev. Lett. **78**, 1876 (1997).

[106] J. R. P. Angel and P. G. H. Sandars, Proc. R. Soc. Lond. A **305**, 125 (1968).

[107] E. Biémont and P. Quinet, Phys. Rev. Lett. **81** (1998).

[108] F. Le Kien, P. Schneeweiss, and A. Rauschenbeutel, The European Physical Journal D **67**, 1023 (2013).

[109] C. F. A. Baynham, E. A. Curtis, R. M. Godun, J. M. Jones, P. B. R. Nisbet-Jones, P. E. G. Baird, K. Bongs, P. Gill, T. Fordell, T. Hieta, T. Lindvall, M. T. Spidell, and J. H. Lehman, arxiv:1801.10134 (2018).

[110] B. S. Davis, L. Kaplan, and J. H. McGuire, J. Opt. **15**, 035403 (2013).

[111] A. A. Peshkov, V. G. Serbo, S. Fritzsche, and A. Surzhykov, Phys. Scr. **91**, 064001 (2016).

Publications by the Author

S. A.-L. Schulz, S. Fritzsche, R. A. Müller, and A. Surzhykov
Modification of multipole transitions by twisted light
Physical Review A 100, 043416 (2019)

S. A.-L. Schulz, A. A. Peshkov, R. A. Müller, R. Lange, N. Huntemann, Chr. Tamm, E. Peik, and A. Surzhykov
Generalized excitation of atomic multipole transitons by twisted light modes
Physical Review A (2020)
(accepted)

Acknowledgements

Viele werden mich bestätigen können, wenn ich sage, der Weg zum Ende einer Doktorarbeit ist nicht einfach und nicht immer geradlinig. Es gibt Abzweigungen, Höhen und Tiefen. Und aus diesen Gründen ist es wichtig, Personen in dieser Zeit um sich zu haben, die einen unterstützen und begleiten.

An dieser Stelle möchte ich allen Personen meinen großen Dank aussprechen, die mich während meiner Promotionszeit und bei der Anfertigung meiner Doktorarbeit unterstützt haben.

Als Erstes möchte ich meinem Doktorvater Prof. Andrey Surzhykov für die ausgezeichnete Betreuung und die Unterstützung bei der Umsetzung meiner Arbeit danken. Außerdem möchte ich mich bei Prof. Peter Lemmens bedanken, dass er sich für die Begutachtung meiner Dissertation bereit erklärt hat.

Besonderer Dank gilt Anton Peshov, Robert Müller und Yuxiong Duan für die zahlreichen thematischen Gespräche, Anregungen und Diskussionen. Des Weiteren danke ich Nils Huntemann und Richard Lange für die Geduld bei der Beantwortung meiner Fragen zu den experimentellen Aspekten meiner Arbeit. Außerdem möchte ich meinen restlichen Arbeitskollegen für die schöne Zeit am Institut meinen Dank aussprechen.

Zum Schluss möchte ich meiner Familie danken. Meine Eltern, meine Schwester und mein Freund haben mich während der Arbeit an dieser Doktorarbeit mit ihrer Geduld und Fürsorge ermutigt und unterstützt.

Rechtsverbindliche Erklärung gemäß § 8 der Promotionsordnung der Fakultät für Elektrotechnik, Informationstechnik, Physik der TU Braunschweig

Zu meiner vorliegenden Dissertation mit dem Thema "Excitation of Atoms by Twisted Light" erkläre ich, Sabrina Anna-Lena Schulz, hiermit rechtsverbindlich, dass

- ich noch kein Promotionsgesuch gestellt habe,
- ich die Dissertation selbst verfasst habe (Selbständigkeitserklärung), keine Textabschnitte von Dritten oder eigener Prüfungsarbeiten ohne Kennzeichnung übernommen und alle von mir benutzten Hilfsmittel und Quellen in meiner Arbeit angegeben habe,
- ich die Dissertation noch nicht als Prüfungsarbeit für eine staatliche oder andere wissenschaftliche Prüfung eingereicht habe,
- Dritte weder unmittelbar noch mittelbar geldwerte Leistungen von mir für Vermittlungstätigkeiten oder für Arbeiten erhalten haben, die im Zusammenhang mit dem Inhalt der vorgelegten Dissertation stehen, d.h. die wissenschaftliche Arbeit ist weder in Teilen noch in Gänze von Dritten gegen Entgelt oder sonstige Gegenleistung erworben oder vermittelt worden,
- ich die gleiche oder eine in wesentlichen Teilen ähnliche Arbeit noch nicht bei einer anderen Hochschule als Dissertation eingereicht habe,
- ich keine andere Abhandlung bei einer anderen Hochschule als Dissertation eingereicht habe,
- ich die vorliegende Dissertation noch nicht veröffentlicht habe,
- ich die Grundsätze zur Sicherung guter wissenschaftlicher Praxis an der TU Braunschweig kenne und beachtet habe,
- ich die Regeln der geltenden Promotionsordnung kenne und eingehalten habe und mit einer Prüfung nach den Bestimmungen der Promotionsordnung einverstanden bin,
- ich damit einverstanden bin, dass die Dissertation auch zum Zwecke der Überprüfung der Einhaltung allgemein geltender wissenschaftlicher Standards genutzt werden kann, insbesondere auch unter Verwendung elektronischer Datenverarbeitungsprogramme.

Braunschweig, den

_____

Sabrina Anna-Lena Schulz